Fall 12-2022

Kinetic Simulations of Active Nematic Polymers in Channel Flow

Lacey Savoie Schenk
Old Dominion University, lacey.s.schenk@gmail.com

KINETIC SIMULATIONS OF ACTIVE NEMATIC POLYMERS IN CHANNEL FLOW

by

Lacey Savoie Schenk
B.S. May 2008, United States Naval Academy
M.S. May 2017, Old Dominion University
M.S. May 2019, Old Dominion University

A Dissertation Submitted to the Faculty of
Old Dominion University in Partial Fulfillment of the
Requirements for the Degree of

DOCTOR OF PHILOSOPHY

COMPUTATIONAL AND APPLIED MATHEMATICS

OLD DOMINION UNIVERSITY
December 2022

Approved by

Ruhai Zhou (Director)

Xiang Xu (Member)

Sookyung Joo (Member)

Yaohang Li (Member)

ABSTRACT

KINETIC SIMULATIONS OF ACTIVE NEMATIC POLYMERS IN CHANNEL FLOW

Lacey Savoie Schenk
Old Dominion University, 2022
Director · Dr. Ruhai Zhou

Suspensions of active nematic liquid crystalline polymers exhibit complex phenomena such as spontaneous flows, pattern formations, and defects. They have many applications in industry, commercial settings, and our daily lives. We employ the Kinetic Model for our research, an extensive model that couples the Smoluchowski Equation and the incompressible Navier-Stokes Equations to solve for the active nanorod number density function–a function dependent on the polymer's physical orientation and space at a given time. Using this function, we can derive the polymer's polarity and nematic orientations as well as other rheological properties. In this research, we conduct numerical simulations of active, polarized polymers in a microfluidic channel to investigate the competitive effects among different material constants, namely the nematic concentration and active strength. Further, we also study the effects of Poiseuille flow by imposing a pressure gradient along the length of the channel. Both Dirichlet and Neumann boundary conditions are employed on the polymer's polarity vector. No-slip boundary conditions are imposed along the channel walls. We explore the differences in the physical parallel anchoring and normal anchoring of the polymer along the boundaries. We begin with fluid velocity set to zero and the application of a small sinusoidal perturbation on specific spatial components within the model. Steady states, including isotropic and nematic states, as well as periodic states are observed. Spontaneous flows reveal interesting geometries in polarity vector orientation, such as flow reversals and banded structures with multiple regions and defects. Other rheological properties such as velocity, order parameter, and the normal stresses of the fluid are studied. Within Poiseuille flow simulations, we see backflow effects that preserve simulation geometry as well as pressure-induced periodic states.

To my husband, Michael.

ACKNOWLEDGEMENTS

I would like to thank Dr. Ruhai Zhou, my advisor, for his guidance during our work together. I appreciate your kindness and patience. You were always willing to answer my questions, even if I had asked them before. You kept my spirits high, reminded me to be patient and always said "Just have fun!" Thank you for always being willing to help, willing to meet, and willing to share your knowledge. Working with you has truly been a great joy of my life.

Thank you to my committee, Drs. Xiang Xu, Sookyung Joo, and Yaohang Li. I appreciate your time, inputs, and support. You all brought enthusiasm and kindness to the process this year, and for that, I could not be more grateful.

Thank you to Dr. Jin Ren for his assistance during my final semester. Sharing your experience of the process was invaluable, and your assistance in solving obscure LaTeX issues saved me more than a few hours. I wish you the best as you start your career.

Lastly, I would like to thank my husband, Michael. You always provided loving encouragement, starting from the decision to take math graduate courses, to being the lead cheerleader at my dissertation defense. Thank you for putting me first, despite the Navy telling you that "you should really do a tour in D.C." I could not have done this without your love and support.

TABLE OF CONTENTS

Page

LIST OF TABLES

LIST OF FIGURES

Figure Page

Figure Page

Figure Page

Figure Page

CHAPTER 1

INTRODUCTION

Liquid crystals are a state of matter between solids and liquids that exhibit physical properties of each [18, 20, 34, 36, 55]. There are four primary stages of liquid crystals: crystalline, smectic, nematic, and isotropic, with each state exhibiting varying degrees of positional and orientational order. Our research focuses on nematic liquid crystals. Nematic liquid crystals are macromolecular uniaxial rods with lengths modeled at 10-100 nanometers and suspended in a viscous fluid solvent [18], producing a solution that can successfully be modeled as an incompressible fluid [55]. Given their rod-like shape, when these particles are dissolved in a solution, they have a tendency to align themselves along similar orientations [32, 42] producing interesting geometric patterns.

Nematic liquid crystals are categorized as passive or active, and this research focuses on the active form. These active particles absorb energy from the surrounding environment [26] and transform it into mechanical motion [48]. They propel themselves in a collective way creating a dynamic state [22, 33, 50, 53] from the motion of the particles exhibiting stresses within the fluid [1, 49]. Particle motion can be classified as "pusher" motion or "puller" motion. These dynamic states produce remarkable hydrodynamic phenomena such as spontaneous flows, pattern formations, chaotic oscillations, and defects [43] which have been observed in the laboratory setting [31, 41, 54]. Because of industrial and scientific relevance, there is much interest in the area of active nematics during the past decade [47].

Self-propelling liquid crystals and living organisms, such as birds or fish, can both be classified as active matter. When active matter self-propels within a large group, the collective group dynamics exhibit a level of orientational order, which can be studied, classified, and predicted [25, 38]. Nematic liquid crystal research can be applied to other elongated microstructures, such as human epithelial cells and DNA structures [46]. The structure of biological tissues can be modeled with nematic fluids [27], and cytoskeletal fluids exhibit spontaneous flows under certain circumstances [23]. Profiles of these cells show orientational

order, axial movement, defect formation, and similar stress profiles to nematic liquid crystals [8,24,45]. The rod-like active liquid crystals we study are polarized with a distinct head and tail. Models that study these elongated liquid crystals are also used to predict behavior and study pusher and puller mobility in biological particles [61]. The collective motion of *E. Coli* organisms are widely studied using active particle-based research [7,10,40,51], as they exhibit pusher-like behavior on their surroundings [14]. Similarly, self-propelled bacteria of the *Chlamydomonas* genus exhibit puller-like behavior [14].

The unique properties of liquid crystals make them an invaluable building material in modern industry. Under certain circumstances, liquid crystals exhibit a high degree of orientational order, which at the molecular level is useful in polarizing light. This lends itself the construction of optical lenses [52]. Liquid crystals can be fashioned into polymer-based textiles that are highly durable, lightweight, and have the ability to withstand high temperatures [9, 21, 28]. The most commonly known use of liquid crystals' electro-optic qualities is in liquid crystal displays (LCDs). LCDs have been studied and manufactured for nearly six decades and play an important role in the construction of cellphones, televisions, and computer screens [30].

Mathematical models can study, explain, and predict the physical phenomenal of active nematic liquid crystals. Different types of mathematical models exist to model liquid crystals: continuous, mesoscopic, and microscopic [2,3]. These model differ in the general lengths of the objects the model studies. We employ the Kinetic Model in our research, which falls into the mesocopic/microscopic overlap. The Kinetic Model is a system of partial differential equations that solves for a probability density function, f, which gives the probability of finding a liquid crystal polymer at a certain spatial location, at a specific orientation, at a given time [18,37,50].

Our research focuses on the competing effects of two parameters within the Kinetic Model: nematic strength (N) and the stress activation parameter (ζ_a). Both of these parameters describe physical aspects of the liquid crystal in the solvent. Nematic strength describes the ability of the particle to self-align and is proportional to the volume fraction of polymers dissolved in the solvent. Raising N above 5 typically transitions an isotropic state to a nematic state [16]. A non-zero value of ζ_a indicates an active particle, and the param-

eter magnitude is a direct measure of the pusher/puller effect of the particle. By varying these two parameters within different mathematical settings, we produce simulation results that reveal spontaneous flows of the microfluidic solution and complex geometries of liquid crystal orientation. This thesis is organized in the following manner: Chapter 2 reviews the Kinetic Model and associated equations, parameters, and methodology. We explore in detail the numerical methods that we use to solve the Kinetic Model. Chapters 3 though 5 contain simulation results and rheological data of our research using the Kinetic Model. In Chapter 3, we first explore the effects of Dirichlet boundary conditions with both parallel and normal positional anchoring of the polymer. Next, in Chapter 4 we impose homogenous Neumann boundary conditions and explore their effects on the simulation. Finally in Chapter 5, using results from Chapters 3 and 4, we impose a pressure gradient within the simulation space of the channel, creating Poiseuille flow.

CHAPTER 2

THE KINETIC MODEL

2.1 KINETIC MODEL EQUATIONS

The Kinetic Model is a system of partial differential equations governing the active nanorod number density function, $f(\boldsymbol{m}, \boldsymbol{x}, t)$, a probability density function dependent on the polymer's physical variables of orientation, $\boldsymbol{m}$, and space, $\boldsymbol{x}$, at a given time, t [19, 37]. The functional represented by the notation $\langle \cdot \rangle$ computes the average over the unit sphere and is used to calculate the moments of the density function f:

$$\langle (\cdot) \rangle = \int_{\|m\|=1} (\cdot) f(\boldsymbol{m}, \boldsymbol{x}, t) d\boldsymbol{m}. \tag{1}$$

The vector $\boldsymbol{m}$ gives the particle's axis of orientation in a unit sphere. The angles θ and ϕ are the polar and azimuthal angle, respectively. We define $\boldsymbol{m}$ as:

$$\boldsymbol{m} = \begin{pmatrix} \sin\theta\cos\phi \\ \sin\theta\sin\phi \\ \cos\theta \end{pmatrix}. \tag{2}$$

The spatial variable is represented by the three-dimensional vector $\boldsymbol{x}$, and time is given by t. The function f becomes the basis function to compute mathematical moments that represent the liquid crystal polymers at a certain time and position [18]. Computing the first moment of the f, as seen below, produces the three-dimensional polarity vector, $\boldsymbol{p}$, which describes the average orientation of a monodomain of nematic liquid crystals. See Figure 1 for a graphical representation.

$$\boldsymbol{p} = \langle \boldsymbol{m} \rangle = \int_{\|m\|=1} \boldsymbol{m} f(\boldsymbol{m}, \boldsymbol{x}, t) d\boldsymbol{m}. \tag{3}$$

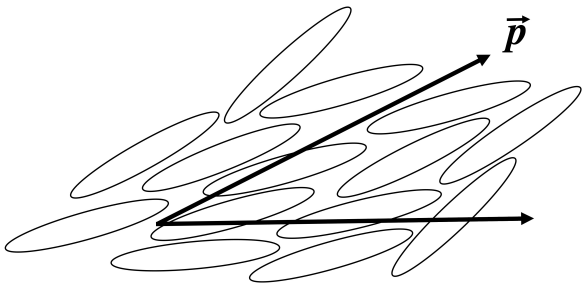

Figure 1: The computed polarity vector gives the average orientation for group of nanorods.

The second moment of f, or $\langle \boldsymbol{mm} \rangle$, produces the second moment tensor, denoted by $\boldsymbol{M}$. Using a summation of the zeroth, first, and second moments of f, we calculate the polymer's potential energy, U, by recalling the well-known potential energy equation [18]:

$$U = N_1\langle 1 \rangle - \alpha \langle \boldsymbol{m} \rangle \cdot \boldsymbol{m} - \frac{3N}{2} \langle \boldsymbol{mm} \rangle : \boldsymbol{mm}. \tag{4}$$

Three main coefficients describe the physical characteristics of the particle dissolved in the solvent: N, N_1, and α. Nematic strength, N, gives a measure of the particle's ability to self-align with nearby particles in the solution and is proportional to the volume fraction of polymers in the solvent [19]. The stronger the nematic strength, the greater the effect that particles will have on other particles around them due to proximity. Nematic strength is the first of two parameters investigated in this research. Spatial inhomogeneity is represented by the constant N_1 and gives a measure of the inconsistencies of the polymer concentration within the fluid. The parameter α is the strength of potential for polarity of the particle. A full listing of variables and coefficients can be found in Table 1. The second moment's double dot product with $\boldsymbol{mm}$ represents the physical restriction of excluded volume potential, or the concept that two objects, in this case liquid crystals, cannot occupy the same space at the same time [12].

2.1.1 THE SMOLUCHOWSKI EQUATION

The Kinetic Model is a coupling of three partial differential equations: the Smoluchowski Equation and the incompressible Navier-Stokes Equations. The Smoluchowski Equation

Nematic Strength	N
Polarity Strength	α
Homogeneity Strength	N_1
Potential Energy	U
Polar Angle	θ
Azimuthal Angle	ϕ
Particle Swimming Speed	U_0
Translational Diffusion	D_s
Rotational Diffusion	D_r
Geometry Parameter of Nanorod	a
Solvent Reynolds Number	Re,η
Reynolds Numbers - Viscous Stress	$Re_{2,3}$
Normalized Ansiotropic Stress Coefficient	G

Table 1: Description of Variables and Coefficients.

(5) describes the population balance of the active polar liquid crystals over time or the change in density of particles as they coagulate. We write the non-dimensional Smoluchowski Equation [18]:

$$\frac{\partial f}{\partial t} + \bigtriangledown \cdot \big((\boldsymbol{v} + U_0 \boldsymbol{m}) f\big) = \bigtriangledown \cdot D_s \cdot (\bigtriangledown f + f \bigtriangledown U) + \mathscr{R} \cdot D_r \cdot (\mathscr{R} f + f \mathscr{R} U) - \mathscr{R} \cdot (\boldsymbol{m} \times \dot{\boldsymbol{m}} f). \quad (5)$$

We identify the rotational gradient operator, $\mathscr{R}$, as $\boldsymbol{m} \times \dfrac{\partial}{\partial \boldsymbol{m}}$. We define the following in spherical coordinates on the unit sphere [5]:

$$\frac{\partial}{\partial \boldsymbol{m}} = \begin{bmatrix} \cos\theta\cos\phi\dfrac{\partial}{\partial\theta} - \dfrac{\sin\phi}{\sin\theta}\dfrac{\partial}{\partial\phi} \\ \cos\theta\sin\phi\dfrac{\partial}{\partial\theta} + \dfrac{\cos\phi}{\sin\theta}\dfrac{\partial}{\partial\phi} \\ -\sin\theta\dfrac{\partial}{\partial\phi} \end{bmatrix}, \quad (6)$$

$$\mathscr{R} = \begin{bmatrix} -\cos^2\theta\sin\phi\dfrac{\partial}{\partial\theta} + \left(-\sin^2\theta\sin\phi - \dfrac{\cos\theta\cos\phi}{\sin\theta}\right)\dfrac{\partial}{\partial\phi} \\ \left(\cos\phi - \dfrac{\cos\theta\sin\phi}{\sin\theta}\right)\dfrac{\partial}{\partial\phi} \\ \dfrac{\partial}{\partial\phi} \end{bmatrix}. \quad (7)$$

We now describe the physical phenomena represented by the different terms of the Smoluchowski Equation. The term $\bigtriangledown \cdot \big((\boldsymbol{v} + U_0\boldsymbol{m})f\big)$ describes the convection process of the particles in the solution, where $\boldsymbol{v}$ is the three-dimensional velocity of the fluid dependent on space and time.

Translational diffusion describes the spatial diffusion of the particle in space, given by the term, $\bigtriangledown \cdot D_s \cdot (\bigtriangledown f + \bigtriangledown U)$. The translational diffusion coefficient, D_s, is computed as:

$$D_s = D_{\parallel}\boldsymbol{mm} + D_{\perp}(\boldsymbol{I} - \boldsymbol{mm}). \tag{8}$$

The matrices $D_{\parallel}$ and $D_{\perp}$ represent the parallel and perpendicular values of the translational diffusion coefficient to $\boldsymbol{m}$. In our simulations, we take D_s as a constant value.

Rotational diffusion describes the movement of the particle as related to the spatial diffusion over the surface of a sphere. It is defined by the term of $\mathscr{R} \cdot D_r \cdot (\mathscr{R}f + f\mathscr{R}U)$. D_r is the rotational diffusion coefficient.

The final term, $\mathscr{R} \cdot (\boldsymbol{m} \times \dot{\boldsymbol{m}}f)$, describes the orbit of the particle on the unit sphere using the Jeffery Orbit equation [18]:

$$\dot{\boldsymbol{m}} = \boldsymbol{W} \cdot \boldsymbol{m} + a[\boldsymbol{D} \cdot \boldsymbol{m} - \boldsymbol{D} : \boldsymbol{mmm}]. \tag{9}$$

The geometry of the particle is given by the parameter a, where $a = \dfrac{r^2 - 1}{r^2 + 1}$, and r is the aspect ratio of the particle, or measure of elongation [18]. The matrices $\boldsymbol{D}$ and $\boldsymbol{W}$ are the symmetric and anti-symmetric forms of the velocity gradient tensor. The velocity gradient tensor measures the change of velocity from one spatial point to another at a single instance in time [32]. We consider an incompressible liquid crystal solution, therefore the trace of tensor is zero [32]. We decompose the velocity gradient tensor into $\boldsymbol{D}$ and $\boldsymbol{W}$:

$$\begin{aligned} \boldsymbol{D} &= \frac{1}{2}(\bigtriangledown \boldsymbol{v} + \bigtriangledown \boldsymbol{v}^T), \\ \boldsymbol{W} &= \frac{1}{2}(\bigtriangledown \boldsymbol{v} - \bigtriangledown \boldsymbol{v}^T). \end{aligned} \tag{10}$$

$\boldsymbol{D}$ represents the strain rate tensor, and $\boldsymbol{W}$, the vorticity tensor, both key components in the Jeffery Orbit Equation (9). [44]

We couple the Smoluchowski Equation with the incompressible Navier-Stokes Equations of conservation of mass and conservation of momentum to complete the Kinetic Model:

$$\begin{gathered}\frac{\partial \boldsymbol{v}}{\partial t} + \boldsymbol{v} \cdot \bigtriangledown \boldsymbol{v} = \bigtriangledown \cdot (-p\boldsymbol{I} + \boldsymbol{\tau}), \\ \bigtriangledown \cdot \boldsymbol{v} = 0.\end{gathered} \tag{11}$$

2.1.2 THE STRESS TENSOR, $\boldsymbol{\tau}$

The stress tensor is $\boldsymbol{\tau}$, and the pressure is given by p. The stress tensor is the sum of the different stresses within the fluid: viscous stress, active stress, and passive stress:

$$\tau = \tau_{viscous} + \tau_{active} + \tau_{passive}. \tag{12}$$

Viscous stress, represented by $\tau_{viscous}$, is the stress contribution from the viscosity of the solvent (η) as the fluid flows past the particle [32], and is computed by the Newtonian constitutive law:

$$\tau_{viscous} = 2\eta \boldsymbol{D}. \tag{13}$$

Active stress, τ_{active}, is the stress component derived from the mobility of the particle. The presence of the stress activation parameter, ζ_a, make the liquid crystal *active* versus *passive*. It is the second of two parameters investigated in this report. When the stress activation parameter is negative, the polymer exerts an extensile force and acts as a "pusher" to surrounding polymers. When the stress activation parameter is positive, the polymer is contractile, acting as "puller" [59], as seen in Figure 2. The greater the magnitude of $|\zeta_a|$, the stronger pusher/puller effect [13].

We compute active stress using the well-known formula:

$$\tau_{active} = G\zeta_a \left[\boldsymbol{M} - \frac{1}{3}\boldsymbol{I} \right]. \tag{14}$$

Passive stress, $\tau_{passive}$, is generated from the elasticity of the nanorod ensemble. It is

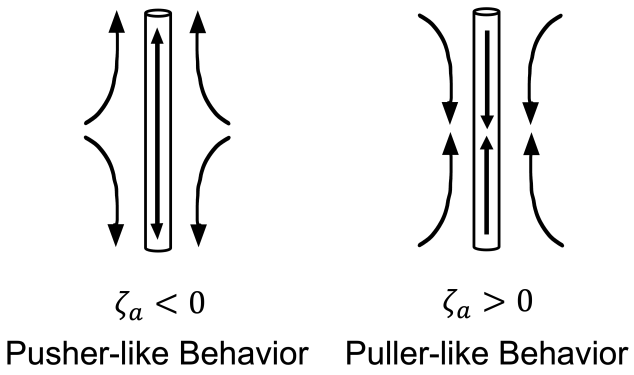

Figure 2: Pusher vs. Puller Polymer Activation Strength.

computed as following [58], note: $\boldsymbol{M}_n$ denotes the n-th moment of $\boldsymbol{m}$, or $\langle \boldsymbol{m}^n \rangle$:

$$\tau_{passive} = 2Re^{-1}\boldsymbol{D} + G\left[\boldsymbol{M} - \frac{1}{3}c\boldsymbol{I} - N\boldsymbol{M}^2 + N\boldsymbol{M} : \boldsymbol{M}_4\right] - \frac{1}{6}\alpha_0 G[2\boldsymbol{pp} - (\boldsymbol{M}_3 \cdot \boldsymbol{p} + \boldsymbol{p} \cdot \boldsymbol{M}_3)] + Re_2^{-1}[\boldsymbol{D} \cdot \boldsymbol{M} + \boldsymbol{M} \cdot \boldsymbol{D}] + Re_3^{-1}\boldsymbol{M}_4 : \boldsymbol{D}. \quad (15)$$

2.2 CHANNEL FLOW MODEL

Channel flow describes unidirectional streamline flows, such as the flow inside a pipe or down a river. We restrict our channel flow simulations of liquid crystal polymers to one dimension. Shown in Figure 3, we see the polarity vector spatial profile giving the orientation and magnitude of the liquid crystals in the channel. The spatial profile of fluid velocity is shown in a parabolic shape, as it often observed in a similar form at steady state. Fluid velocity at the upper and lower channel boundaries is set to the zero, giving the channel no-slip boundary conditions.

We mathematically reduce the Kinetic Model to model channel flow discretized along the y-axis. We define the spatial vector $\boldsymbol{x} = \begin{bmatrix} x \\ y \\ z \end{bmatrix}$ and velocity as $\boldsymbol{v} = \begin{bmatrix} v_1(x,y,z) \\ v_2(x,y,z) \\ v_3(x,y,z) \end{bmatrix}$. Our channel is defined in the y-direction, thus x and z remain constant for each time step ($\partial x = \partial z = 0$).

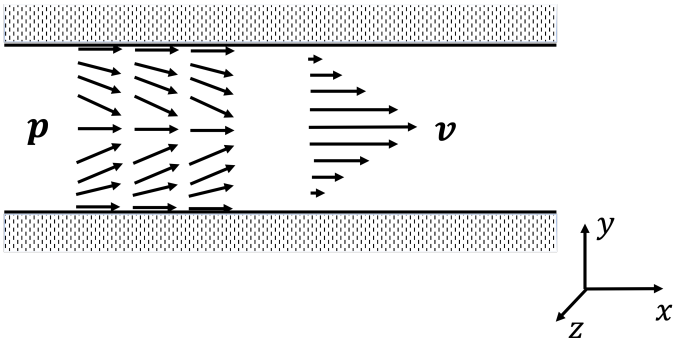

Figure 3: Channel flow geometry with polarity vector, $\boldsymbol{p}$ and velocity vector, $\boldsymbol{v}$. Vector orientation indicates positive direction.

Velocity is fully dependent on the spatial variable y, thus for this study, we neglect v_2 and v_3. We recall the Smoluchowski Equation (5):

$$\frac{\partial f}{\partial t} + \bigtriangledown \cdot \big((\boldsymbol{v} + U_0\boldsymbol{m})f\big) = \bigtriangledown \cdot D_s \cdot (\bigtriangledown f + f \bigtriangledown U) + \mathscr{R} \cdot D_r \cdot (\mathscr{R}f + f\mathscr{R}U) - \mathscr{R} \cdot (\boldsymbol{m} \times \dot{\boldsymbol{m}}f).$$

The convection term in channel flow expands as:

$$\bigtriangledown \cdot \big((\boldsymbol{v} + U_0\boldsymbol{m})f\big) = U_0 m_2 \frac{\partial f}{\partial y}. \tag{16}$$

The spatial diffusion term expands as:

$$\bigtriangledown \cdot D_s \cdot (\bigtriangledown f + f \bigtriangledown U) = D_s \frac{\partial}{\partial y}\left(\frac{\partial f}{\partial y} + f\frac{\partial U}{\partial y}\right). \tag{17}$$

The remaining terms on the right hand side do not contain spatial terms, so they do not need to be reduced. Equation 5 becomes:

$$\frac{\partial f}{\partial t} + U_0 m_2 \frac{\partial f}{\partial y} = D_s \frac{\partial}{\partial y}\left(\frac{\partial f}{\partial y} + f\frac{\partial U}{\partial y}\right) + \mathscr{R} \cdot D_r \cdot (\mathscr{R}f + f\mathscr{R}U) - \mathscr{R} \cdot (\boldsymbol{m} \times \dot{\boldsymbol{m}}f). \tag{18}$$

We reformat the incompressible Navier-Stokes Equations (11) into the velocity-pressure formulation [18]:

$$\frac{\partial \boldsymbol{v}}{\partial t} + (\boldsymbol{v} \cdot \bigtriangledown)\boldsymbol{v} = \bigtriangledown p + \eta\Delta\boldsymbol{v} + \bigtriangledown \cdot \tau, \tag{19}$$

$$\Delta p + \bigtriangledown \boldsymbol{v} : \bigtriangledown \boldsymbol{v}^T = \beta_0 \bigtriangledown \cdot \boldsymbol{v} + \bigtriangledown \cdot (\bigtriangledown \cdot \tau). \tag{20}$$

Within the Navier-Stokes conservation of mass equation (19), the first component becomes $\dfrac{\partial v_1(y)}{\partial t}$ as velocity is now in a one-dimensional space. We expand the second term as follows:

$$(\boldsymbol{v} \cdot \bigtriangledown)\boldsymbol{v} = \left(v_1 \frac{\partial}{\partial x} + v_2 \frac{\partial}{\partial y} + v_3 \frac{\partial}{\partial z} \right) \begin{bmatrix} v_1 \\ v_2 \\ v_3 \end{bmatrix} = \begin{bmatrix} v_1 \dfrac{\partial v_1}{\partial x} + v_2 \dfrac{\partial v_1}{\partial y} + v_3 \dfrac{\partial v_1}{\partial z} \\ v_1 \dfrac{\partial v_2}{\partial x} + v_2 \dfrac{\partial v_2}{\partial y} + v_3 \dfrac{\partial v_2}{\partial z} \\ v_1 \dfrac{\partial v_3}{\partial x} + v_2 \dfrac{\partial v_3}{\partial y} + v_3 \dfrac{\partial v_3}{\partial z} \end{bmatrix}. \tag{21}$$

Let $v_2 = 0$ as established above, and velocity is constant in the x and z-direction, making the first component of $(\boldsymbol{v} \cdot \bigtriangledown)\boldsymbol{v} = 0$.

To analyze the pressure term, we define p as a scalar quantity dependent the spatial variables, $p = p(x, y, z)$. Computing the gradient,

$$\bigtriangledown p = \begin{bmatrix} \frac{\partial p}{\partial x} \\ \frac{\partial p}{\partial y} \\ \frac{\partial p}{\partial z} \end{bmatrix} = \begin{bmatrix} 0 \\ \frac{\partial p}{\partial y} \\ 0 \end{bmatrix}. \tag{22}$$

To reduce to the one dimension, we take only the first component of the gradient vector, thus $\dfrac{\partial p}{\partial x} = 0$.

In calculations of the $\eta \Delta \boldsymbol{v}$ term in (19), with a constant velocity in the x and z-direction, we have the first component expanded as:

$$(\eta \Delta \boldsymbol{v})_1 = \eta \left(\frac{\partial^2 v_1}{\partial x^2} + \frac{\partial^2 v_1}{\partial y^2} + \frac{\partial^2 v_1}{\partial z^2} \right) = \eta \frac{\partial^2 v_1}{\partial y^2}. \tag{23}$$

Our stress tensor, $\boldsymbol{\tau}$, is defined as $\begin{bmatrix} \tau_{11} & \tau_{12} & \tau_{13} \\ \tau_{21} & \tau_{22} & \tau_{23} \\ \tau_{31} & \tau_{32} & \tau_{33} \end{bmatrix}$, where $\tau = \tau^T$. Computing the diver-

gence,

$$\bigtriangledown \cdot \boldsymbol{\tau} = \begin{bmatrix} \frac{\partial \tau_{11}}{\partial x} + \frac{\partial \tau_{12}}{\partial y} + \frac{\partial \tau_{13}}{\partial z} \\ \frac{\partial \tau_{21}}{\partial x} + \frac{\partial \tau_{22}}{\partial y} + \frac{\partial \tau_{23}}{\partial z} \\ \frac{\partial \tau_{31}}{\partial x} + \frac{\partial \tau_{32}}{\partial y} + \frac{\partial \tau_{33}}{\partial z} \end{bmatrix}. \tag{24}$$

Similar to our pressure term, we take only the first component to reduce to one dimension:

$$\left(\bigtriangledown \cdot \boldsymbol{\tau}\right)_1 = \frac{\partial \tau_{11}}{\partial x} + \frac{\partial \tau_{12}}{\partial y} + \frac{\partial \tau_{13}}{\partial z} = \frac{\partial \tau_{12}}{\partial y}. \tag{25}$$

Thus, the Equation (19) reduces to:

$$\frac{\partial v_1(y)}{\partial t} = \eta \frac{\partial^2 v_1}{\partial y^2} + \frac{\partial \tau_{12}}{\partial y}. \tag{26}$$

Next, we analyze Equation (20). Expanding the Laplacian for pressure:

$$\Delta p = \frac{\partial^2 p}{\partial x^2} + \frac{\partial^2 p}{\partial y^2} + \frac{\partial^2 p}{\partial z^2} = \frac{\partial^2 p}{\partial y^2}. \tag{27}$$

Our velocity component lies in the double dot product of the gradient of $\boldsymbol{v}$ with its transpose, denoting $[x_1, x_2, x_3] = [x, y, z]$,

$$\begin{aligned} \bigtriangledown \boldsymbol{v} : \bigtriangledown \boldsymbol{v}^T &= \sum_{i=1}^{3} \sum_{j=1}^{3} \left[\bigtriangledown \boldsymbol{v}\right]_{ij} \left[\bigtriangledown \boldsymbol{v}\right]_{ij}^T & (28) \\ &= \sum_{i=1}^{3} \sum_{j=1}^{3} \left[\bigtriangledown \boldsymbol{v}\right]_{ij} \left[\bigtriangledown \boldsymbol{v}\right]_{ji} & (29) \\ &= \sum_{i=1}^{3} \sum_{j=1}^{3} \frac{\partial v_j}{\partial x_i} \frac{\partial v_i}{\partial x_j} & (30) \\ &= \left(\frac{\partial v_2}{\partial y}\right)^2 = 0. & (31) \end{aligned}$$

To compute $\bigtriangledown \cdot (\bigtriangledown \cdot \boldsymbol{\tau})$, we expand:

$$\bigtriangledown \cdot (\bigtriangledown \cdot \boldsymbol{\tau}) = \begin{bmatrix} \frac{\partial}{\partial x} & \frac{\partial}{\partial y} & \frac{\partial}{\partial z} \end{bmatrix} \cdot \begin{bmatrix} \frac{\partial \tau_{11}}{\partial x} + \frac{\partial \tau_{12}}{\partial y} + \frac{\partial \tau_{13}}{\partial z} \\ \frac{\partial \tau_{21}}{\partial x} + \frac{\partial \tau_{22}}{\partial y} + \frac{\partial \tau_{23}}{\partial z} \\ \frac{\partial \tau_{31}}{\partial x} + \frac{\partial \tau_{32}}{\partial y} + \frac{\partial \tau_{33}}{\partial z} \end{bmatrix}$$

$$= \frac{\partial}{\partial x}\left[\frac{\partial \tau_{11}}{\partial x} + \frac{\partial \tau_{12}}{\partial y} + \frac{\partial \tau_{13}}{\partial z}\right] + \frac{\partial}{\partial y}\left[\frac{\partial \tau_{21}}{\partial x} + \frac{\partial \tau_{22}}{\partial y} + \frac{\partial \tau_{23}}{\partial z}\right] + \frac{\partial}{\partial z}\left[\frac{\partial \tau_{31}}{\partial x} + \frac{\partial \tau_{32}}{\partial y} + \frac{\partial \tau_{33}}{\partial z}\right]. \quad (32)$$

As $\partial x = \partial z = 0$, we have:

$$\bigtriangledown \cdot (\bigtriangledown \cdot \boldsymbol{\tau}) = \frac{\partial}{\partial y}\left[\frac{\partial \tau_{22}}{\partial y}\right] = \frac{\partial^2 \tau_{22}}{\partial y^2}. \quad (33)$$

Therefore, the Navier-Stokes conservation of momentum equation (20) reduces to:

$$\frac{\partial^2 p}{\partial y^2} = \frac{\partial^2 \tau_{22}}{\partial y^2}. \quad (34)$$

2.3 NUMERICAL METHODS

The active nanorod number density function, $f(\boldsymbol{x}, \boldsymbol{m}, t)$, depends on the position of the polymer in space and its orientation at a given time. Solving for f is a six-dimensional problem: the spatial variable $\boldsymbol{x}$ is three-dimensional, the orientation vector $\boldsymbol{m}$ is two-dimensional with the polar and azimuthal angles, and time, t, is one-dimensional. Each variable needs special numerical methods to ensure stability and proper representation [60]. We begin the mathematical procedures for solving the Kinetic Model using different discretizing techniques for different variables. We use spherical harmonic functions to expand the terms containing $\boldsymbol{m}$. We then perform a spatial discretization of the model using the Central Finite Difference Method, and using Method of Lines, we transform the system of partial differential equations into ordinary differential equations. Finally, using the first order Euler Method, we discretize the ordinary differential equations in time and using the Spectral Deferred Correction Method to increase the order [29, 60].

2.3.1 SPHERICAL HARMONICS

In our method, we begin to solve the Kinetic Model by the expansion of $\boldsymbol{m}$ using complex spherical harmonic functions [60]. Spherical harmonic functions are differentiable functions that satisfy Laplace's Equation on the surface of a sphere [15]. By expanding over the spherical variables of ϕ and θ, we reduce the equation to contain only the spatial and time variables. The spherical harmonic functions are defined as:

$$Y_l^m(\theta,\phi) = \sqrt{\frac{(2l+1)(l-m)!}{4\pi(l+m)!}} P_l^m(\cos\theta) e^{im\phi}, \tag{35}$$

where P_l^m represents the set of Legendre polynomials, and $l = 0, 1, ...$ and $m = -l, ..., 0, ..., l$. Spherical harmonic functions are chosen because of their orthogonality properties [6]:

$$\int_{\|m\|=1} Y_l^m \cdot (Y_{\tilde{l}}^{\tilde{m}})^* = \begin{cases} 1, & \text{for } l = \tilde{l}, m = \tilde{m} \\ 0, & \text{for } l \neq \tilde{l} \text{ or } m \neq \tilde{m}, \end{cases} \tag{36}$$

where $(Y_l^m)^* = (-1)^m Y_l^{-m}$.

Using spherical harmonics, we rewrite the nanorod density function, f, in Equation (37) as a summation of amplitude functions and spherical harmonic functions:

$$f(\boldsymbol{x}, \boldsymbol{m}, t) = \sum_{l=0}^{L} \sum_{m=-l}^{l} a_l^m(\boldsymbol{x}, t) Y_l^m(\boldsymbol{m}). \tag{37}$$

The complex amplitude functions are of the form $a_l^m(\boldsymbol{x}, t)$, and contain the remaining variables of space and time. The upper limit L gives the order of Galerkin approximation. By parity, we have a conjugate relationship of the complex coefficients: $\overline{a_l^m} = (-1)^m a_l^m$. From Equation (35), we compute $Y_0^0 = \dfrac{1}{\sqrt{4\pi}}$. Using spherical harmonic expansion we can calculate the real-valued concentration of the solvent as follows:

$$\begin{aligned} c = \langle 1 \rangle &= \int_{\|m\|=1} f(\boldsymbol{m}, \boldsymbol{x}, t) d\boldsymbol{m} \\ &= \int a_0^0 Y_0^0 d\boldsymbol{m} \\ &= \sqrt{4\pi} a_0^0 \int Y_0^0 (Y_0^0)^* d\boldsymbol{m} \\ &= \sqrt{4\pi} a_0^0. \end{aligned} \tag{38}$$

Similarly, we rewrite $\boldsymbol{m}$ using spherical harmonics. We use the expressions of Y_1^{-1}, Y_1^0, and Y_1^1, produced when $l = 1$:

$$Y_1^{-1}(\theta, \phi) = \frac{1}{2}\sqrt{\frac{3}{2\pi}} \sin\theta e^{-i\phi} = \frac{1}{2}\sqrt{\frac{3}{2\pi}} \sin\theta(\cos\phi - i\sin\phi) \tag{39}$$

$$Y_1^0(\theta, \phi) = \frac{1}{2}\sqrt{\frac{3}{\pi}} \cos\theta \tag{40}$$

$$Y_1^1(\theta, \phi) = -\frac{1}{2}\sqrt{\frac{3}{2\pi}} \sin\theta e^{i\phi} = -\frac{1}{2}\sqrt{\frac{3}{2\pi}} \sin\theta(\cos\phi + i\sin\phi). \tag{41}$$

We write an equivalent representation of $\boldsymbol{m}$ using the spherical harmonics defined above:

$$\boldsymbol{m} = \begin{bmatrix} \sin\theta\cos\phi \\ \sin\theta\sin\phi \\ \cos\theta \end{bmatrix} = \begin{bmatrix} \sqrt{\frac{2\pi}{3}}(Y_1^{-1} - Y_1^1) \\ \frac{-1}{i}\sqrt{\frac{2\pi}{3}}(Y_1^{-1} + Y_1^1) \\ 2\sqrt{\frac{\pi}{3}} Y_1^0 \end{bmatrix}. \tag{42}$$

To calculate the first moment, $\langle \boldsymbol{m} \rangle$, we rewrite (3) using the harmonic expansion of f in (37) and the expansion of $\boldsymbol{m}$ in (42).

$$\langle \boldsymbol{m} \rangle = \int_{\|m\|=1} \begin{bmatrix} \sqrt{\frac{2\pi}{3}}(Y_1^{-1} - Y_1^1) \\ \frac{-1}{i}\sqrt{\frac{2\pi}{3}}(Y_1^{-1} + Y_1^1) \\ 2\sqrt{\frac{\pi}{3}} Y_1^0 \end{bmatrix} \cdot \sum_{l=0}^{L} \sum_{m=-l}^{l} a_l^m(\boldsymbol{x}, t) Y_l^m(\boldsymbol{m}) d\boldsymbol{m}. \tag{43}$$

We compute the first component of $\langle \boldsymbol{m} \rangle$ by expansion and integration using the orthog-

onality property:

$$\begin{aligned}
\langle \boldsymbol{m} \rangle_1 &= \sqrt{\frac{2\pi}{3}} \int_{\|m\|=1} (Y_1^{-1} - Y_1^1)(a_1^{-1} Y_1^{-1} + a_1^1 Y_1^1) d\boldsymbol{m} \\
&= \sqrt{\frac{2\pi}{3}} \int a_1^{-1} Y_1^{-1} Y_1^{-1} + a_1^1 Y_1^1 Y_1^{-1} - a_1^{-1} Y_1^{-1} Y_1^1 - a_1^1 Y_1^1 Y_1^1 d\boldsymbol{m} \\
&= \sqrt{\frac{2\pi}{3}} \int (-1) a_1^{-1} Y_1^{-1} (Y_1^1)^* + (-1) a_1^1 Y_1^1 (Y_1^1)^* \\
&\quad -(-1) a_1^{-1} (Y_1^1)^* Y_1^1 - (-1) a_1^1 Y_1^1 (Y_1^{-1})^* d\boldsymbol{m} \\
&= \sqrt{\frac{2\pi}{3}} (-a_1^1 + a_1^{-1}) \\
&= \sqrt{\frac{2\pi}{3}} (-a_1^1 - \overline{a_1^1}) \\
&= -2\sqrt{\frac{2\pi}{3}} Re(a_1^1). \qquad (44)
\end{aligned}$$

The remaining vector components of $\boldsymbol{m}$ are shown below (computations are skipped):

$$\langle \boldsymbol{m} \rangle_2 = 2\sqrt{\frac{2\pi}{3}} Im(a_1^1), \qquad (45)$$

$$\langle \boldsymbol{m} \rangle_3 = 2\sqrt{\frac{\pi}{3}} a_1^0. \qquad (46)$$

Similarly, we construct our symmetric second moment tensor using the following combinations of amplitude functions [17] computed when $l = 2$:

$$\boldsymbol{M}_{11} = -\frac{2}{3}\sqrt{\frac{\pi}{5}} a_2^0 + \sqrt{\frac{8\pi}{15}} Re(a_2^2), \qquad (47)$$

$$\boldsymbol{M}_{22} = \frac{2}{3}\sqrt{\frac{\pi}{5}} a_2^0 - \sqrt{\frac{8\pi}{15}} Re(a_2^2), \qquad (48)$$

$$\boldsymbol{M}_{12} = \boldsymbol{M}_{21} = -\sqrt{\frac{8\pi}{15}} Im(a_2^2), \qquad (49)$$

$$\boldsymbol{M}_{13} = \boldsymbol{M}_{31} = -\sqrt{\frac{8\pi}{15}} Re(a_2^2), \qquad (50)$$

$$\boldsymbol{M}_{23} = \boldsymbol{M}_{32} = \sqrt{\frac{8\pi}{15}} Im(a_2^1). \qquad (51)$$

In this research, to solve the Kinetic Model we truncate to $L = 10$, producing a system

of 121 nonlinear partial differential equations. Expansions are performed for every term in the Smoluchowski Equation containing f, $\boldsymbol{m}$, or a moment of $\boldsymbol{m}$; details are not included in this report.

2.3.2 SPATIAL DISCRETIZATION

We begin our spatial discretization of the reduced Navier-Stokes Equation, recalling (26):

$$\frac{\partial v_1(y)}{\partial t} = \eta \frac{\partial^2 v_1}{\partial y^2} + \frac{\partial \tau_{12}}{\partial y}.$$

We discretize the first and second spatial derivatives on the right hand side using the Central Different Method:

$$\frac{\partial v_1(y)}{\partial t} = \eta \frac{(v_1)_{i+1} - 2(v_1)_i + (v_1)_{i-1}}{\Delta y^2} + \frac{(\tau_{12})_{i+1} - (\tau_{12})_{i-1}}{2\Delta y}. \tag{52}$$

Method of Lines is used to transform the PDE system into a set of ODEs. Spatial discretization for other equations in the Kinetic Model is similar.

2.3.3 TIME INTEGRATION

We now use the first order Euler Method to discretize in time, rewriting the left hand side of (52):

$$\frac{v_1^{n+1} - v_1^n}{\Delta t} = \eta \frac{(v_1)_{i+1}^n - 2(v_1)_i^n + (v_1)_{i-1}^n}{\Delta y^2} + \frac{(\tau_{12})_{i+1}^n - (\tau_{12})_{i-1}^n}{2\Delta y}. \tag{53}$$

Finally, we employ Spectral Deferred Correction method [17] to increase the order of the scheme in time [18]. The computed velocity is inserted in the system of harmonically-expanded, time-discretized Smoluchowski Equations:

$$\frac{f^{n+1} - f^n}{\Delta t} + U_0 m_2 \frac{\partial}{\partial y} f^n = \frac{\partial}{\partial y} \cdot D_s \Big(\frac{\partial f^{n+1}}{\partial y} + f^n \frac{\partial U^n}{\partial y} \Big) + \frac{1}{D_e} \mathscr{R} \cdot (\mathscr{R} f^n + f^n \mathscr{R} U^n) - \mathscr{R} \cdot (\boldsymbol{m} \times \dot{\boldsymbol{m}} f^n). \tag{54}$$

For our simulations, we use a spatial grid size of $\frac{1}{128}$ and a time step of 2×10^{-4}. We

Polarity Strength	$\alpha = 1$
Homogeneity Strength	$N_1 = 3$
Particle Swimming Speed	$U_0 = 1$
Translational Diffusion Coefficient	$D_s = 1$
Rotational Diffusion Coefficient	$D_r = 1$
Solvent Reynolds Number	$\eta = 5$
Reynolds Numbers - Viscous Stress	$Re_{2,3} = 5$
Normalized Ansiotropic Stress Coefficient	$G = 4$
Polar Extra Stress Activity Parameter	$\alpha_0 = 1$

Table 2: Kinetic Model Parameter Values.

validate our results using a spatial grid size of $\frac{1}{256}$ and a time step of 2×10^{-5}. Resulting relative error is computed between the steady state polarity vectors to be 0.009%.

2.4 SIMULATION DETAILS

Model Parameters

The parameters used within the model, with the exception of N and ζ_a, are defined in Table 2. The value listed is used for all simulations.

Initial Conditions

With the fluid velocity set to zero, $\boldsymbol{v} = 0$, at the initial time, we investigate spontaneous flows occurring from sinusoidal perturbations imposed on the polarity vector and nematic orientation tensor. The sine perturbations are spatially symmetric across the width of the channel and are applied to the polarity vector and the nematic director. For the polarity vector, the perturbation is applied to the non-dominating component of the polarity vector as show in Table 3 [57]. The dominating spatial component of the polarity vector in parallel anchoring is the x-direction (horizontal), setting the polymer to be aligned with the channel boundaries. For normal anchoring, the dominating spatial component is the y-direction (vertical), putting the polymer in a perpendicular position to the channel boundaries. Perturbations on the nematic director are imposed on the $(1, 2)$ component of the 3×3 second

Type of Anchoring	**Initial $\boldsymbol{p}$**
Parallel	$\boldsymbol{p} = \begin{bmatrix} 1 \\ 0.01\sin(2\pi y) \\ 0 \end{bmatrix}$
Normal	$\boldsymbol{p} = \begin{bmatrix} 0.01\sin(2\pi y) \\ 1 \\ 0 \end{bmatrix}$

Table 3: Initial Perturbations on Polarity Vector.

moment tensor, $\boldsymbol{M}$, are of the same magnitude as those imposed on the polarity vector.

Boundary Conditions

Boundary conditions on the Kinetic Model are applied to both the fluid velocity vector, $\boldsymbol{v}$, and the particle's polarity vector, $\boldsymbol{p}$. For all simulations we impose Dirichlet no-slip boundary conditions, or $\boldsymbol{v} = 0$ along the channel walls. For the polarity vector, both Dirichlet and Neumann boundary conditions are employed (in Chapter 3 and Chapter 4, respectively). When using Dirichlet boundary conditions, we anchor the position of the molecule along the channel walls in either a parallel or perpendicular position. For Neumann boundary conditions, we enforce $\dfrac{\partial f}{\partial y}$ across the upper and lower boundaries. This results in a constant orientation of the polarity vector across the boundaries. In all Neumann simulations, the polymers have parallel anchoring at initial time, but are unrestricted in orientation afterwards.

2.4.1 GRAPHICAL DETAILS OF RHEOLOGICAL SIMULATION DATA

Polarity Vector

The polarity vector graphs display a spatial cross section of the polarity vector orientation along the vertical axis. It is computed by the first moment of the number rod density function, f. The horizontal axis is time, displaying the last 300 time units of the simulation. The colored density plot is a measure of the changes in magnitude of the polarity vector.

Nematic Director

The nematic director graphs display a spatial cross section of the nematic director orientation along the vertical axis. The nematic director gives molecular directional order [35], and while it does have an orientation, it does not distinguish between head and tail. Using the symmetric tensor produced by second moment of the number rod density function, f, we compute the nematic director as the eigenvector corresponding to the largest eigenvalue. In the graph, the horizontal axis is time, displaying the last 300 time units of the simulation. The colored density plot is a measure of the degree of order, or order parameter, computed by taking the difference of the two largest eigenvalues of the second moment tensor.

Velocity

The velocity versus space plot shows the magnitude and sign of the velocity of the fluid, as seen during steady state, across the spatial profile of the channel. In periodic states, the simulation's velocity over time is also given. All velocity over space profiles show a velocity of zero at the boundaries, evident of the no-slip velocity boundary condition along channel walls.

Polarity Angle

The polarity angle versus space plot shows the measure of the polarity angle in radians, as seen during steady state, across the spatial profile of the channel.

Order Parameter

Order parameter measures the degree of molecular order. Order parameter measure is computed by the difference of the two leading eigenvalues computed from the second moment tensor. The order parameter versus space plot shows the magnitude of the order parameter, as seen during steady state, across the spatial profile of the channel. A liquid crystal in the perfect crystalline state has an order parameter of one. An order parameter at or near zero indicates that a defect exists, an area where the polymers do not show any preferred alignment [36]. In our simulations, only weak defects appear, which are indicated

by a low-valued order parameter.

Normal Stress Differences

Normal stress differences present themselves as streamlines of tension within the fluid [5]. The first normal stress difference is found in the direction of velocity flow, and is calculated by taking the difference of the stress tensor components of $\tau_{11} - \tau_{22}$. This value is generally negative, as our simulations confirm. The second normal stress is found along the z-axis, and is computed by $\tau_{22} - \tau_{33}$. The second normal stress difference is, on average, positive and is usually a fraction of the value of the first normal stress difference [32].

Apparent Stress

Apparent stress is calculated from the stress tensor component τ_{12} and scaling it by η. This value is calculated and plotted for each point in space as seen during steady state.

Note on Periodic Simulations

Steady state rheological data is presented via four snapshots from four equidistant points in one cycle.

CHAPTER 3

PARALLEL AND NORMAL ANCHORING SIMULATIONS

We begin our Kinetic Model simulations by imposing Dirichlet boundary conditions ensuring either parallel or normal anchoring of the polymer to the upper and lower channel walls. In this chapter, we explore both types of anchoring coupled with different values of nematic strength, N, and activation parameter ζ_a. Our goal is to investigate how they compete within spontaneous flow dynamics.

3.1 SIMULATIONS WITH PARALLEL ANCHORING AND PUSHER-LIKE BEHAVIOR

The following results are from simulations that have parallel anchoring on the boundaries for the polarity vector, as well as a negative value for the activation parameter, $\zeta_a < 0$. A negative activation parameter indicates pusher-like behavior of the polymer [18]. All simulations within this section reach steady state convergence.

3.1.1 INITIAL SINUSOIDAL PERTURBATION OF $\sin \pi$

Initial perturbations with differing wave numbers applied at initial time produce different steady states for otherwise identical simulations. This first section contains data when the perturbation of $\sin \pi x$ is applied, and the following section presents simulation results from a $\sin 2\pi x$ perturbation. Both sections divide results into Regions 1-4, with each region containing the same activation parameter and nematic strength in both sections. Remarkable similarities exist in structure geometry and within steady state data plots.

As shown in Figure 4, the different regions found within this section transition smoothly, in terms of geometry, from one section to the neighboring section. The different regions listed in Table 4 are chosen at an explicit point within the phase diagram. Minimum thresholds of activation parameter and nematic director are observed, notably when both values are very

Geometry Name	Nematic Strength	Active Strength
Forward Channel	$N = 4$	$\zeta_a = -10$
Forward Double Channel	$N = 2$	$\zeta_a = -50$
Simple Forward Flow	$N = 12$	$\zeta_a = -60$
Forward Centerline Flow	$N = 12$	$\zeta_a = -10$

Table 4: Description of observed states for Dirichlet boundary conditions with parallel anchoring and $\zeta_a < 0$.

low. Within this threshold, the simulations show an isotropic state, or a random orientation of polymers where all orientational order is lost [56].

Region 1.a: Forward Channel Flow

The Forward Channel flow simulation pairs a small value of nematic strength with a small activation parameter. In Figure 5, as the activation parameter increases with a constant nematic strength, a single banded channel in the center of the simulation is observed. The center of the channel has the highest fluid velocity, with an almost linear decrease to zero as the boundary approaches. All polarity vectors orient rightward in Figure 5(a), which also indicates the flow direction of fluid velocity. After a short transition time, the simulations quickly converge to steady state. The nematic director's geometry and direction, as seen in Figure 5(b), present a similar shape to the polarity diagram.

Observing the steady state rheological data, we see the polarity angle in Figure 6(a) over space diagram is skew-symmetric, with mostly positive angles on the lower half of the simulation, and mostly negative angles on the upper half. As the polymers approach centerline, we observe a sign change, which corresponds to the slight outward orientation seen in the polarity plot over time in Figure 5(a). The order parameter, show in Figure 6(b), increases in magnitude with an increasing distance from the channel walls, with a slight dip in the center of the channel. Fluid velocity in Figure 6(c) takes a parabolic shape, reaching a maximum value in the center of the channel. Apparent stress in Figure 6(d) is skew-symmetric, with negative values in the lower half of the channel and positive values in the upper half. First normal stress in Figure 6(e) is negative, indicating a stress difference along

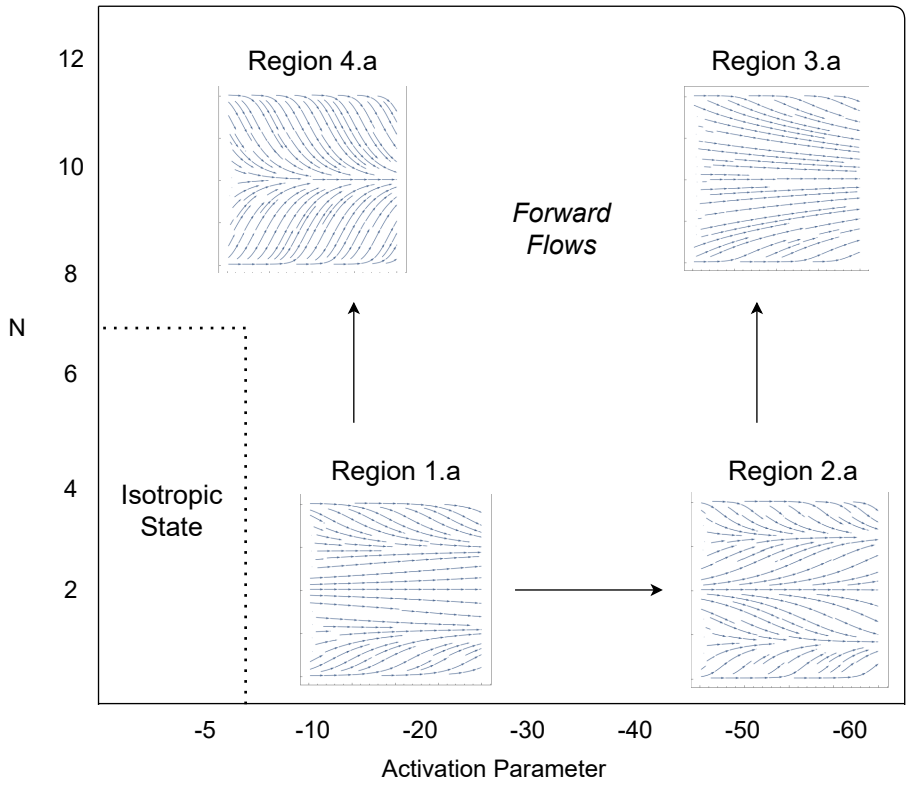

Figure 4: Phase diagram for Dirichlet boundary conditions with a positive activation parameter, showing simulation results for a $\sin \pi$ perturbation. Four distinct regions are identified. Transitioning geometries are denoted by arrows.

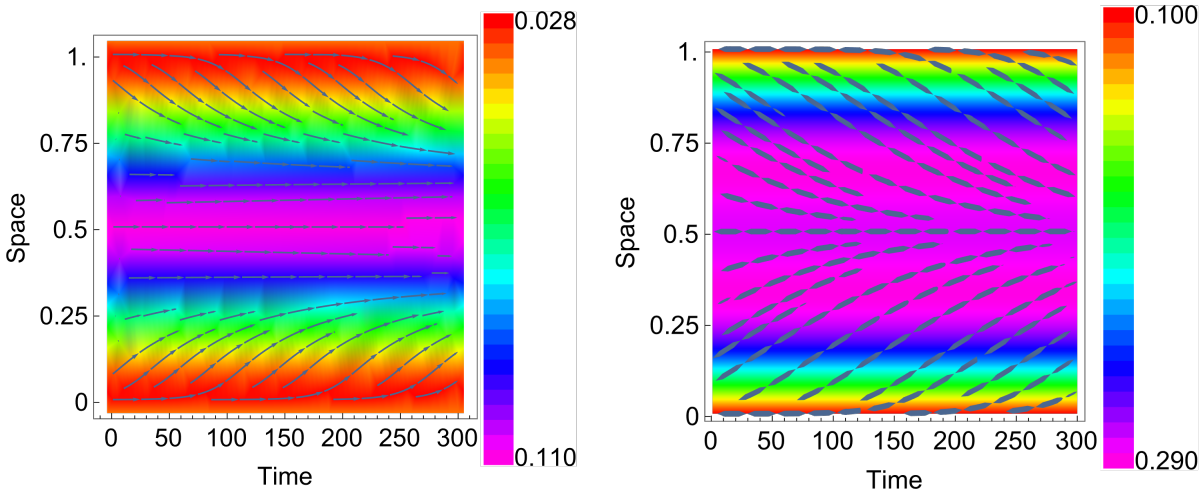

(a) Polarity vector at steady state. (b) Nematic director at steady state.

Figure 5: Region 1.a: Polarity and Nematic Plots for $N = 4$ and $\zeta_a = -10$.

the centerline of the channel in the direction opposite of observed velocity. Second normal stress in Figure 6(f) is positive and correlates in shape to the order parameter data.

Region 2.a: Forward Double Channel Flow

This region shows simulations that couple a small value for nematic strength with a large activation parameter. As the activation parameter is further increased from Region 1.a, the center channel becomes two distinct channels. This leads to the observation of four distinct bands of liquid crystals in the polarity vector diagram, shown in Figure 7(a). In nematic director diagram in Figure 7(b), we observe only two regions, which take nearly an identical shape to the previous nematic director observed in Figure 5(b).

Steady state rheological data for Region 2.a is presented in Figure 8. Analyzing the angle of the polarity vector at steady state in Figure 8(a), we see, again, skew-symmetry around the zeroes of the graph. In the first band, the polarity vector points upwards, while in the second band, the polarity vector points downwards. The third band has an upward-pointing polarity vector, and the fourth band has a downward-pointing polarity vector. The second and third

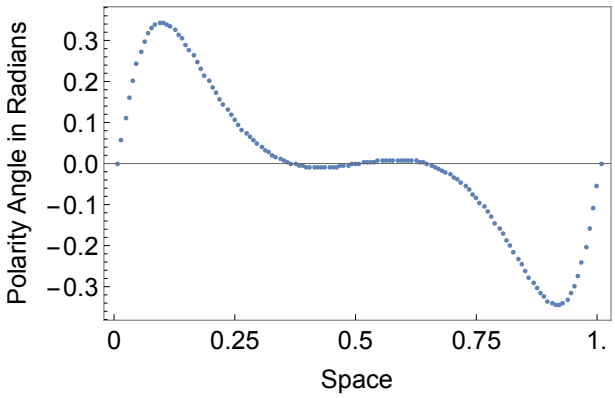

(a) Polarity angle over space.

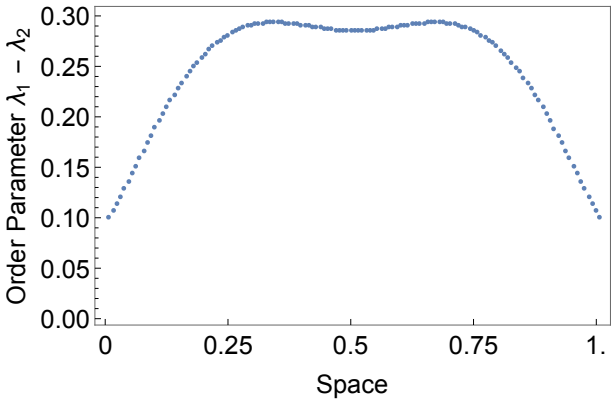

(b) Order parameter over space.

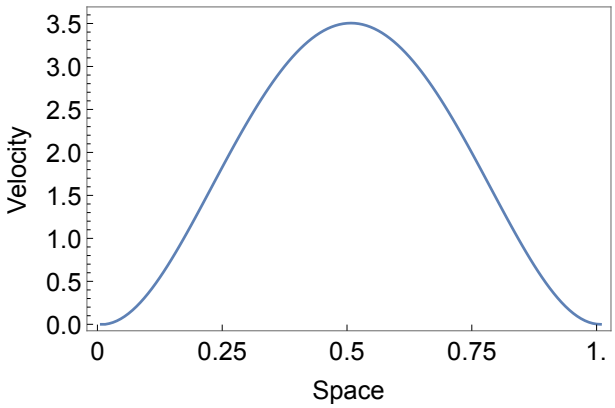

(c) Fluid velocity over space.

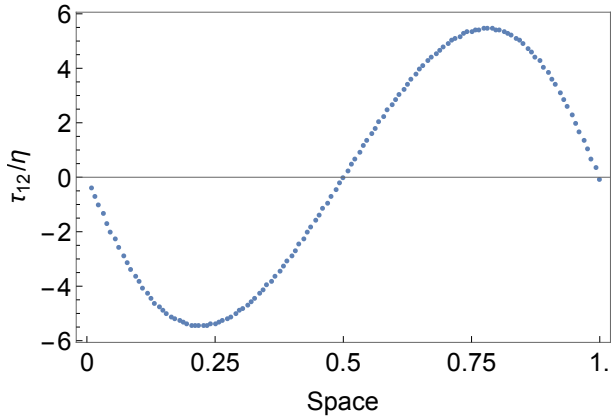

(d) Apparent stress over space.

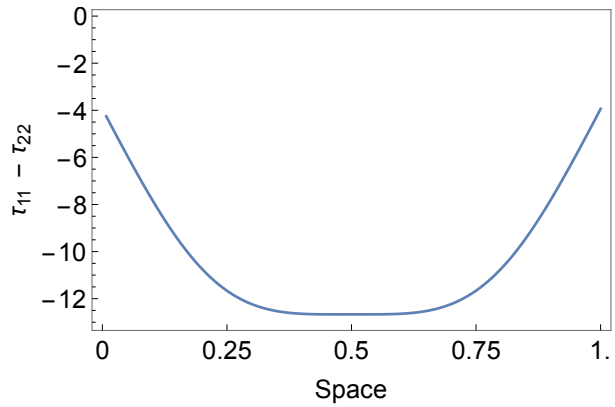

(e) First normal stress over space.

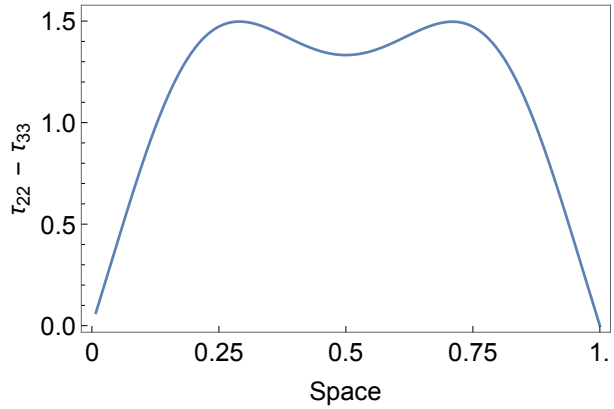

(f) Second normal stress over space.

Figure 6: Region 1.a: Rheological Properties for $N = 4$ and $\zeta_a = -10$.

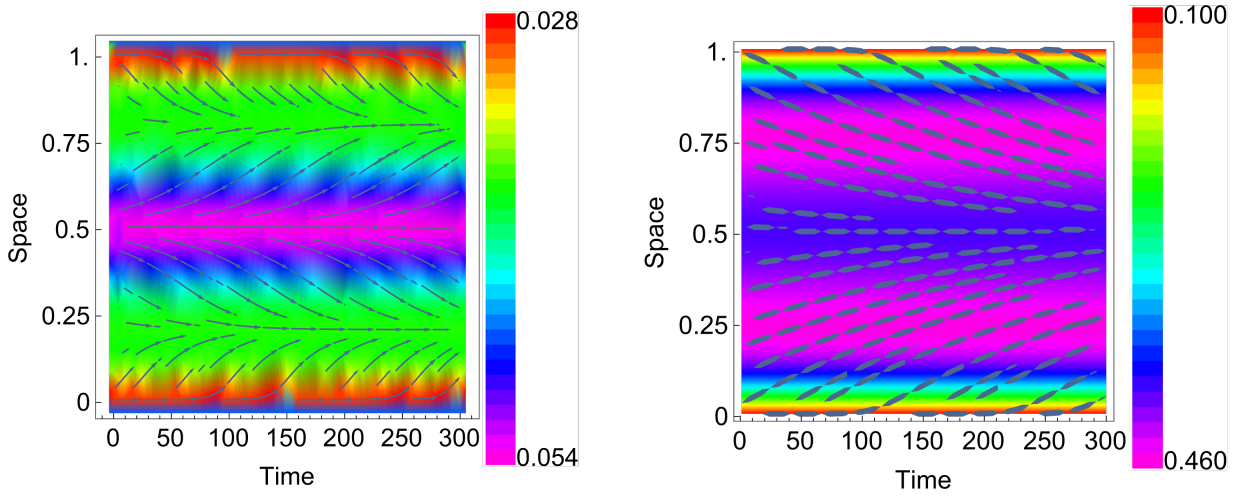

(a) Polarity vector at steady state.

(b) Nematic director at steady state.

Figure 7: Region 2.a: Polarity and Nematic Plots for $N = 2$ and $\zeta_a = -50$.

bands magnify the slightly outward orientation effect seen in Region 1.a's polarity angle diagram, a result of the increased activation parameter. The order parameter over space in Figure 8(b) shows the center of the channel having a higher degree of polymer order than the regions near the outer walls, yet dipping in the center of the channel. Similar to Region 1.a, Region 2.a's final steady state profile of velocity seen in Figure 8(c) reaches its maximum value in the center of the channel. However, the maximum value of velocity is nearly 3.5 times greater than the maximum velocity observed in Region 1.a. Figure 8(d)'s apparent stress profile presents skew-symmetry with an almost linear increase from the bottom to the top of the channel. First normal stress and second normal stress, Figure 8(e) and (f), respectively, take similar shapes to Region 1.a, but are observed at a magnitude of nearly 10 times greater than Region 1.a. This implies that an increased activation parameter also increases the non-Newtonian stress differences within the fluid.

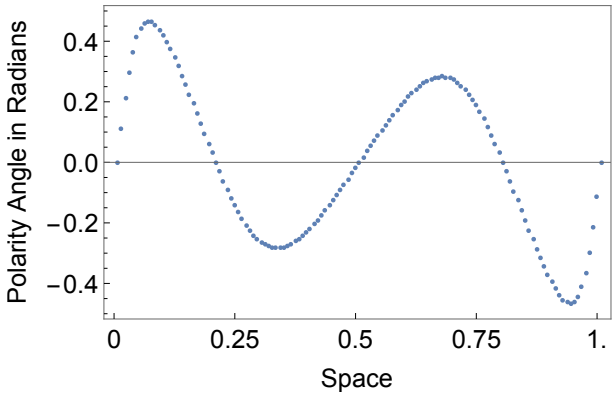

(a) Polarity angle over space.

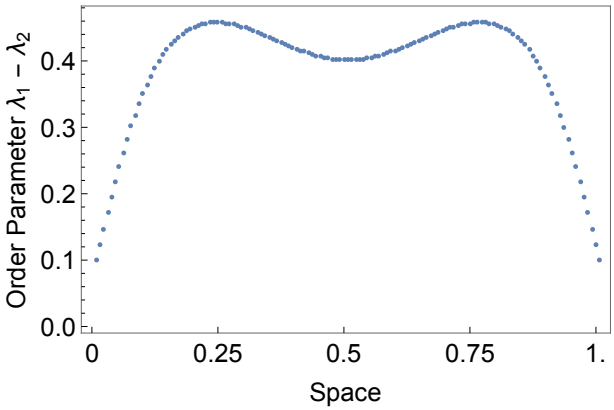

(b) Order parameter over space.

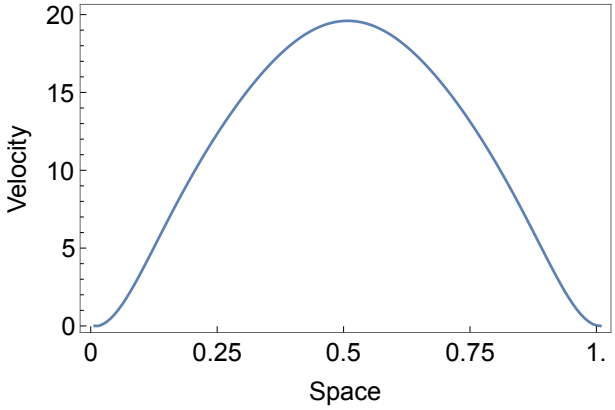

(c) Fluid velocity over space.

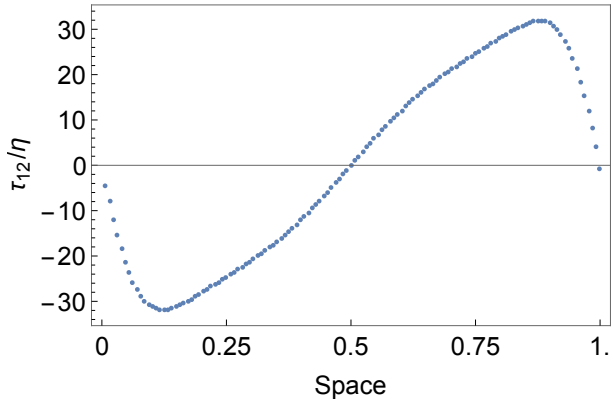

(d) Apparent stress over space.

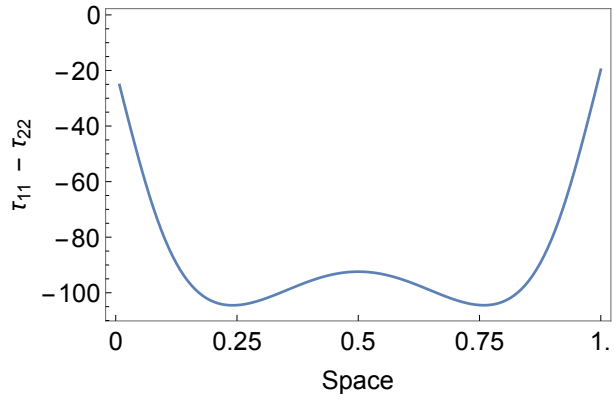

(e) First normal stress over space.

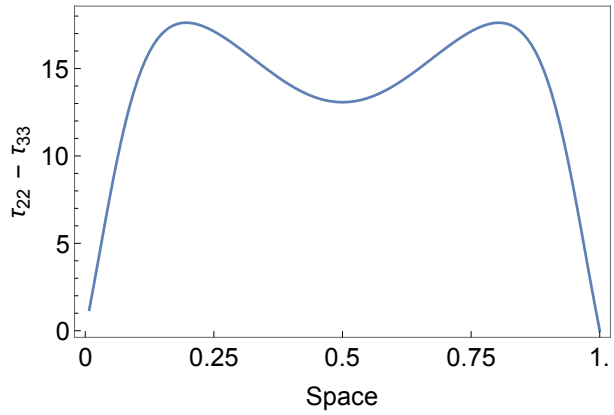

(f) Second normal stress over space.

Figure 8: Region 2.a: Rheological Properties for $N = 2$ and $\zeta_a = -50$.

Region 3.a: Simple Forward Flow

This region shows simulations of large nematic strength coupled with a large activation parameter. As nematic strength is increased from Region 2.a, the four bands give way to a single channel, as seen in Figure 9(a). An observable change in the nematic director orientation plot from Region 1.a and Region 2.a is the centerline vector begins to align horizontally, as seen in 9(b).

Observing a smooth geometry in Figure 9(a), we see the data correlate to a linear decrease of polarity angle over space in the steady state data plot of Figure 10(a). The order parameter profile in Figure 10(b) presents a high value of polymer orientational order in the center of the channel. We observe a decrease in the maximum value of velocity as compared to Region 2.a, but the profile maintains a parabolic shape in Figure 10(c). Apparent stress in Figure 10(d) is skew-symmetric, with negative values in the lower half of the channel and positive values in the upper half. The value of first normal stress difference in Figure 10(e) is again negative and is increased even further from Regions 1.a and 1.b, recording its maximum value in the center of the channel. The second normal stress difference is positive in Figure 10(f), taking a minimum value in the center of the channel and maximum values nearest the channel walls.

Region 4.a: Forward Centerline Flow

This region shows simulations with a large value of nematic strength and a small to intermediate activation parameter. As the nematic strength is decreased from Region 3.a, we see from our polarity diagram the polymers aligning towards a centerline, evenly dividing the channel in Figure 11(a). This effect was first seen in Region 3.a, and the effect is further increased as the activation parameter is decreased. Figure 11(b) presents a nematic director nearly parallel throughout in the channel to the channel boundaries.

Steady state rheological data in Figure 12 shows the effects of a decreased activation parameter. The polarity angle spatial plot in Figure 12(a) is skew-symmetric and correlates to the smooth geometries observed in Figure 11(a). The order parameter in Figure 12(b) is parabolic in form with a high value of orientational order of nearly 0.8 observed in channel center. Fluid velocity in Figure 12(c) indicates a very low velocity magnitude as compared

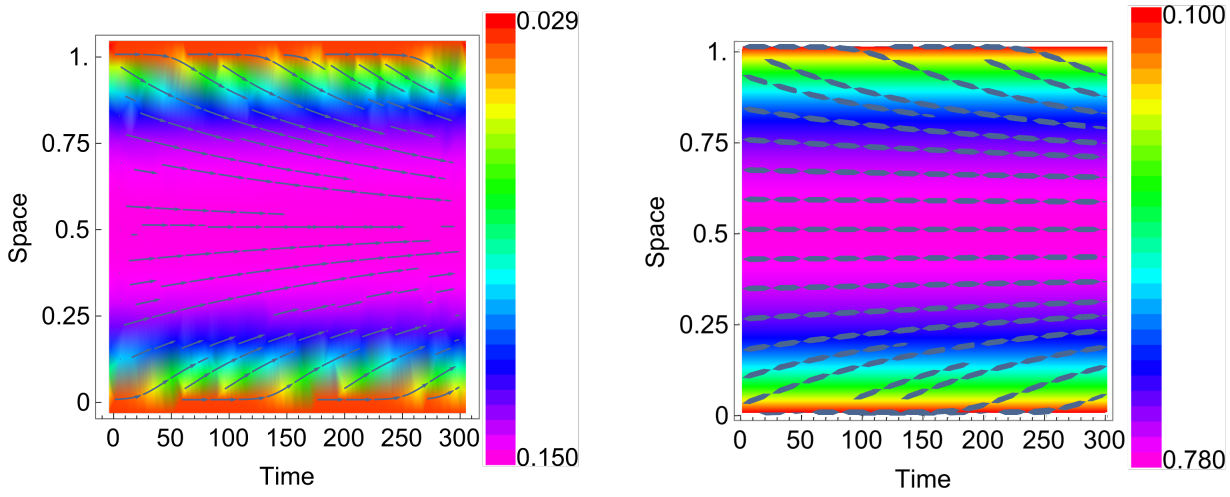

(a) Polarity vector at steady state.

(b) Nematic director at steady state.

Figure 9: Region 3.a: Polarity and Nematic Plots for $N = 12$ and $\zeta_a = -60$.

with previous regions, indicating that the decreased activation parameter greatly decreases fluid flow. Apparent stress in Figure 12(d) is skew-symmetric with an observed linear increase in the center regions of the channel. First normal stress difference in Figure 12(e) measures negative and decreases in magnitude when approaching channel center. Second normal stress difference in Figure 12(f) is positive nearest the channel boundaries, but experiences a drop to negative values and decreases towards channel center.

3.1.2 INITIAL PERTURBATION OF $\sin 2\pi$

The following section contains simulation results from an initial perturbation of $\sin 2\pi$. Dirichlet boundary conditions on the polarity vector exist as parallel anchoring, and the activation parameter remains negative. With a different wave number on the perturbation, we see similar geometries to the previous section with the same values of nematic strength and activation parameter–however, the polarity vector orientation and the direction of fluid flow is reversed. The exception is Region 4, with a high nematic strength and low activation parameter, we see forward flow geometry preserved. Observed states and their parameters

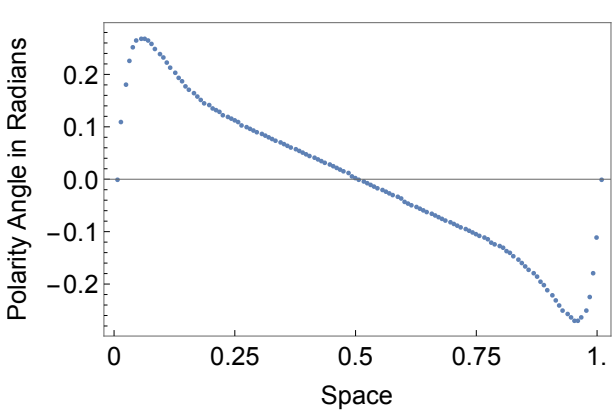

(a) Polarity angle over space.

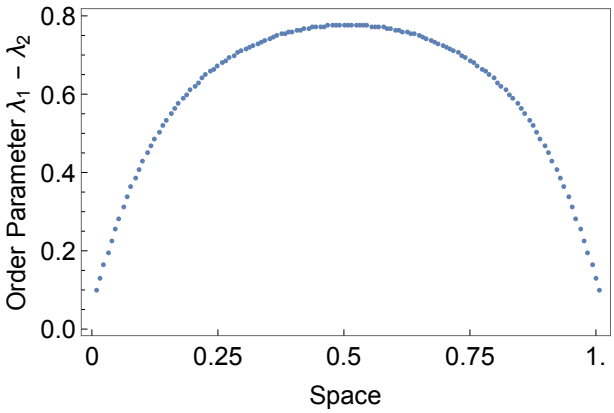

(b) Order parameter over space.

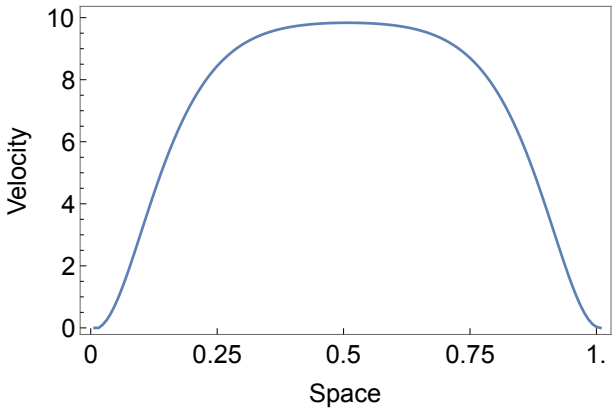

(c) Fluid velocity over space.

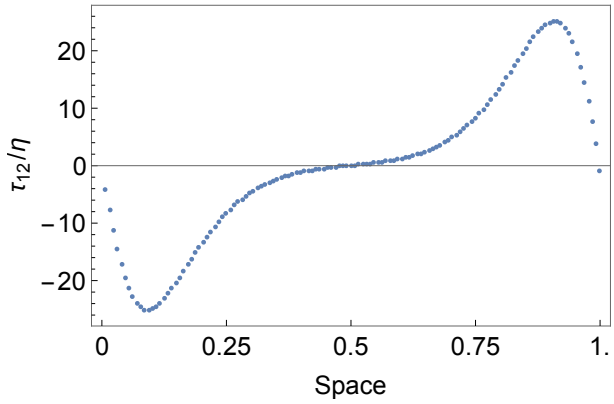

(d) Apparent stress over space.

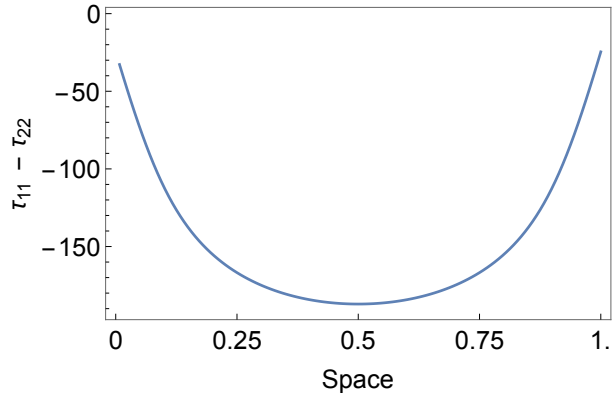

(e) First normal stress over space.

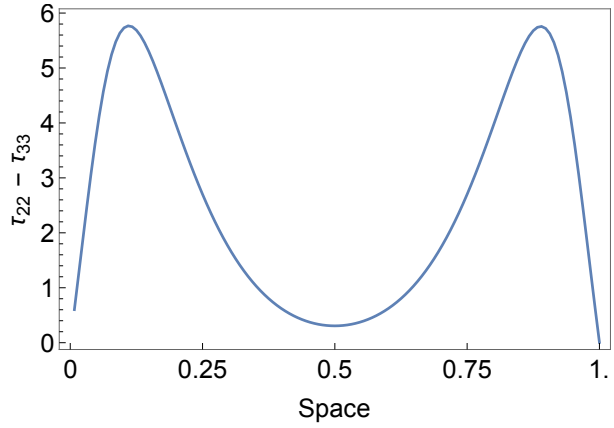

(f) Second normal stress over space.

Figure 10: Region 3.a: Rheological Properties for $N = 12$ and $\zeta_a = -60$.

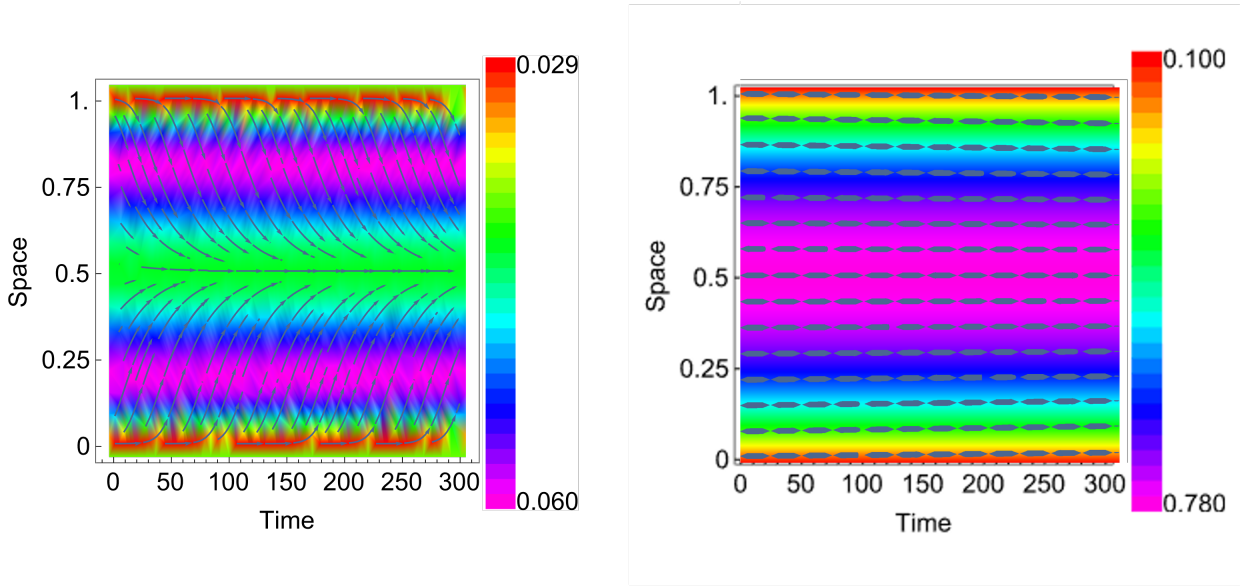

(a) Polarity vector at steady state.

(b) Nematic director at steady state.

Figure 11: Region 4.a: Polarity and Nematic Plots for $N = 12$ and $\zeta_a = -10$.

Geometry Name	Nematic Strength	Active Strength
Reverse Channel	$N = 4$	$\zeta_a = -10$
Reverse Double Channel	$N = 2$	$\zeta_a = -50$
Simple Reverse Flow	$N = 12$	$\zeta_a = -60$
Forward Centerline Flow	$N = 12$	$\zeta_a = -10$

Table 5: Description of observed states for Dirichlet boundary conditions with parallel anchoring and $\zeta_a < 0$.

are listed in Table 5 and the phase diagram can be found in Figure 13. Each region is described and contrasted to the $\sin \pi$ simulation of the same parameters.

Region 1.b: Reverse Channel Flow

The Reverse Channel flow simulation pairs a small value of nematic strength with a small activation parameter. In Figure 14(a), we see a strong resemblance to the $\sin \pi$ pertubation simulation in Figure 5(a), but the orientation is reversed. Our steady state polarity vector diagram in Figure 14(a) shows three distinct regions: the two outer regions each show

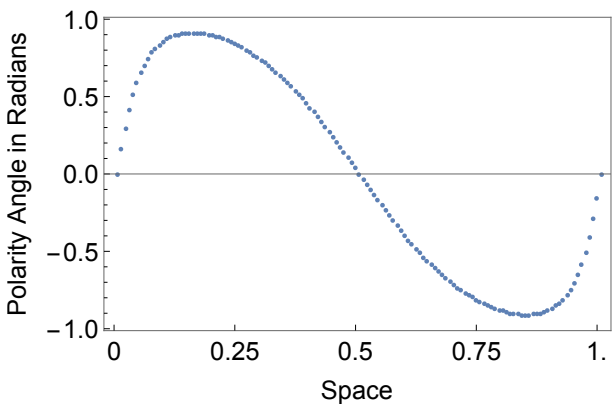

(a) Polarity angle over space.

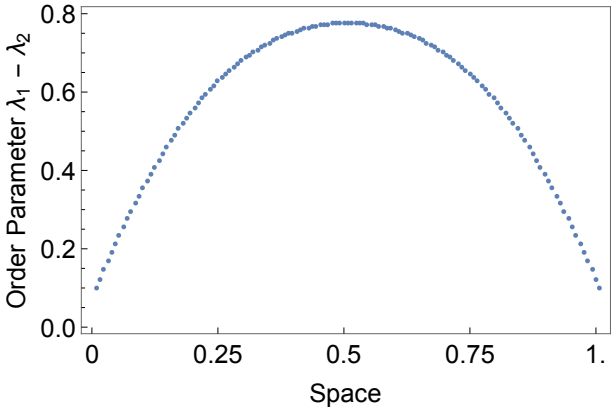

(b) Order parameter over space.

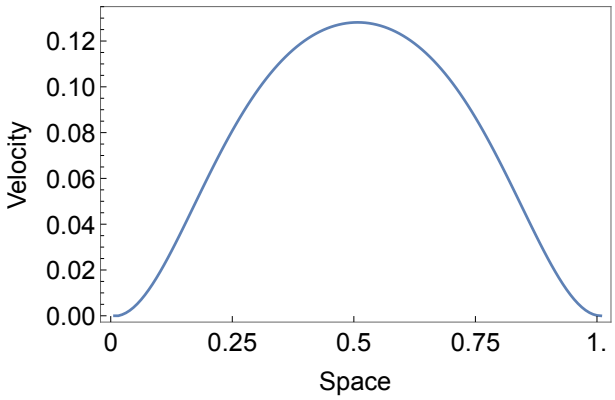

(c) Fluid velocity over space.

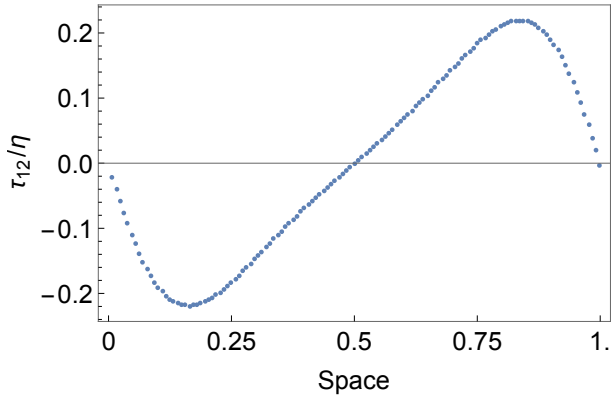

(d) Apparent stress over space.

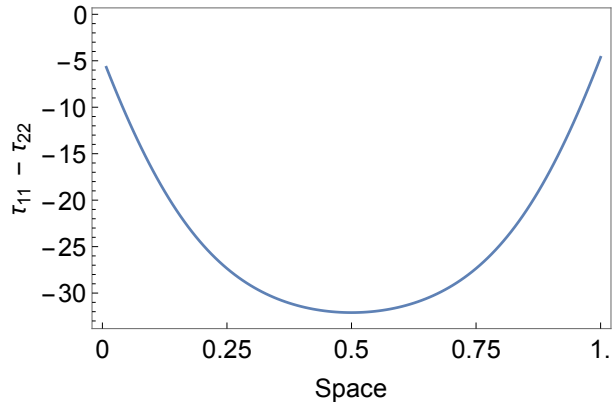

(e) First normal stress over space.

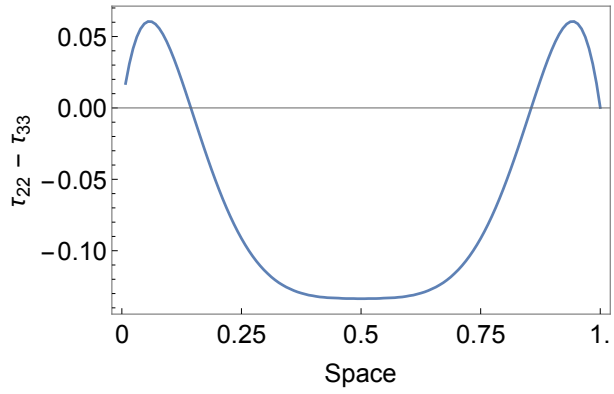

(f) Second normal stress over space.

Figure 12: Region 4.a: Rheological Properties for $N = 12$ and $\zeta_a = -10$.

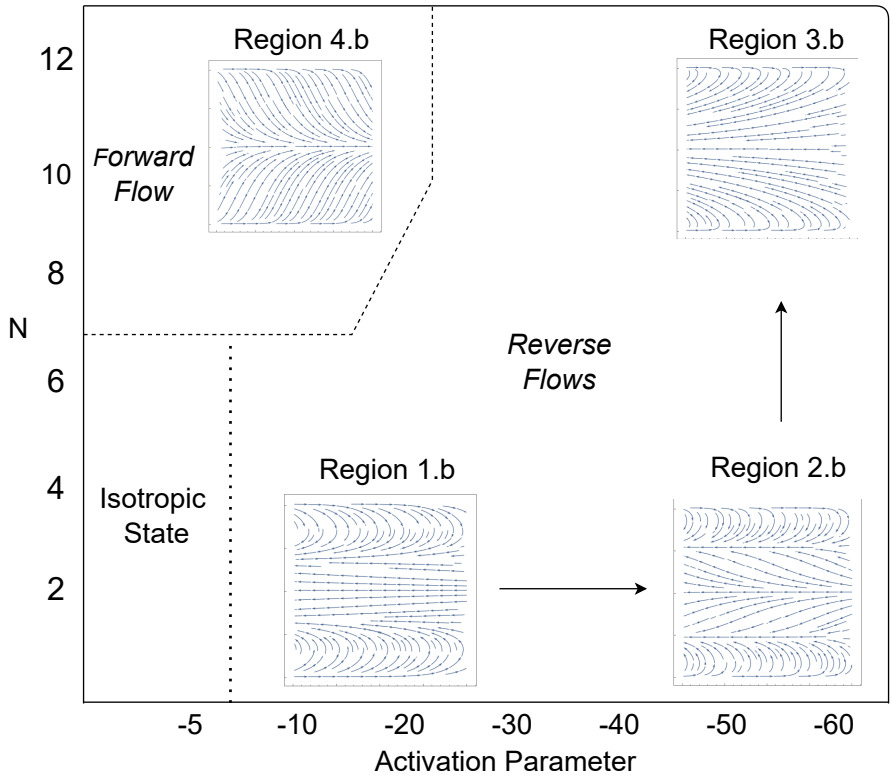

Figure 13: Phase diagram for Dirichlet boundary conditions with a negative activation parameter, showing simulation results for a $\sin 2\pi$ perturbation. Four distinct regions are identified. Transitioning geometries are denoted by arrows.

forward-pointing, parallel-anchored polarity vectors along channel walls, and an inner region displays a band of leftward-facing polarity vectors. As the liquid crystals shift away from the channel walls, we see an inward turning of the polarity vector until fully oriented leftward. One large spatially-symmetric band is seen in the center of the channel. The nematic director in Figure 14(b) shows the nematic director oriented in a way that shows reverse flow toward the center of the channel.

The spatially-symmetric polarity vector diagram in Figure 14(a) translates to a spatial profile of skew-symmetric polarity angle data in Figure 15(a). We view the large centerline band as it treads the horizontal axis. Order parameter data in Figure 15(b) shows that center half of the channel contains the highest degree of molecular order, a positive correlation to the density plot of Figure 14(b). Fluid velocity in Figure 15(c) is negative and is observed as a downward parabola, having a similar shape (albeit negative) and reaching a similar magnitude as the velocity observations in Region 1.a with $\sin \pi$ perturbation. Apparent stress is also similar in shape but is a horizontal reflection of $\sin \pi$'s Region 1.a. The graphs of the first and second normal stress differences, seen in Figure 15(e) and (f), are nearly identical to Region 1.a, despite the changes in perturbation and opposite polarity structure.

Region 2.b: Reverse Double Channel

Region 2.b couples a low nematic strength with a high activation parameter. One can see four distinct, spatially-symmetric regions in Figure 16(a)'s polarity vector diagram. We see a direct geometric correlation to Region 2.a Forward Double Channel's polarity diagram in Figure 7. In the center bands, the polarity vectors have an outward orientation, showing an alignment with polarity vectors off the boundary in two convergence zones. Despite the intricate geometries seen within the polarity vector plot, the nematic director diagram in Figure 16(b) retains the same geometry seen in the previous simulation's (Region 1.b) nematic plot.

In Figure 17, we plot the polarity angles of Region 2.a and Region 2.b together. The effects of the different wave numbers cause a flow reversal, but maintain near perfect symmetry between the two simulations. Steady state data shows an order parameter in Figure 18(b) that reaches its highest points along the outer defects, and a negative fluid velocity reaching

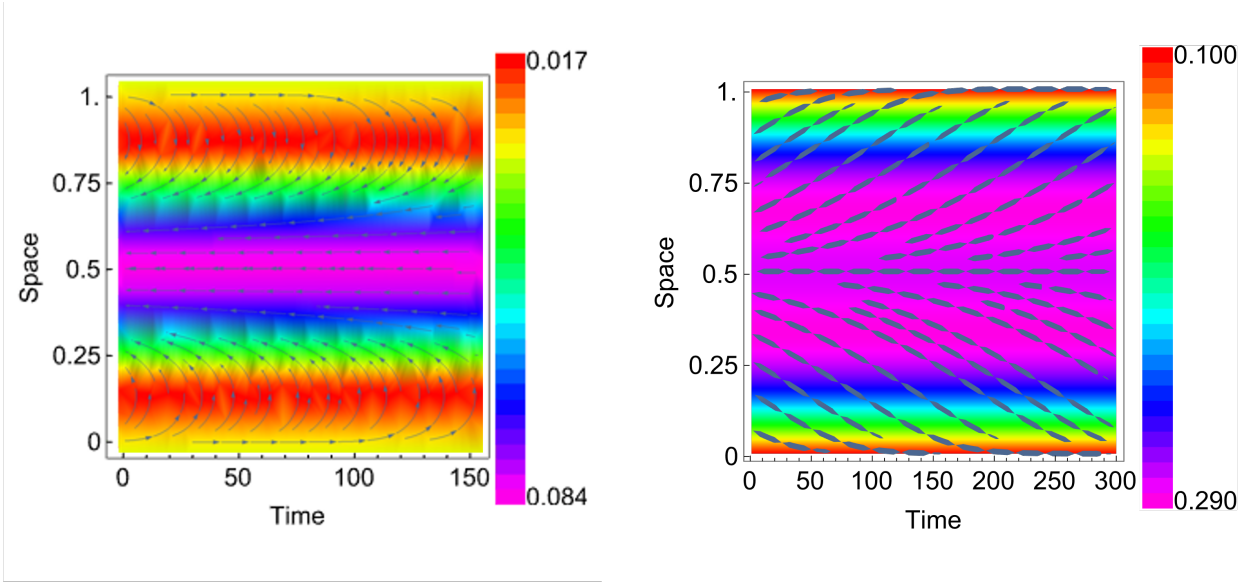

(a) Polarity vector at steady state.

(b) Nematic director at steady state.

Figure 14: Region 1.b: Polarity and Nematic Plots for $N = 4$ and $\zeta_a = -10$.

a similar magnitude as Region 2.a in the center of the channel. The spatial profile of apparent stress in Figure 18(d) is a near-exact reflection of $\sin \pi$'s apparent stress, with the lower half of the channel having a positive value, zero stress observed at centerline, and negative values of apparent stress in the upper half of the channel. Further comparisons observed are nearly identical first and second normal stress differences in Figure 18(e) and (f) at steady state. First normal stress is negative throughout the channel, and second normal stress is positive, both indicating the highest recordings along the outer defects.

Region 3.b: Simple Reverse Flow

Region 3.b contains simulations which pair a large nematic strength and a large activation parameter. Figure 19(a) shows polarity vectors pointing leftward. The nematic director observed in Figure 19(b) shows a very similar geometry to the polarity vector, with the horizontal band in the center indicating a high degree of orientational order. The spatial polarity angle in Figure 20(a) shows the quick directional change of the vectors near the channel walls, and the small rate of angular change through the inner channel. Order pa-

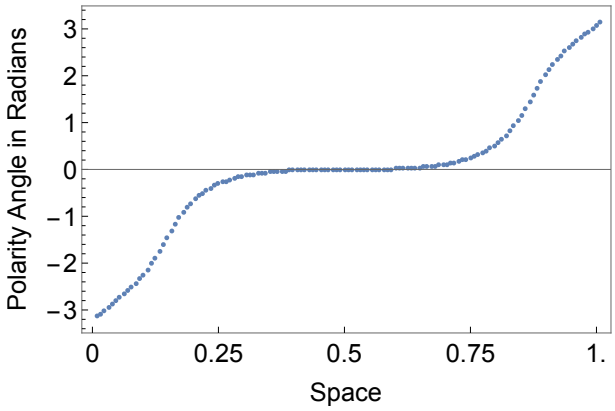

(a) Polarity angle over space.

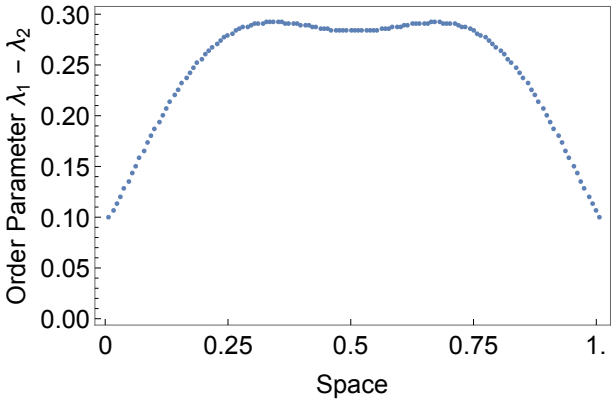

(b) Order parameter over space.

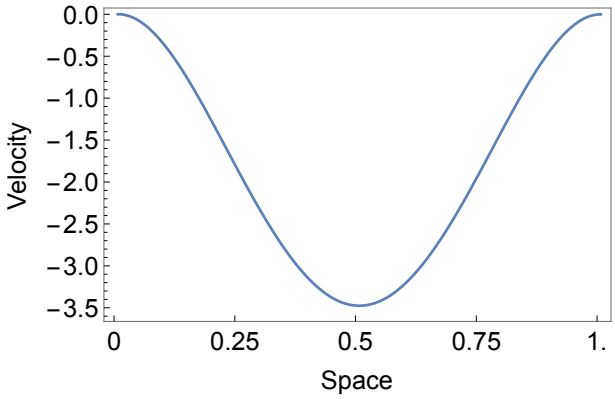

(c) Fluid velocity over space.

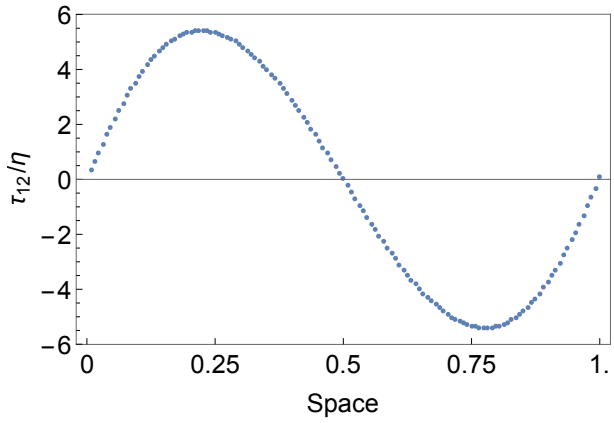

(d) Apparent stress over space.

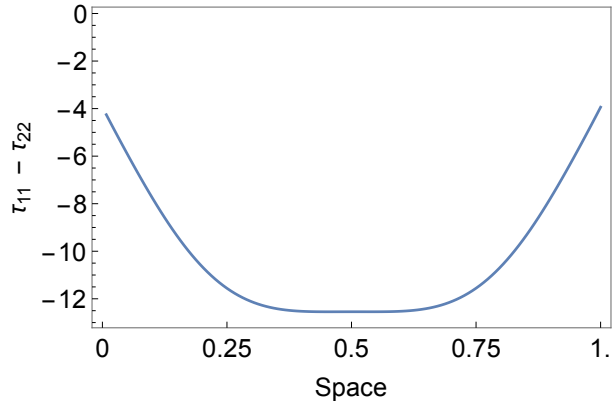

(e) First normal stress over space.

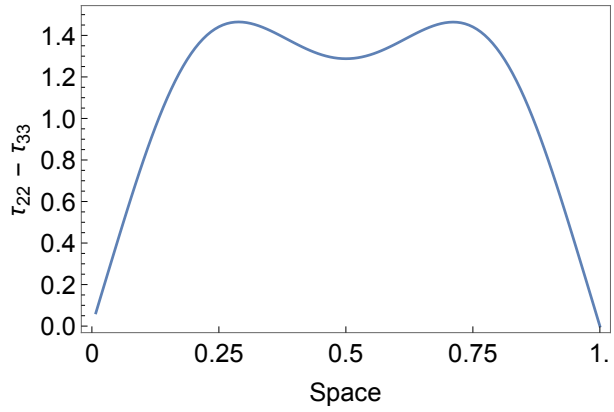

(f) Second normal stress over space.

Figure 15: Region 1.b: Rheological Properties for $N = 4$ and $\zeta_a = -10$.

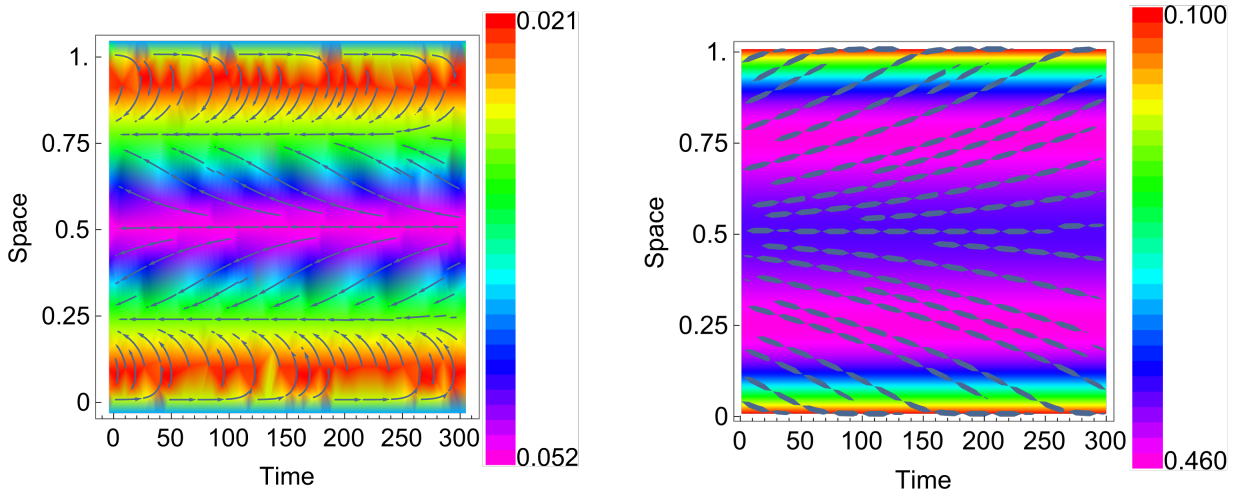

(a) Polarity vector at steady state.

(b) Nematic director at steady state.

Figure 16: Region 2.b: Polarity and Nematic Plots for $N = 2$ and $\zeta_a = -50$.

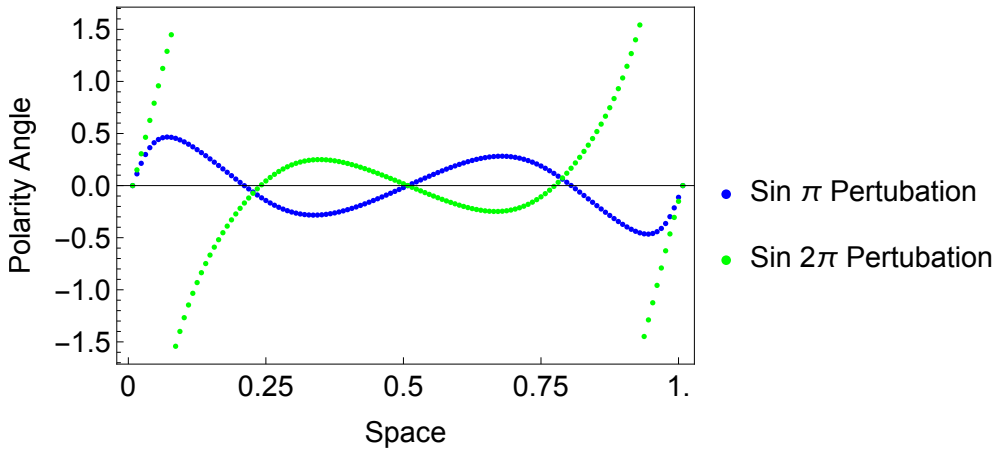

Figure 17: Polarity Angle Comparisons of Region 2.a and Region 2.b.

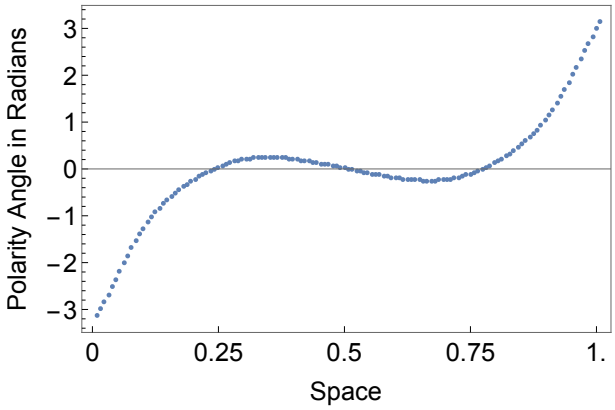

(a) Polarity angle over space.

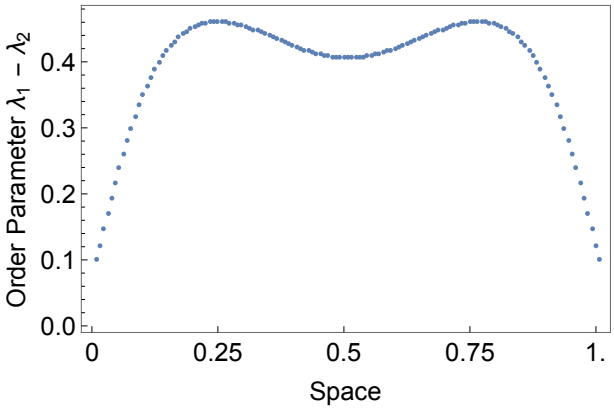

(b) Order parameter over space.

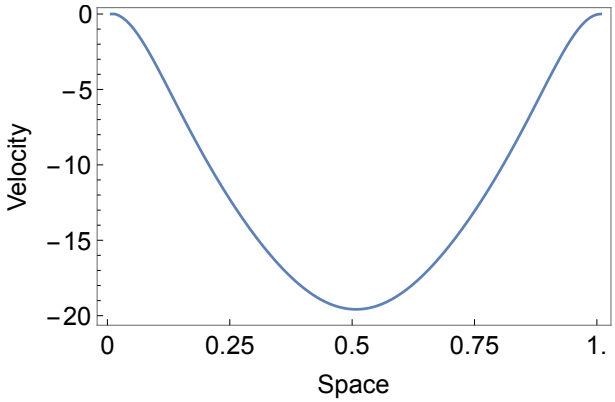

(c) Fluid velocity over space.

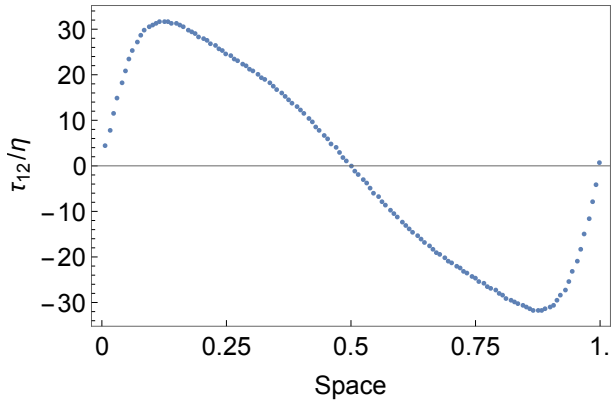

(d) Apparent stress over space.

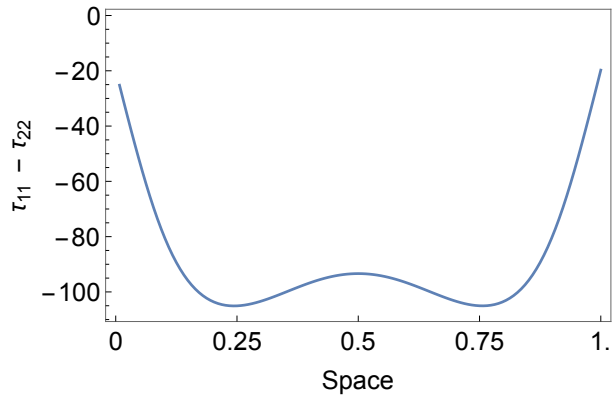

(e) First normal stress over space.

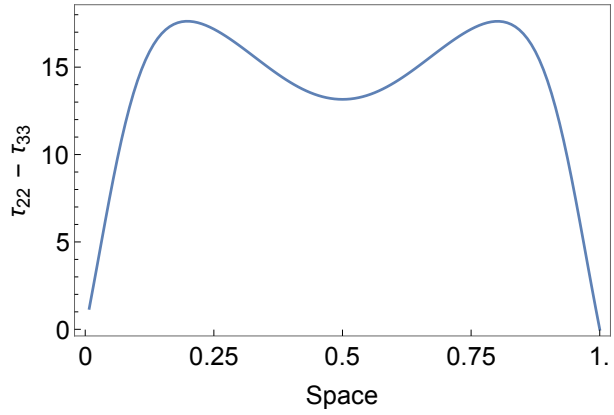

(f) Second normal stress over space.

Figure 18: Region 2.b: Rheological Properties for $N = 2$ and $\zeta_a = -50$.

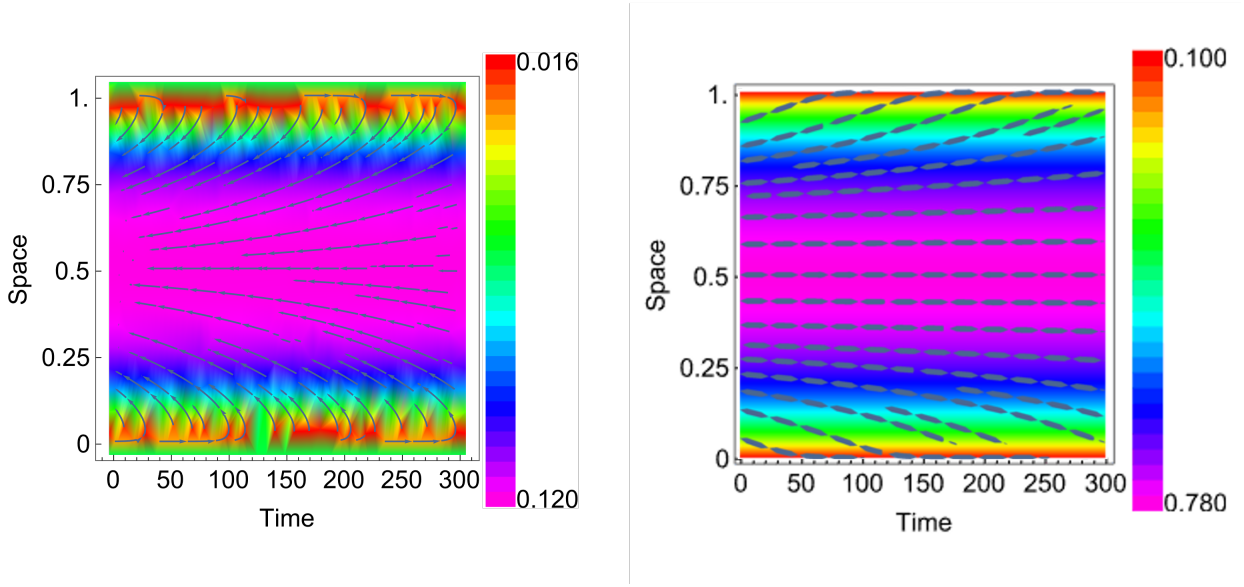

(a) Polarity vector at steady state.

(b) Nematic director at steady state.

Figure 19: Region 3.b: Polarity and Nematic Plots for $N = 12$ and $\zeta_a = -60$.

rameter in Figure 20(b) data matches the density plot of Figure 19(b), indicating the highest degree of order in the center of the channel. As seen in previous regions within this section, polarity vectors pointing left correlate to a negative velocity in Figure 20(c), with the center of the simulation recording the maximum velocity. Apparent stress in Figure 20(d) shows the highest magnitudes near the boundaries, with values close to zero in the center of the channel. Very high values of first normal stress in Figure 20(e) compare to those seen in Region 3.a. Both regions record this stress value as negative. The plot of second normal stress in Figure 20(f) is also identical to Region 3.a, with peaks near the outer boundaries of the channel.

Region 4.b: Forward Centerline Flow

When a high nematic strength is coupled with a low activation parameter, we see the only forwards flows with a $\sin 2\pi$ perturbation and a negative activation parameter. This section yields identical graphs to $\sin \pi$'s Region 4.a, indicating that when a high nematic strength is coupled with a low activation parameter, the resulting steady state remains

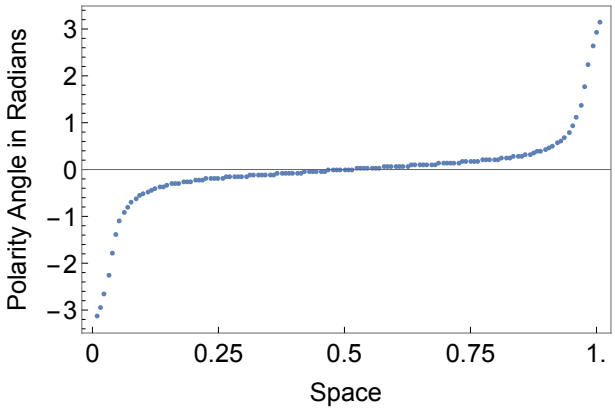

(a) Polarity angle over space.

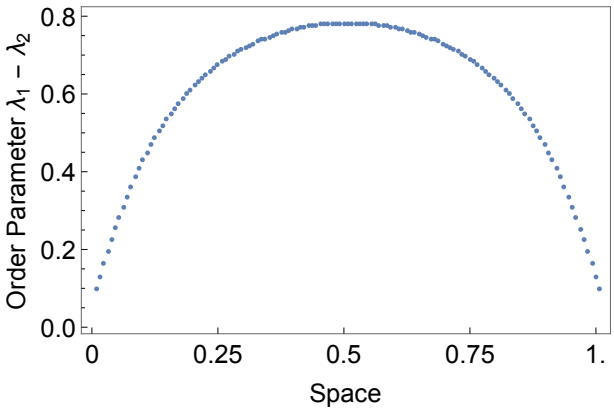

(b) Order parameter over space.

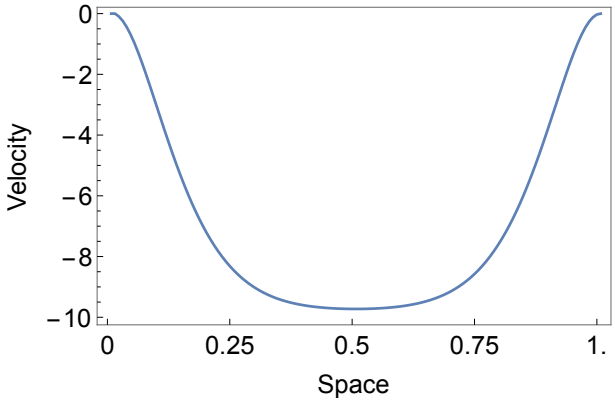

(c) Fluid velocity over space.

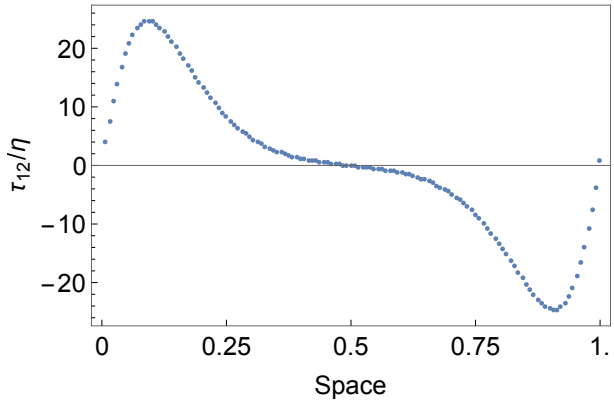

(d) Apparent stress over space.

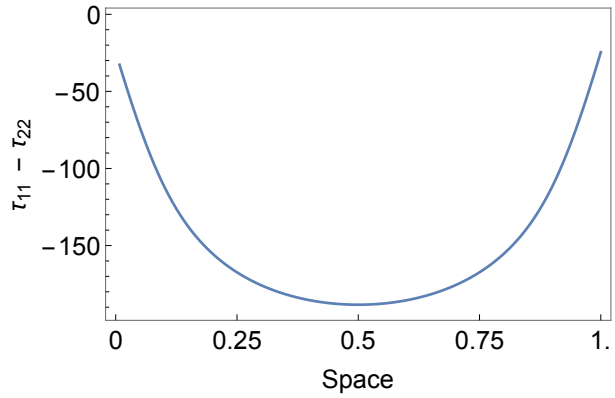

(e) First normal stress over space.

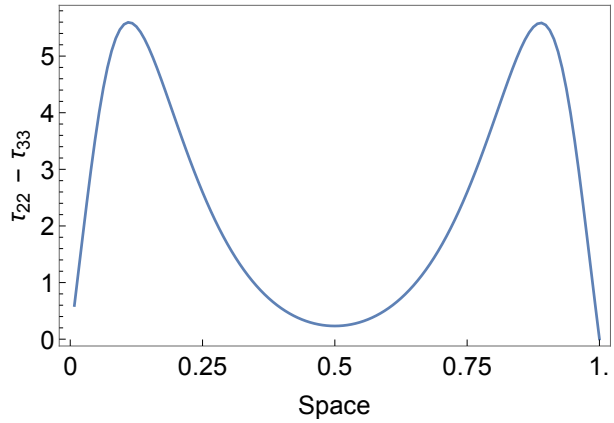

(f) Second normal stress over space.

Figure 20: Region 3.b: Rheological Properties for $N = 12$ and $\zeta_a = -60$.

unchanged by different initial perturbations.

3.1.3 SUMMARY

Within simulations of Dirichlet boundary conditions of parallel anchoring coupled with a negative activation parameter, all non-isotropic simulations ($N > 5$) produce spontaneous flows. Polarity vectors pointing right correlate to positive velocities, and polarity vectors pointing left indicate negative velocities. Despite the unusual geometries and patterns formed by the polymers, all velocity curves are of parabolic shape and velocity magnitude increases with an increasing ζ_a. Within Regions 1, 2, and 3, the differences in perturbations of $\sin \pi$ and $\sin 2\pi$ produce flow geometries containing many similarities–the polarity vector diagrams are near perfect reflections of the other. Their spatial profiles of velocity take identical shapes and reach the same maximum values, but are positive for $\sin \pi$ and negative for $\sin 2\pi$. The skew-symmetric spatial profiles of apparent stress between the two perturbations produce graphs with reflective symmetries. Order parameter figures, as well as first and second normal stress differences are unchanged by a change in perturbation. In between Regions 1, 2, and 3, transitional geometry of the polarity vector diagrams is seen between the regions. Unlike Regions 1-3, Region 4 simulations, with high nematic strengths and a small activation parameter, produce the same geometric results despite the change in perturbation wave number.

3.2 SIMULATIONS WITH PARALLEL ANCHORING AND PULLER-LIKE BEHAVIOR

This section of results continue with parallel anchoring simulations but now contain a positive activation parameter. A positive ζ_a indicates puller-like behavior of the polymer on surrounding particles. This section and subsequent simulations contain results for a $\sin 2\pi$ perturbation. Simulation results yield both steady states and periodic states as shown in the phase diagram of Figure 21. The named regions parameter data is listed in Table 6. The steady state flows subdivide into two categories: Outward flow and Inward flow. Two different types of periodic states are observed, containing different geometries and wave period length. Note the phase diagram's lower boundary of nematic strength is at $N = 8$.

Geometry Name	Nematic Strength	Active Strength
Steady State Outward Flow	$N = 12$	$\zeta_a = 10$
Steady State Inward Flow	$N = 8$	$\zeta_a = 20$
Periodic State, Type I	$N = 10$	$\zeta_a = 7$
Periodic State, Type II	$N = 12$	$\zeta_a = 30$

Table 6: Description of Observed States.

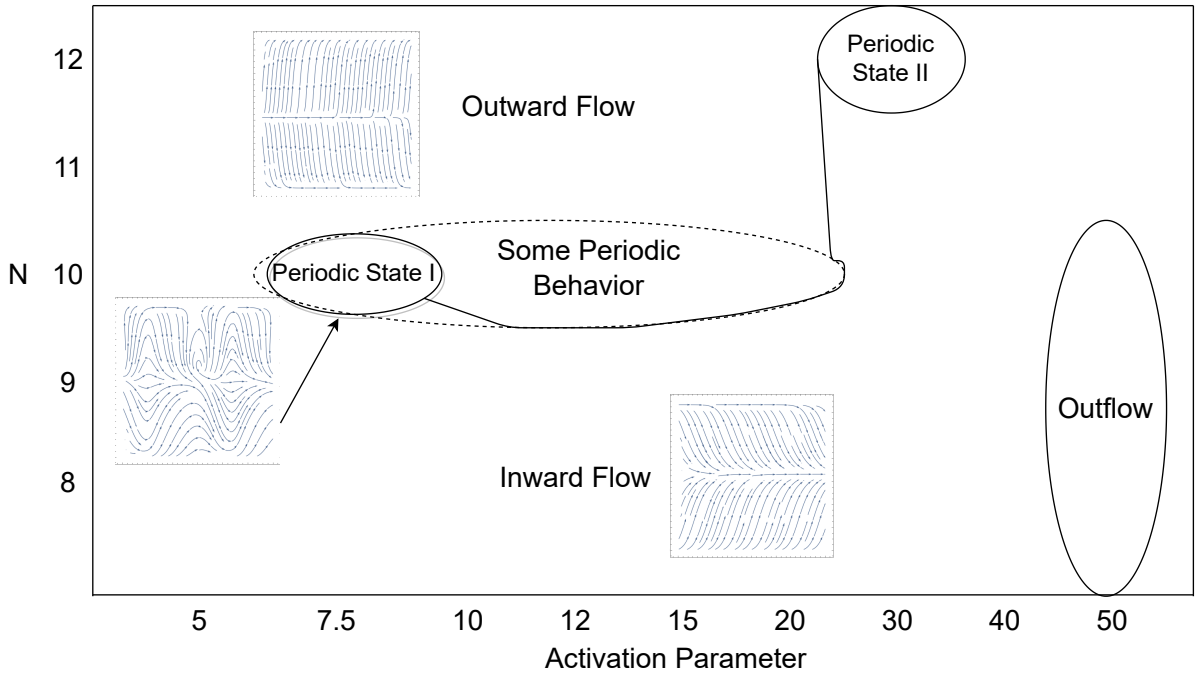

Figure 21: Phase Diagram for Dirichlet Boundary Conditions III.

Lower values of nematic strength in simulations produce isotropic results.

3.2.1 STEADY STATE OUTWARD FLOW

Simulations in this section pair a high activation parameter with a low to intermediate activation parameter for steady state convergence. Outward flow is characterized by polarity vector diagram in Figure 22(a), where the polarity vectors orient outwards toward the channels walls. Nematic orientation differs greatly, as seen in Figure 22(b), with the nematic director in a vertical position throughout the center of the channel. Along the channel walls,

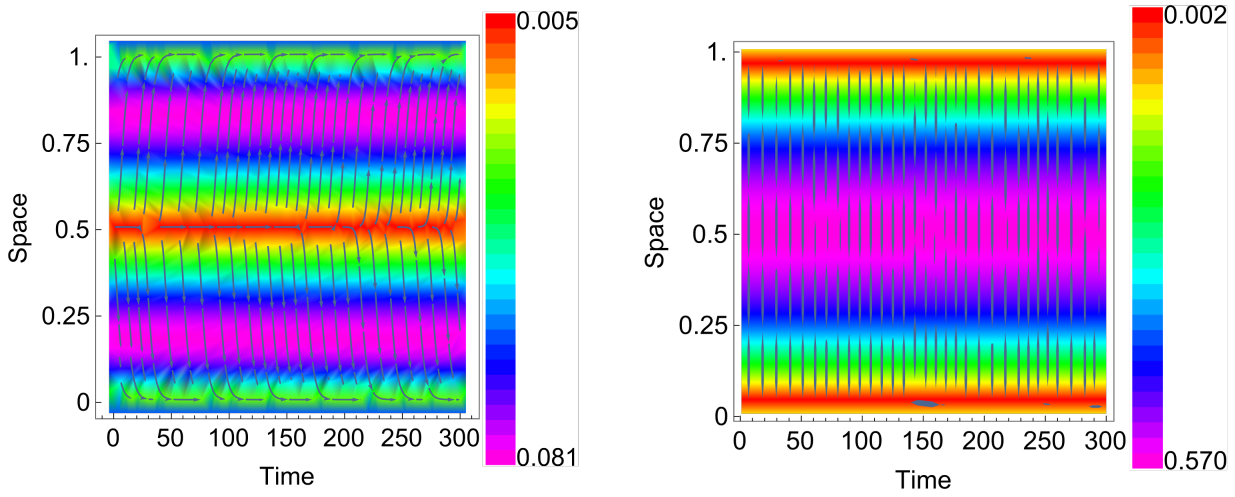

(a) Polarity vector at steady state.

(b) Nematic director at steady state.

Figure 22: Outward Flow: Polarity and Nematic Plots for $N = 12$ and $\zeta_a = 10$.

we see the nematic director oriented horizontally along channel walls.

In Figure 23(a)'s steady state rheological data, we see the polarity vector spatial profile with skew-symmetric symmetry, indicating similar angular measures in each half of the channel. Order parameter data in Figure 23(b) measures highest in the center of the channel, with two small jumps near each boundary. In a noticeable change from the previous sections containing a negative value of activation parameter, we see a rightward-pointing polarity vector not indicative of a positive velocity. The spatial profile of fluid velocity in Figure 23(d) shows a negative velocity throughout the channel, and velocity magnitude is considerably small. Apparent stress in Figure 23(d) spatial profile is skew-symmetric and records very small values. The first normal stress difference in Figure 23(e) is negative everywhere except at the boundaries, while the second normal stress difference is positive and parabolic in shape. Both normal stress differences reach their maximum value in the center of the channel.

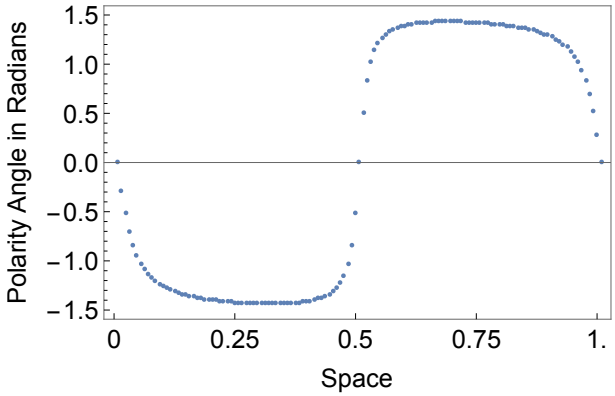

(a) Polarity angle over space.

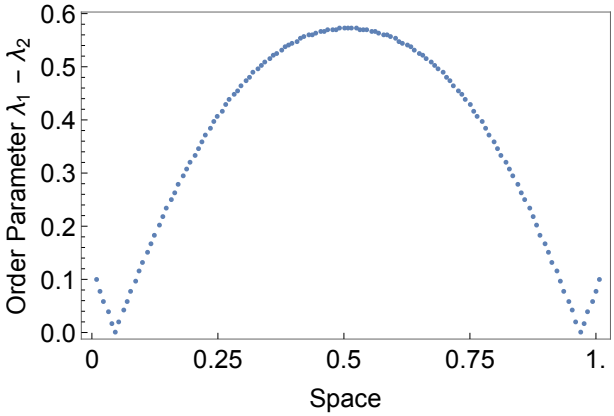

(b) Order parameter over space.

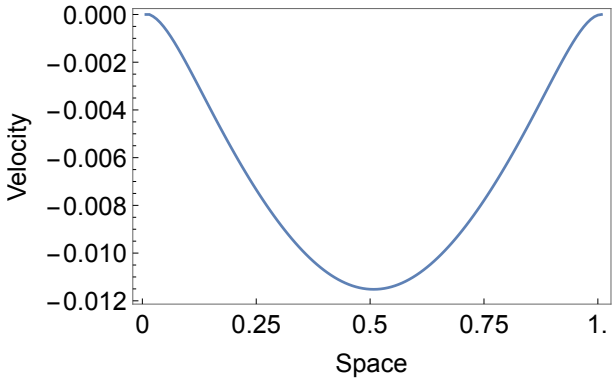

(c) Fluid velocity over space.

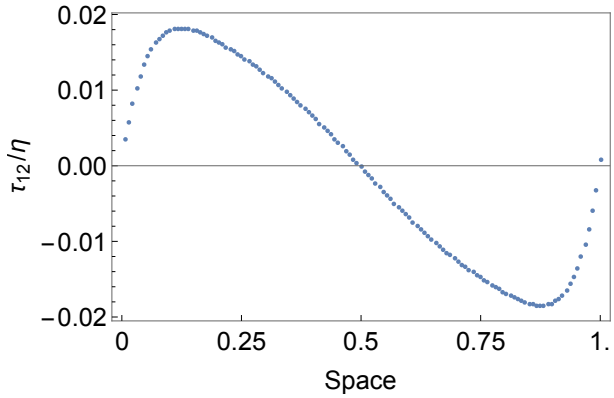

(d) Apparent stress over space.

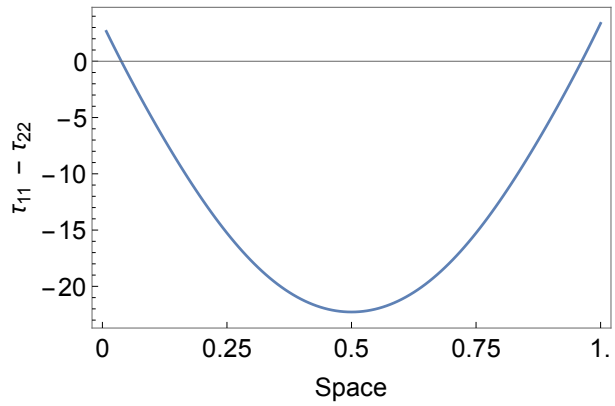

(e) First normal stress over space.

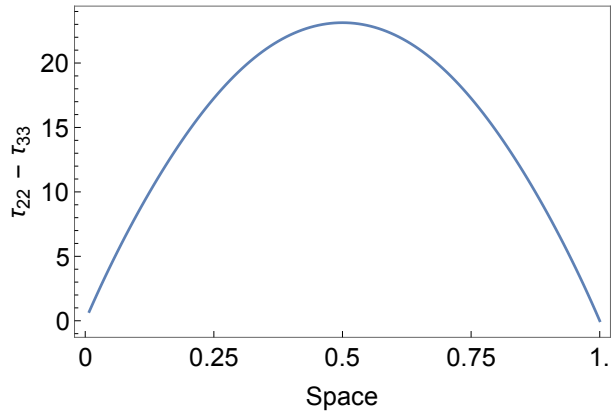

(f) Second normal stress over space.

Figure 23: Outward Flow: Rheological Properties for $N = 12$ and $\zeta_a = 10$.

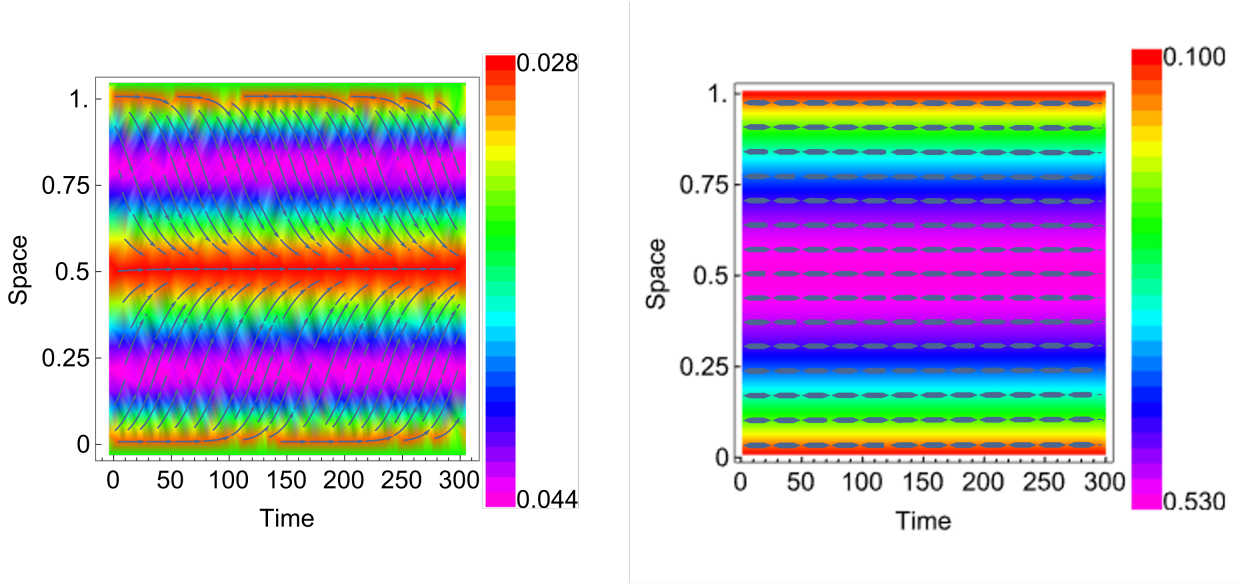

(a) Polarity vector at steady state.

(b) Nematic director at steady state.

Figure 24: Inward Flow: Polarity and Nematic Plots for $N = 8$ and $\zeta_a = 20$.

3.2.2 STEADY STATE INWARD FLOW

Inward flow is observed in multiple areas of our phase diagram in Figure 21; this section presents results with $N = 8$ and $\zeta_a = 20$. Resulting geometry is similar in structure to Region 4 of the previous section ($\zeta_a < 0$). In the polarity vector diagram in Figure 24(a), we see parallel anchoring along channel walls and vectors pointing inward towards center of the channel. The nematic director in Figure 24(b) is horizontal throughout the entire channel.

Steady state rheological data is presented in Figure 25. The spatial profile of polarity angle in Figure 25(a) shows two regions of positive and negative angle measurement. Order parameter data in Figure 25(b) confirms the density plot in Figure 24(b), with proximity to the center of the channel indicating higher orientational order. The profile of fluid velocity in Figure 25(c) maintains parabolic shape and indicates negative velocity in the channel. Similar to Outward flow, the polarity vector direction no longer correlates to the direction of velocity. The profile of apparent stress in Figure 25(d) shows very low values but maintains a similar shape to apparent stress of Outward flow. First normal stress difference in Figure 25(e) is positive throughout the channel. Second normal stress difference in Figure 25(f)

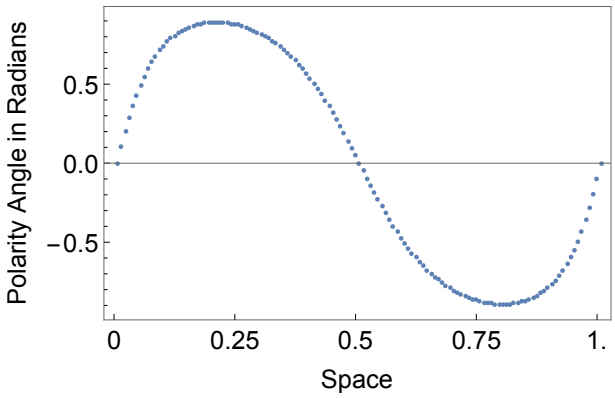

(a) Polarity angle over space.

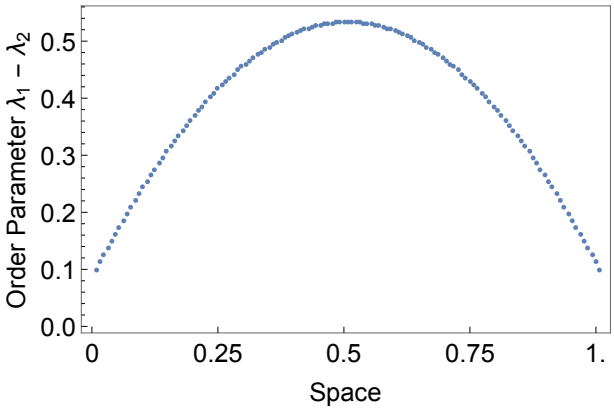

(b) Order parameter over space.

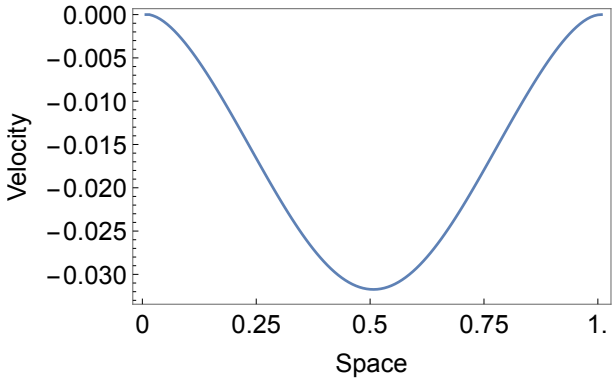

(c) Fluid velocity over space.

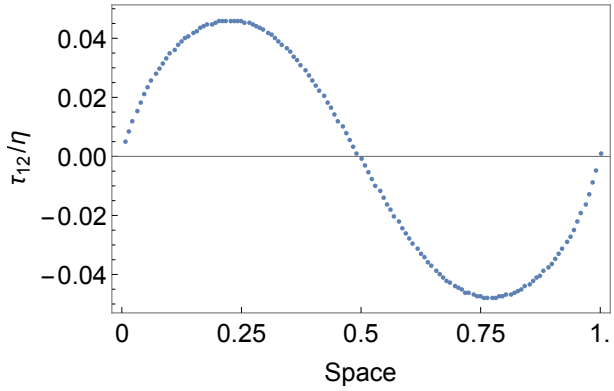

(d) Apparent stress over space.

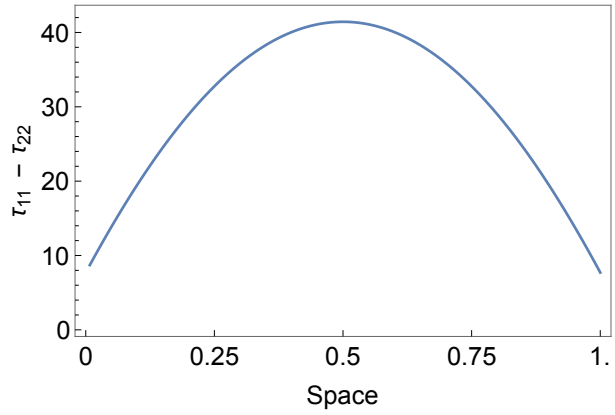

(e) First normal stress over space.

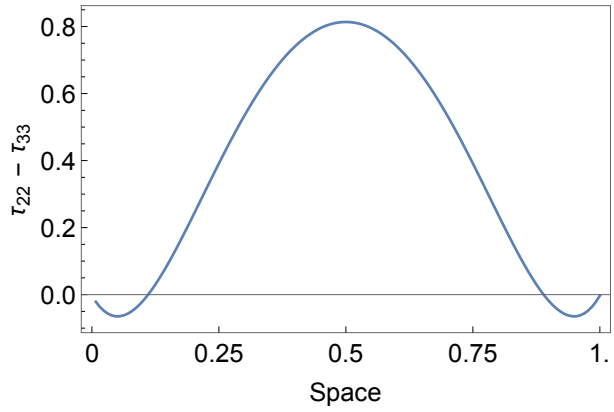

(f) Second normal stress over space.

Figure 25: Inward Flow: Rheological Properties for $N = 8$ and $\zeta_a = 20$.

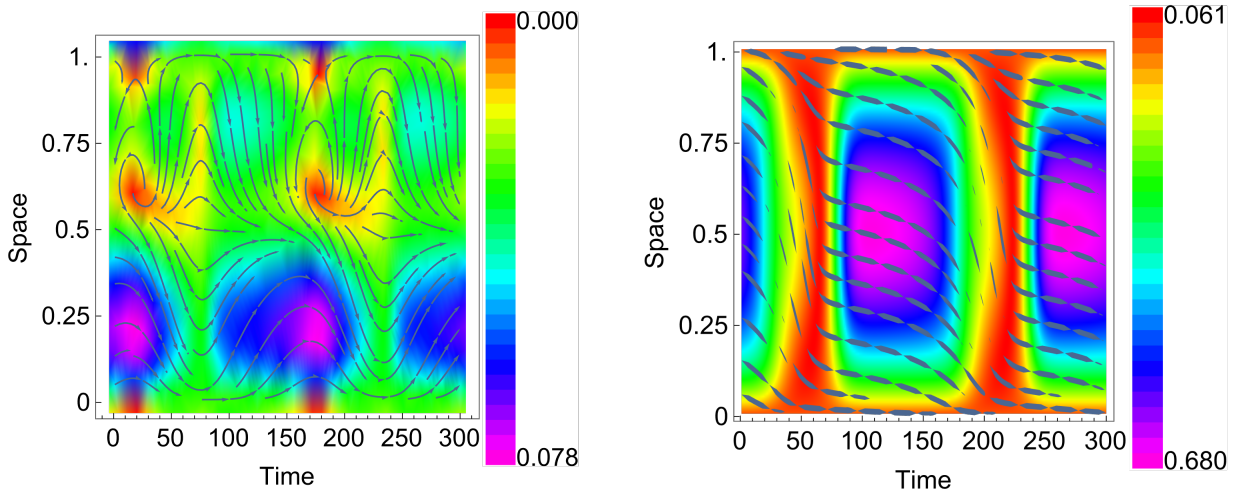

(a) Polarity vector.

(b) Nematic director.

Figure 26: Periodic State I: Polarity and Nematic Plots for $N = 10$ and $\zeta_a = 7$.

is also positive with the exception of the boundary areas. Both normal stress differences reach their maximum value in the center of the channel.

3.2.3 PERIODIC STATE TYPE I

The first of two periodic states observed within Dirichlet boundary conditions, the Type I periodic state is observed when $N = 10$ and $7 \leq \zeta_a \leq 8$. As seen in the phase diagram in Figure 21, when nematic strength is held constant at $N = 10$ and activation parameter is increased, we see some form of periodic behavior within the simulation until $\zeta_a = 25$, at which our simulations revert to inward flow. Type I periodic state has the larger wave period length of the two types: we measure 160 times units per cycle. The simulation achieves periodic state early in the simulation and maintains a stable frequency. The polarity vector and nematic director plots are seen Figure 26. Both graphs show geometry changes within one cycle. The polarity vector appears to switch from outflow-type to inflow-type geometry. The changes of the nematic director orientation within one cycle appear as if a wave is moving through the channel.

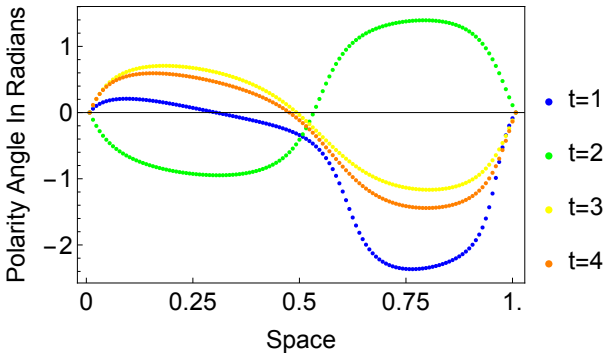

(a) Polarity angle over space.

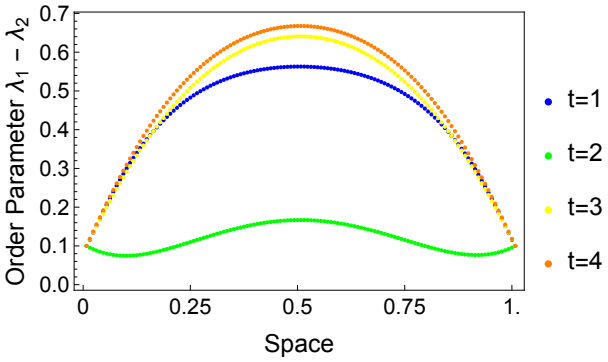

(b) Order parameter over space.

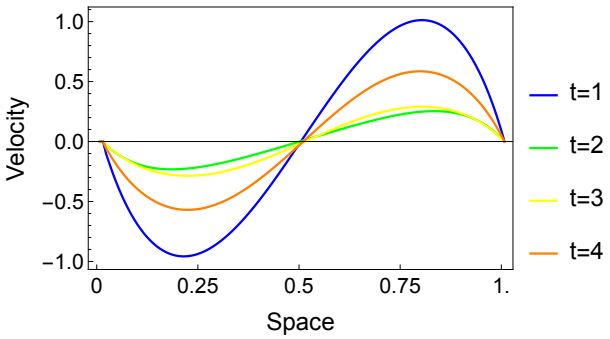

(c) Fluid velocity over space.

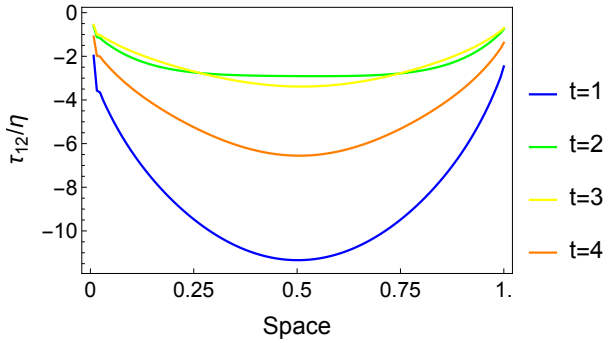

(d) Apparent stress over space.

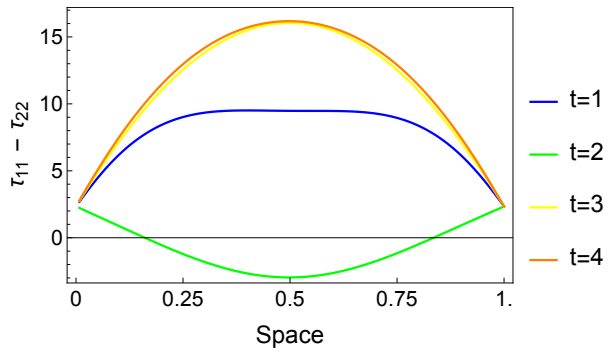

(e) First normal stress over space.

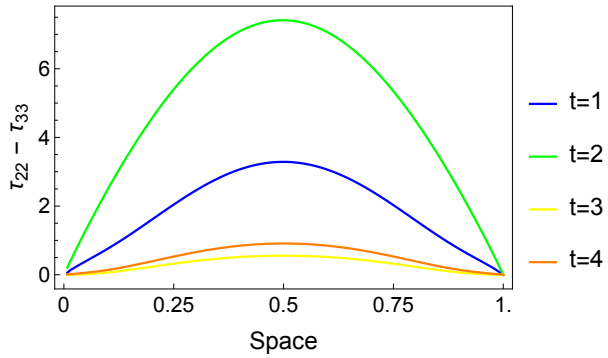

(f) Second normal stress over space.

Figure 27: Periodic State I: Rheological Properties for $N = 10$ and $\zeta_a = 7$.

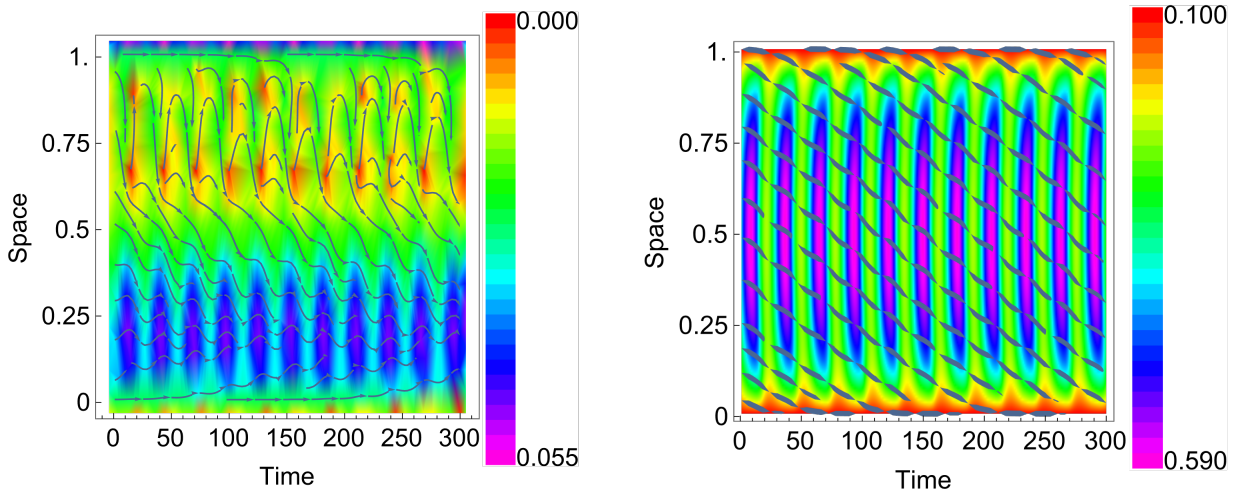

(a) Polarity vector.

(b) Nematic director.

Figure 28: Periodic State II: Polarity and Nematic Plots for $N = 12$ and $\zeta_a = 30$.

Figure 27 shows the rheological data at four equidistant points in time within one cycle. Polarity angle over space in Figure 27(a) shows the movement from inflow to outflow orientation. The non-symmetric value at $t = 1$ reflects the "swirl" seen in the upper half of the polarity vector diagram in Figure 26(a). The order parameter data in Figure 27(b) graphs show the range at which crystalline orientational order oscillates; we see high values near 0.7 but also see a decrease to 0.1 within one cycle. Fluid velocity in Figure 27(c) maintains a symmetric waveform that fluctuates in magnitude. Apparent stress in Figure 27(d) measures negative throughout the cycle and shows the stress magnitudes fluctuate between $2.5 < \tau_{12}/\eta < 11.5$ in the center of the channel. The first normal stress difference in Figure 27(e) is mostly parabolic in shape and fluctuates from positive to negative through one cycle. The second normal stress difference in Figure 27(f) maintains positive values through the cycle.

3.2.4 PERIODIC STATE TYPE II

The second of two periodic states with Dirichlet boundary conditions, Type II periodic state is observed when $N = 12$ with $\zeta_a = 30$. Type II periodic state has a much smaller wave

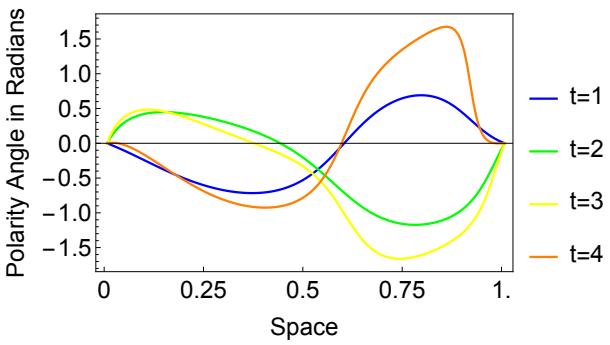

(a) Polarity angle over space.

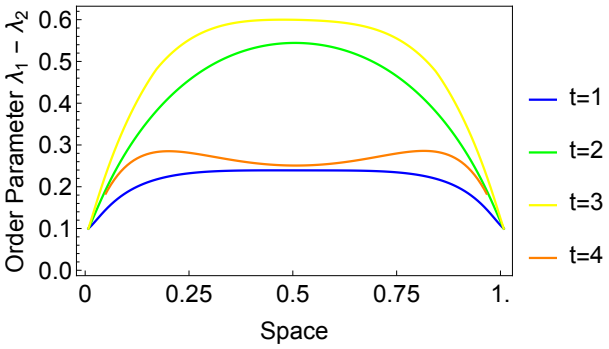

(b) Order parameter over space.

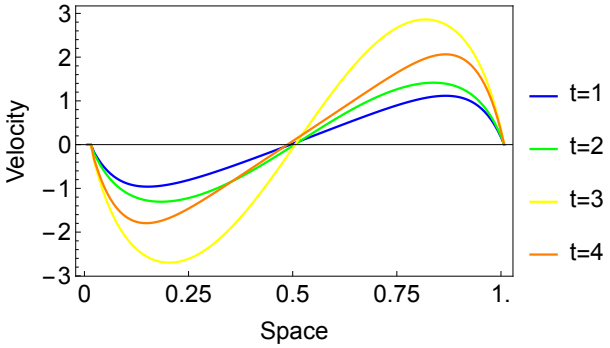

(c) Fluid velocity over space.

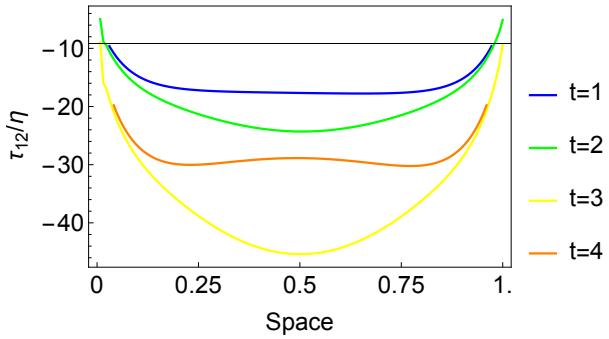

(d) Apparent stress over space.

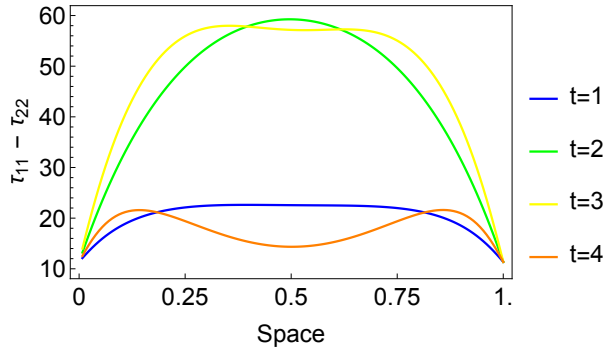

(e) First normal stress over space.

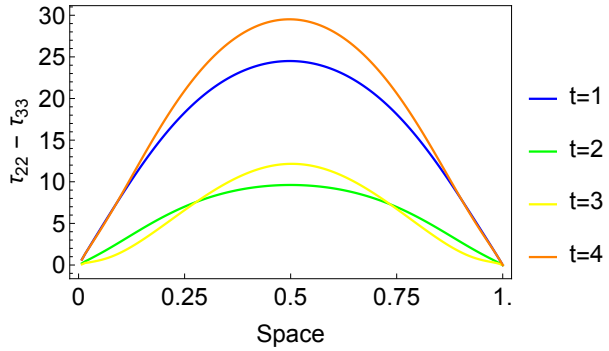

(f) Second normal stress over space.

Figure 29: Periodic State II: Rheological Properties for $N = 12$ and $\zeta_a = 30$.

period length of 30 time units, as compared to Type I's 160 time units. While some anti-symmetries are visible in the polarity vector graphs, symmetry is achieved in the nematic director plot as well as in the velocity, order parameter, and the stress plots. In Figure 28, we see erratic behavior in the polarity vector, with the upper half of the channel containing vertical swirls and the lower half of the channel presenting some sort of forward flow. In Figure 29(a), the polarity angle over space throughout one cycle, again shows non-symmetric inward and outward orientations over one cycle, viewed as waves in Figure 28(a). The nematic director in Figure 28(b) shows an angled orientation of the vectors, with periodic state visible within the order parameter density plot. This fluctuation in order parameter is also shown in Figure 29(b). Fluid velocity in Figure 29(c) maintains a symmetric waveform which fluctuates in magnitude throughout the cycle, as it does in Type I's observation. Apparent stress in Figure 29(d) measures mostly negative, except at certain points in the cycle along the boundaries. First and second normal stresses in Figures 29(e) and (f), measure positive throughout the simulation with high magnitudes.

3.2.5 SUMMARY

Simulations with Dirichlet boundary conditions with a positive activation parameter produce spontaneous flows with nematic strengths of $N \geq 8$. Both steady states and periodic states are observed. In contrast to simulations from the previous section with a negative activation parameter, polarity vector orientation does not correlate to the sign of velocity. Steady state simulations produce symmetric geometries with an initial spike of fluid velocity, but steady state velocity is zero.

3.3 SIMULATIONS WITH NORMAL ANCHORING AND PUSHER-LIKE BEHAVIOR

The following section contains results of Dirichlet boundary conditions on the polarity vector as normal anchoring along channel walls. All simulations with normal anchoring conditions contain negative activation parameters, as simulations with positive activation parameters yield only isotropic results. As seen in the range of axes in Figure 30's phase diagram, only low values of nematic strength coupled with low activation parameters produce

Geometry Name	Nematic Strength	Active Strength
Steady State Bended Flow	$N = 4$	$\zeta_a = 4$
Steady State Wiggle Flow	$N = 6$	$\zeta_a = 2$

Table 7: Description of Observed States.

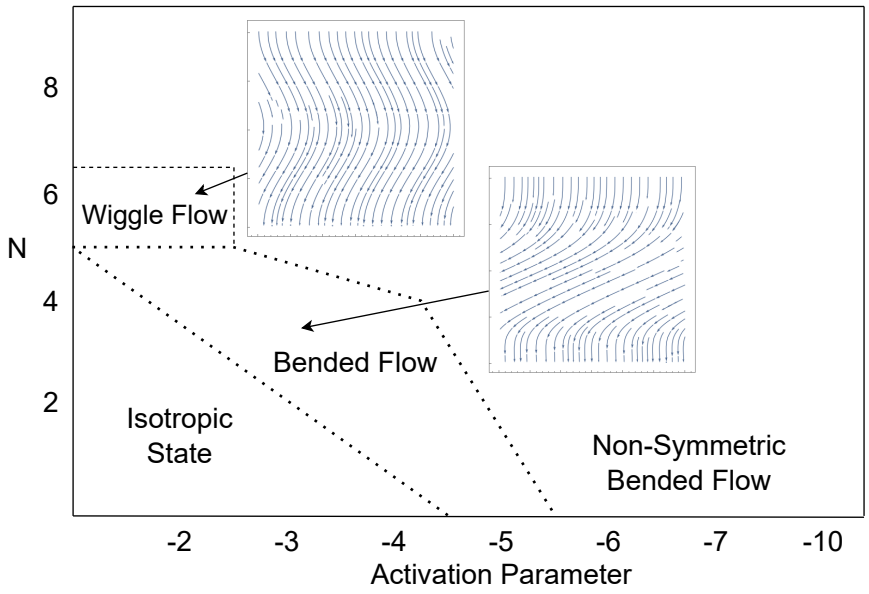

Figure 30: Phase Diagram for Dirichlet Boundary Conditions IV.

spontaneous flows. When both nematic strength and activation parameter are less than four, isotropic states are observed. The two observed regions with normal anchoring are shown in Figure 30 with their specific parameters listed in Table 7. Outside of isotropic state and two steady state named regions, the simulations produce anti-symmetric results, which are not studied in this report.

3.3.1 STEADY STATE BENDED FLOW

The first of two regions observed with normal anchoring, Bended flow refers to the steady state geometry of the polarity vectors shown in Figure 31(a). We see the polymer's perpendicular anchoring position along the channel walls. The vectors orient downward, sharply bend to the left, and then regain their straight downward position. The nematic

director in Figure 31(b) shows a noticeably different geometry as compared to the polarity vector. The upper half of the channel matches the polarity vector with a leftward shift, but the lower half of the channel is oriented in the opposite direction. Within the nematic plot, a defect is observed along the center of the channel, but has no direct correlation to the polarity vector's geometry.

Steady state rheological data is found in Figure 32. We observe the spatial profile of the polarity vector in Figure 32(a) as slightly anti-symmetric, with a more rapid rate of angular change in the lower half of the channel. Order parameter in Figure 32(b) takes an interesting shape, but the small, low-valued range of the graph discounts that actual changes occurring in the simulation are not drastic. The two purple-colored bands observed in the nematic director density plot correlate to the two peaks observed in the order parameter spatial profile. In this simulation, our leftward-pointing polarity vector correlates to a negative velocity over space in Figure 32(c). We observe maximum velocity in the center of the channel. Apparent stress in Figure 32(d) is observed as a symmetric wave. First normal stress in Figure 32(e) is positive near channel walls, but reaches negative values in the center of the channel. Second normal stress in Figure 32(f) is negative and is highest nearest the channel boundaries.

3.3.2 STEADY STATE WIGGLE FLOW

The second type of spontaneous flow with normal anchoring resembles a slight shift of polarity vector orientation, and then a shift back to original alignment, resembling a "wiggle" of polymer orientation, as seen in Figure 33. The lower half of the channel contains vectors oriented rightward, correlating to a positive velocity (seen in Figure 34(c)), while the upper half of the channel has leftward orientation and a negative velocity. This is consistent to what is observed in the previous normal anchoring simulation and for parallel anchoring when $\zeta_a < 0$. We see the nematic director in Figure 33(b) aligned vertically with a slight shift, albeit in the opposite direction of the shift observed in the polarity diagram.

Within the steady state rheological data in Figure 34, we observe the order parameter in Figure 34(b) peak in the center of the channel. Apparent stress in Figure 34(d) is parabolic in shape and peaks in the center of the channel. First normal stress difference in Figure 34(e)

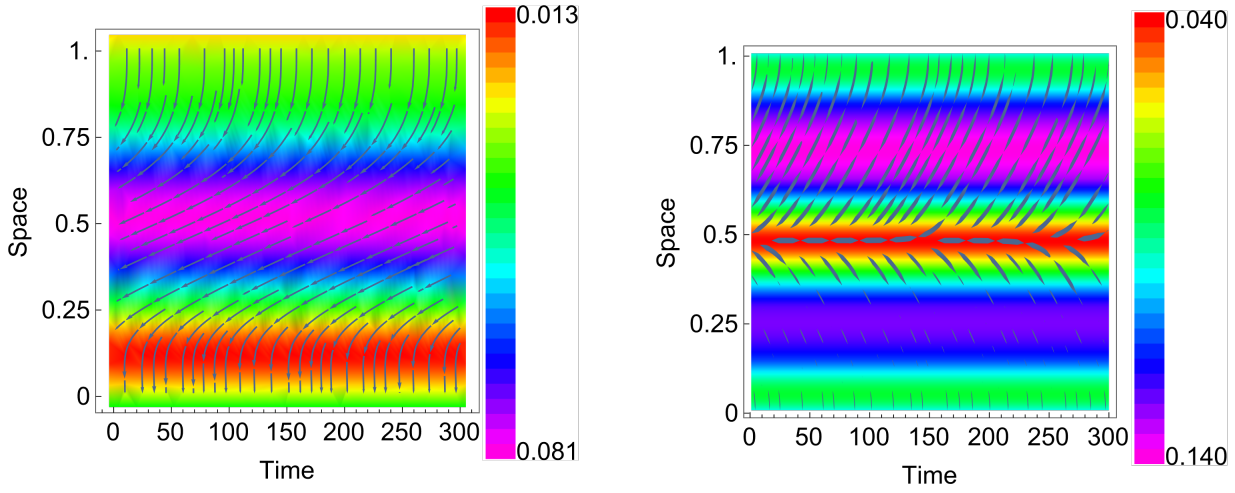

(a) Polarity vector at steady state.

(b) Nematic director at steady state.

Figure 31: Bended Flow: Polarity and Nematic Plots for $N = 4$ and $\zeta_a = 4$.

measures between $0.65 < \tau_{11} - \tau_{22} < 0.95$, very low values with a similarly small range. Second normal stress difference in Figure 34(f) take a parabolic downward shape, having negative values across the channel, also within a small range.

3.3.3 SUMMARY

Simulations with normal anchoring of the polarity vector under Dirichlet boundary conditions produce spontaneous flows when $\zeta_a < 0$. Only two regions of interest exist, as isotropic results occur when $(N < 5) \cup (\zeta_a < -4.5)$. Outside of these regions, simulations with larger values of N and $|\zeta_a|$ result in unstable, non-symmetric geometries. The two regions observed, Bended flow and Wiggle flow, both reach steady state and maintain a constant fluid velocity. Further, polarity vector direction indicates fluid velocity direction, as seen previously with parallel anchoring simulations with negative activation parameters.

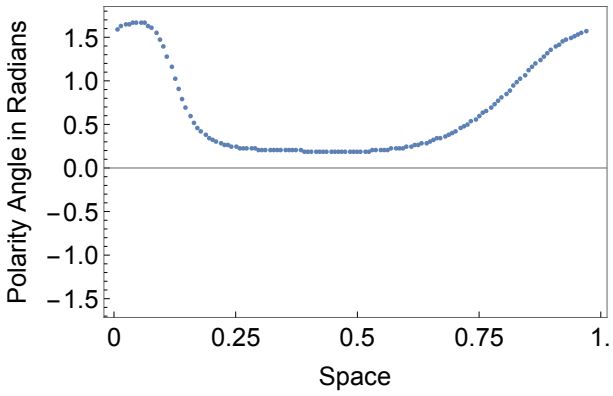

(a) Polarity angle over space.

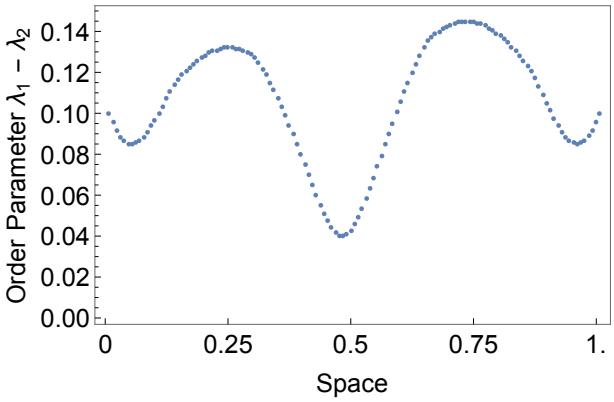

(b) Order parameter over space.

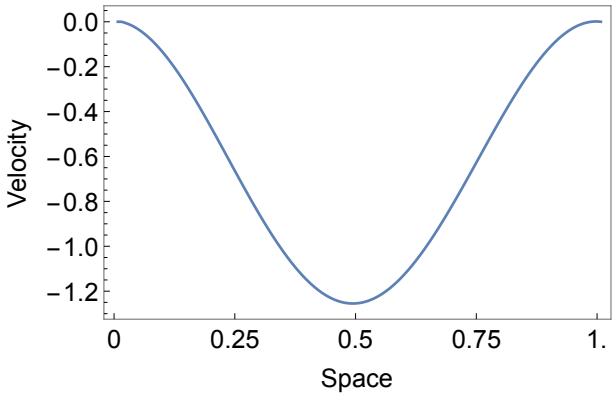

(c) Fluid velocity over space.

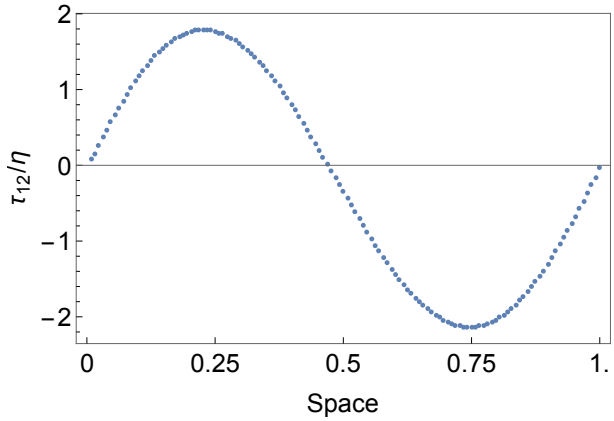

(d) Apparent stress over space.

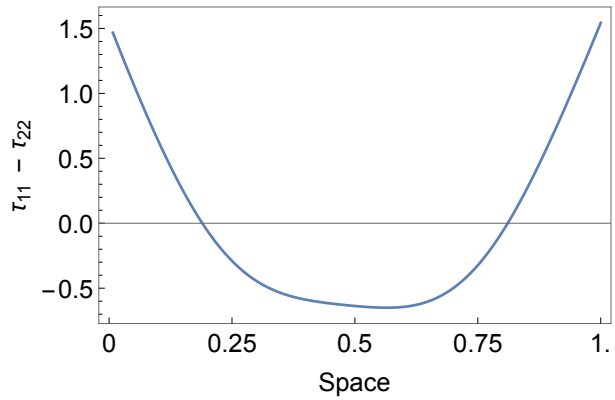

(e) First normal stress over space.

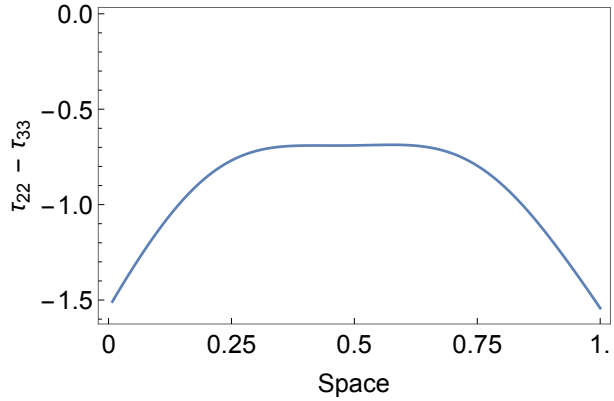

(f) Second normal stress over space.

Figure 32: Bended Flow: Rheological Properties for $N = 4$ and $\zeta_a = 4$.

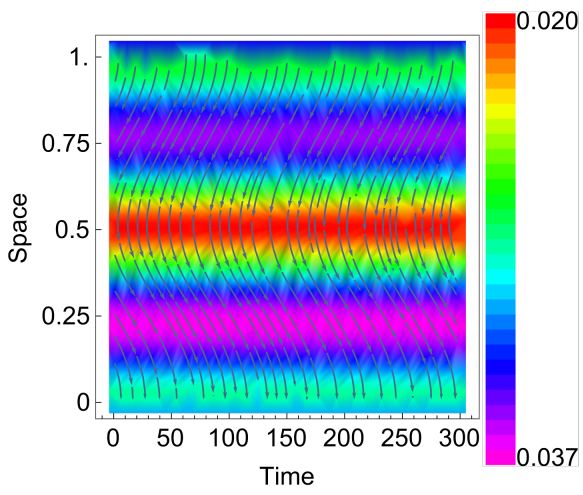

(a) Polarity vector at steady state.

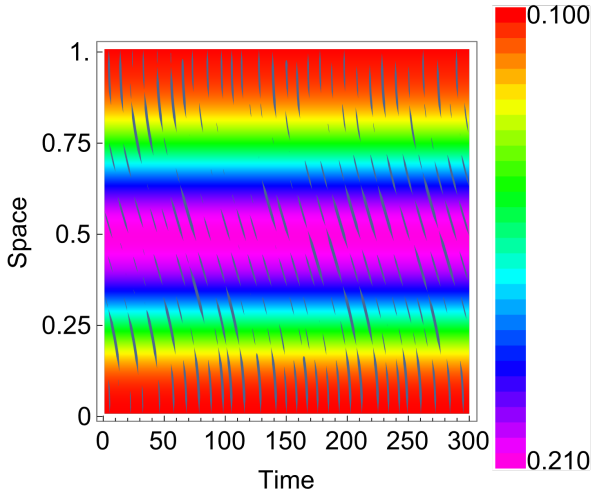

(b) Nematic director at steady state.

Figure 33: Wiggle Flow: Polarity and Nematic Plots for $N = 6$ and $\zeta_a = 2$.

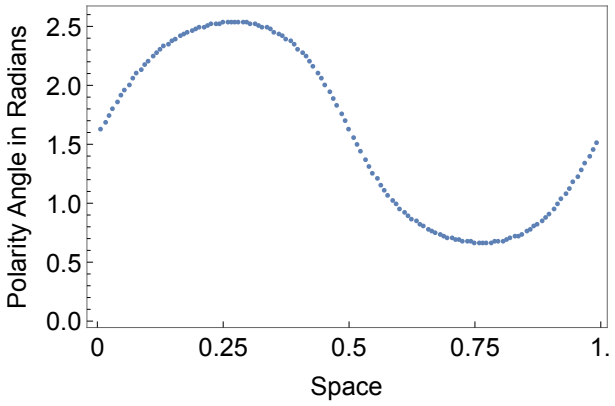

(a) Polarity angle over space.

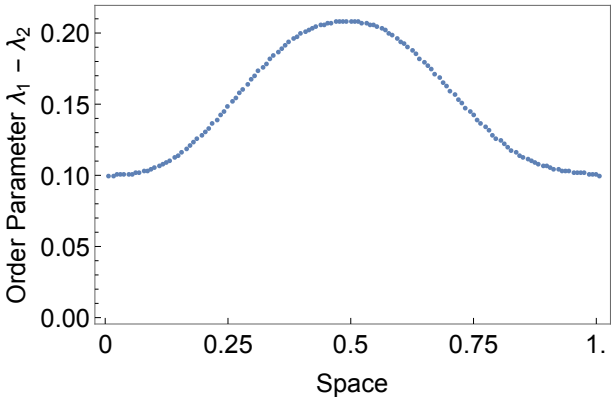

(b) Order parameter over space.

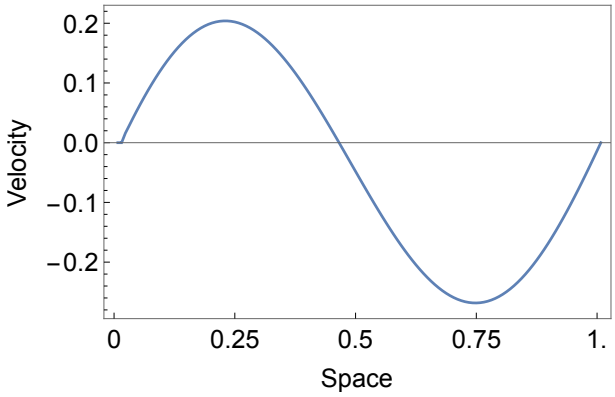

(c) Fluid velocity over space.

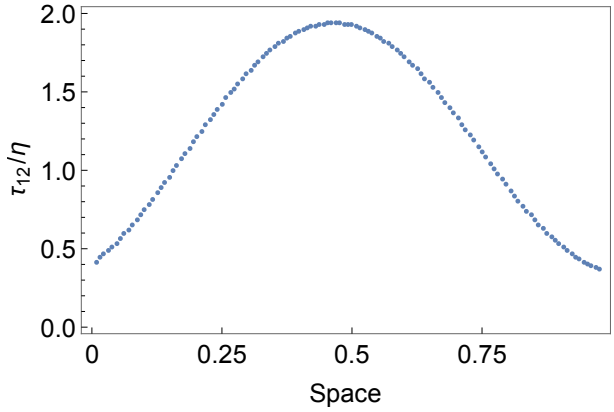

(d) Apparent stress over space.

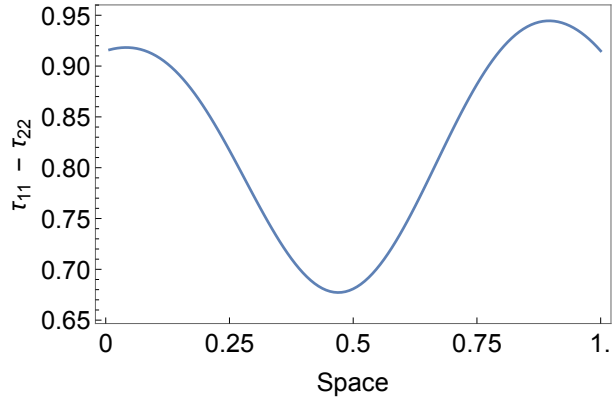

(e) First normal stress over space.

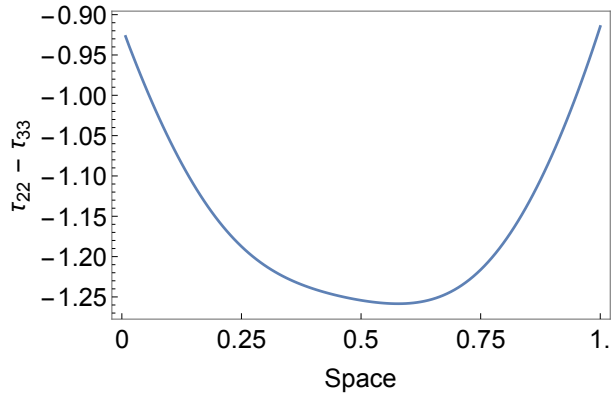

(f) Second normal stress over space.

Figure 34: Wiggle Flow: Rheological Properties for $N = 6$ and $\zeta_a = 2$.

CHAPTER 4

NEUMANN BOUNDARY CONDITION SIMULATIONS

Homogenous Neumann boundary conditions are employed in the Kinetic Model ensuring $\frac{\partial f}{\partial y} = 0$ along the channel boundaries. Boundary conditions imposed on the velocity vector along the channel walls remain as no-slip boundary conditions. Polymers are set in the parallel anchoring position along the channel walls at initial time, but are unrestricted thereafter. We impose sinusoidal perturbations on the y-component of the polarity vector and the $(1, 2)$ component of the second moment tensor. Neumann boundary conditions are visually verified in the flatten edges of the polarity angle over space plots.

4.1 SIMULATIONS WITH PUSHER-LIKE BEHAVIOR

Simulations with Neumann boundary conditions coupled with negative activation parameters produce two types of steady states: nematic state and reverse flow, as shown in Figure 35's phase diagram. Specific parameters of these states are in Table 8. Reverse flow simulations are shown with a constant nematic strength to show how the geometries and the physical characteristics of the simulation change when the magnitude of the activation parameter is increased. Nematic state is observed for values of nematic strength above five and is characterized by polarity vectors oriented in the same direction, zero fluid velocity, and a large order parameter.

Geometry Name	Nematic Strength	Active Strength
Steady State Reverse Flows	$N < 5$	$-30 \leq \zeta_a \leq -5$
Nematic State	$N \geq 5$	$-30 \leq \zeta_a \leq -5$

Table 8: Description of Observed States.

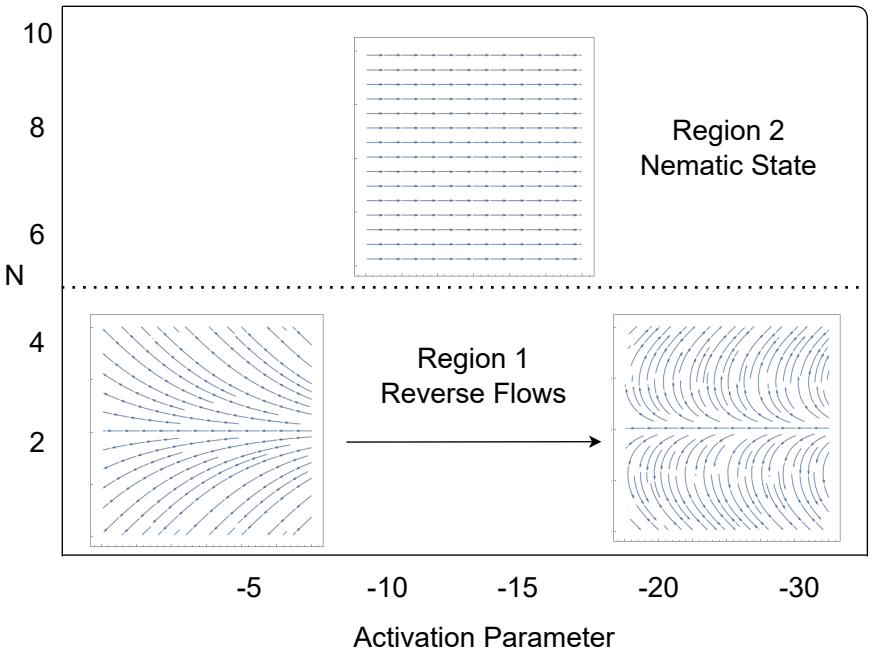

Figure 35: Phase Diagram for Neumann Boundary Conditions I.

4.1.1 STEADY STATE REVERSE FLOWS

Spontaneous flows with a negative activation parameter occur only when nematic strength is 4 or lower. We study this region over the range of $-40 < \zeta_a < -1$ and observe the effects of an increasing activation parameter on polarity vector orientation and fluid velocity magnitude. We hold nematic strength constant at $N = 4$, we observe the progression comparison with $\zeta_a = -5, \zeta_a = -15$, and $\zeta_a = -30$ for the polarity vector and nematic director. Figure 36 contains a progression of polarity vector diagrams for increasing ζ_a values. The centerline of the channel points to the left, and as the activation parameter increases, we see this centerline region form into a weak defect between the upper and lower regions of the channel. As the polarity vectors begin to orient away from the centerline, we see the polarity angle increase to the point where the orientation turns forward. The boundary angle is plotted against an increasing activation parameter in Figure 37, which shows an increase of boundary angle by 135° as the magnitude of the activation parameter is increased from $\zeta_a = -5$ to $\zeta_a = -30$.

Rheological data shows three sets of simulations with $\zeta_a = -5, -15, -30$. Polarity angles, measured in radians, of the three simulations plotted over space show the spatial profile of the angle increase in Figure 40(a). The steady state profile of order parameter in Figure 40(b) shows that increasing the magnitude of the activation parameter also increases orientational order. For all values of ζ_a, order parameter reaches its minimum in the center of the channel. Fluid velocity in Figure 40(c) over space exhibits parabolic shape, with peak velocity along the center line of the channel for all simulations. Velocity is negative, corresponding to the backward orientation of the polarity vectors over space. Velocity magnitude increases linearly as the activation parameter is increased as observed in Figure 39. Apparent stress in Figure 40(d) is skew-symmetric over space and increases as ζ_a increases in magnitude. First normal stress in Figure 40(e) measures negative for all values of ζ_a and sees a significant increase in magnitude as the activation parameter is increased. Second normal stress in Figure 40(f) is positive and increases in magnitude with an increasing ζ_a. Both normal stress differences, as ζ_a increases in magnitude, transition from a mostly constant value across the channel to an increased value of stress along the centerline.

4.1.2 NEMATIC STATE

Nematic state is observed for all values of ζ_a when $N > 5$, as seen in Figure 41 for polarity vector and nematic director plots. Nematic state is characterized by a constant orientation of the polarity vector and nematic director throughout the entirety of the channel, as well as a consistently high value of order parameter. The magnitude of the polarity vector is constant. Fluid velocity is zero throughout the entire simulation. No spontaneous flows are observed in nematic states. Order parameter, given by the density plot of Figure 41(b) is constant and the value (0.76) indicates a high degree of orientational order of the polymers throughout the channel.

4.1.3 SUMMARY

Simulations with homogenous Neumann boundary conditions produce spontaneous flows when $N \leq 5$. Large values of nematic strength produce purely nematic states. Nematic states are characterized by a constant orientation angle, zero fluid velocity, high order pa-

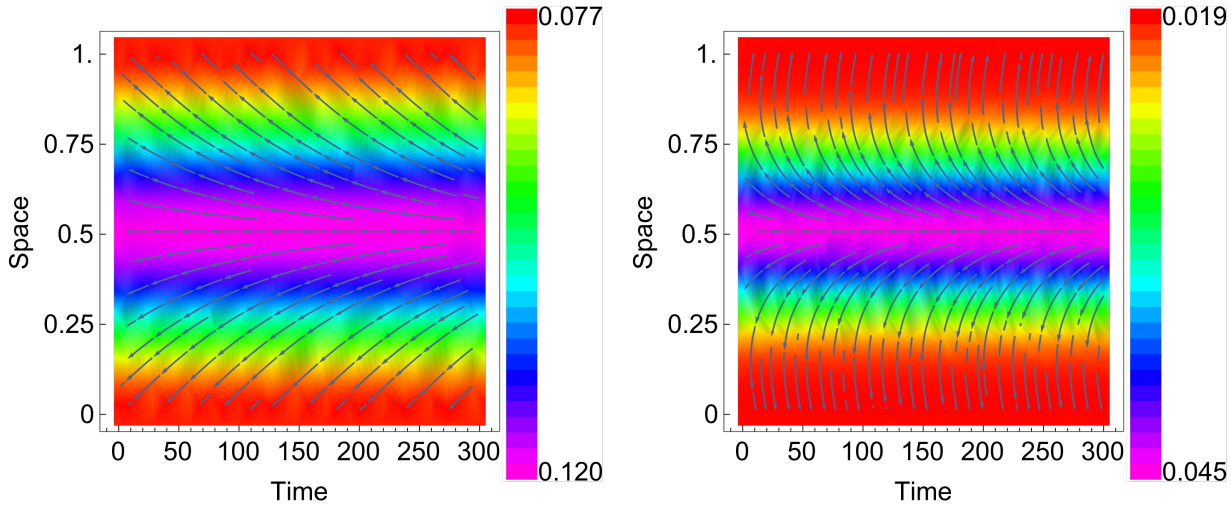

(a) $\zeta_a = -5$.

(b) $\zeta_a = -15$.

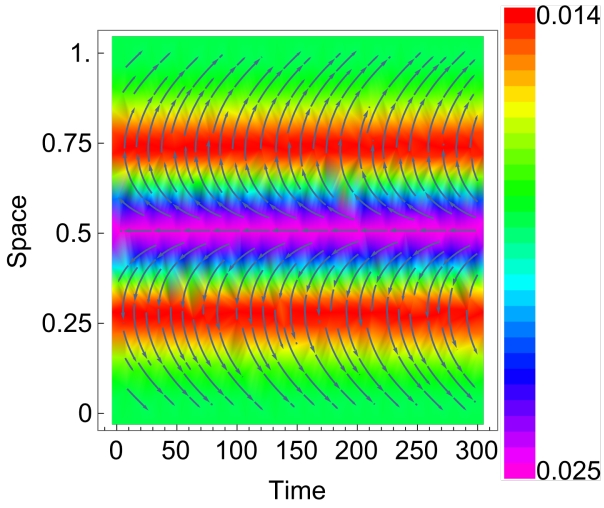

(c) $\zeta_a = -30$.

Figure 36: Reverse Flows: Polarity Vector Progression Plots for $N = 4$ and $\zeta_a = -5, -15, -30$.

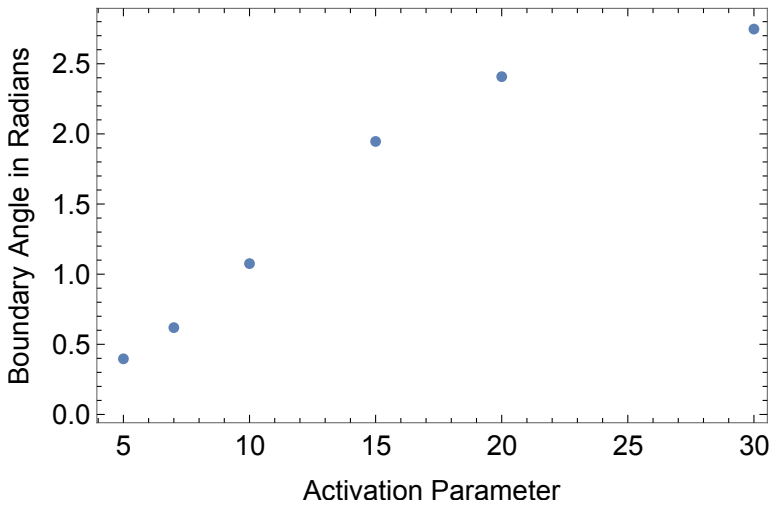

Figure 37: Reverse Flows ($\zeta_a < 0$): Boundary Angle vs. Positive Activation Parameter.

Geometry Name	Nematic Strength	Active Strength
Steady State Reverse Flows	$5 \leq N \leq 7$	$\zeta_a \leq 40$
Periodic State	$N = 8$	$\zeta_a = 20$
Nematic State	$7 < N \leq 12$	$\zeta_a < 20$
Steady State Banded Flow	$N = 12$	$\zeta_a = 30$
Isotropic State	$N \leq 5$	$5 \leq \zeta_a \leq 60$

Table 9: Description of Observed States.

rameter. A similar reverse flow geometry is observed for a constant value of N. Increasing $|\zeta_a|$ increases order parameter, magnitude of fluid velocity, and angle range. We observe that rightward-facing polarity vectors indicate a positive velocity and leftward-facing polarity vectors indicate a negative fluid velocity.

4.2 SIMULATIONS WITH PULLER-LIKE BEHAVIOR

Neumann boundary conditions coupled with a positive activation parameter produce nearly all type of possible observations: steady states, periodic states, nematic states, and isotropic states. Figure 42 shows the different type of geometries produced by varying values of nematic strength and activation parameter. When nematic strength is less than five,

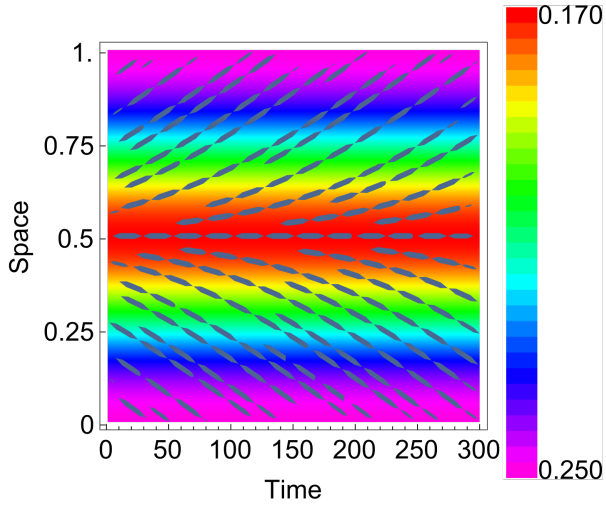

(a) $\zeta_a = -5$.

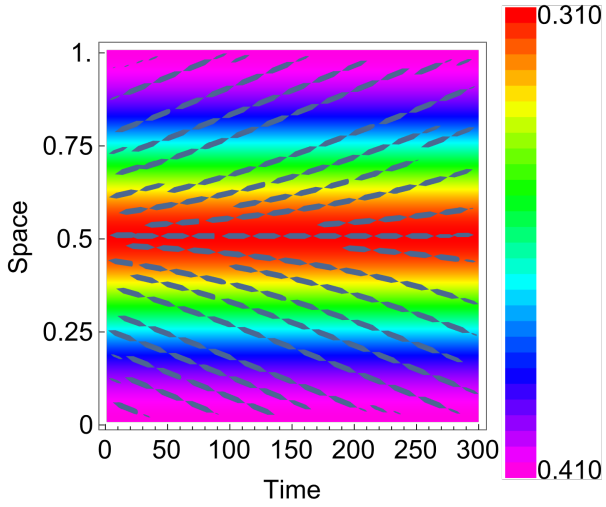

(b) $\zeta_a = -15$.

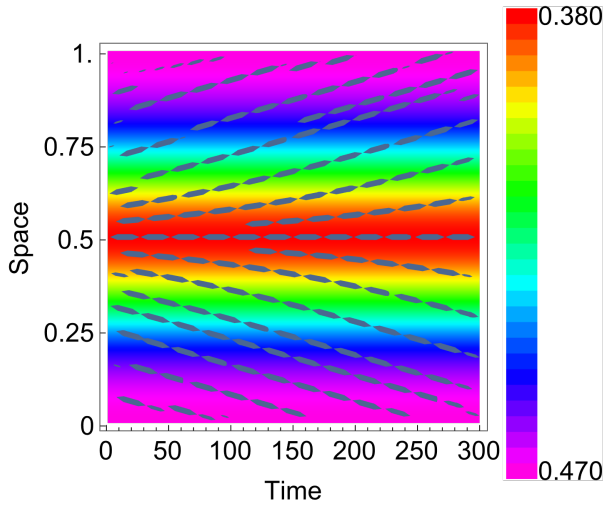

(c) $\zeta_a = -30$.

Figure 38: Reverse Flows: Nematic Director Progression Plots for $N = 4$ and $\zeta_a = -5, -15, -30$.

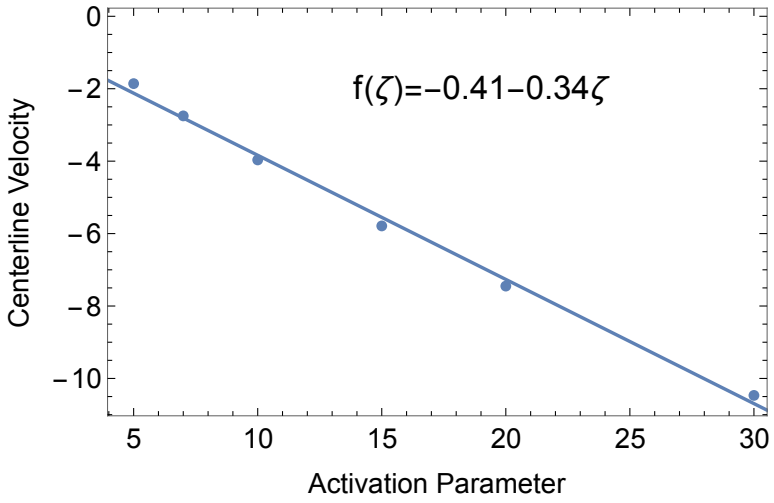

Figure 39: Reverse Flows ($\zeta_a < 0$): Fluid Velocity vs. Positive Activation Parameter.

isotropic state is observed. For a slightly larger value of N, we see spontaneous reverse flow. We present the reverse flows as one region, holding nematic strength constant to show how the geometries and physical values change with an increasing activation parameter. Periodic state is seen for intermediate value of nematic strength, as well as across the diagram when activation parameter is large. Large values of nematic strength produce interesting banded flows with three distinct regions, as well as a fairly large region containing less-interesting nematic states. These regions are defined in Table 9. The nematic and isotropic states observed here are not studied further.

4.2.1 STEADY STATE REVERSE FLOWS

Figures 43 and 44 contain three sets of steady state simulation data of constant N with increasing activation parameters of $\zeta_a = 5, 25, 40$. Increasing the magnitude of ζ_a increases the particle's pulling effects on surrounding polymers. We see similar structure within the polarity vector graphs, as the polarity angles on the boundary polymers increase with an increase of activation parameter. Figure 45 measures this shift at the boundaries; we see an increase of the boundary angle by approximately 80° as the activation parameter increases from $\zeta_a = 5$ to $\zeta_a = 40$. Analyzing the nematic director plots in Figure 44, the slope of

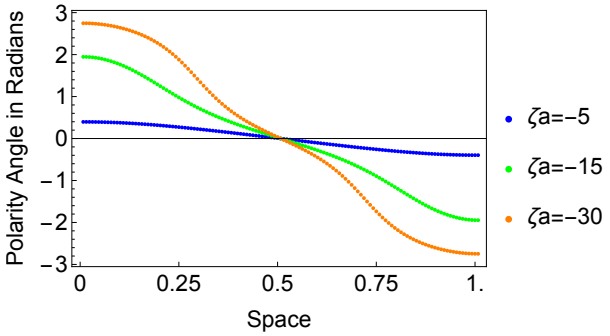

(a) Polarity angle over space.

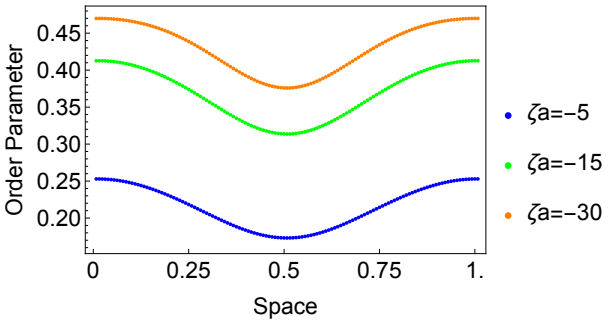

(b) Order parameter over space.

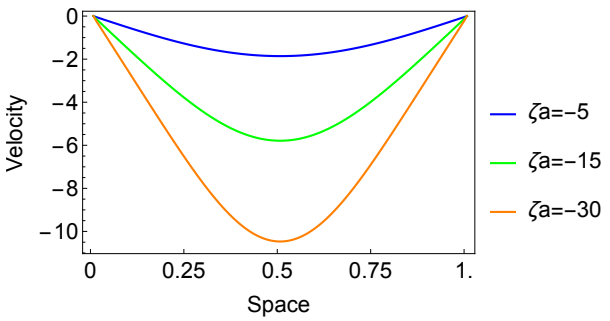

(c) Fluid velocity over space.

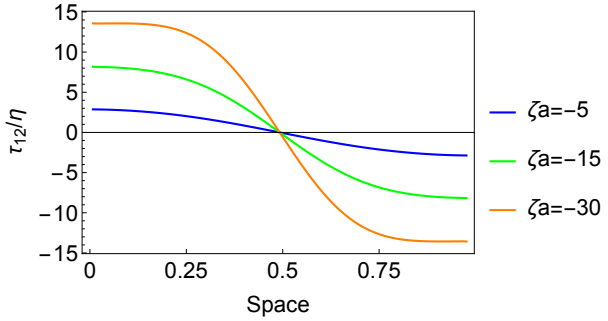

(d) Apparent stress over space.

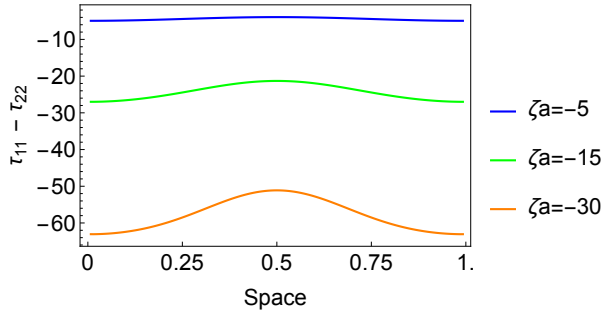

(e) First normal stress over space.

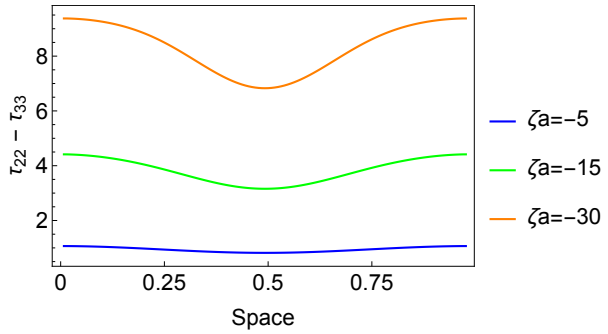

(f) Second normal stress over space.

Figure 40: Reverse Flows: Rheological Properties for $N = 4$ and $\zeta_a = -5, -15, -30$.

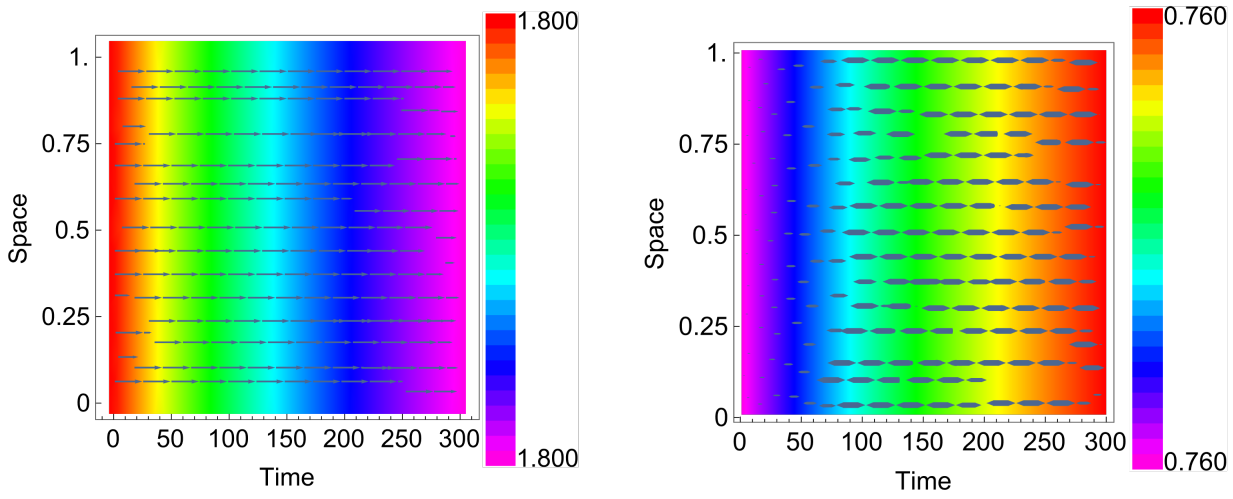

(a) Polarity vector at steady state.

(b) Nematic director at steady state.

Figure 41: Nematic State: Polarity and Nematic Plots.

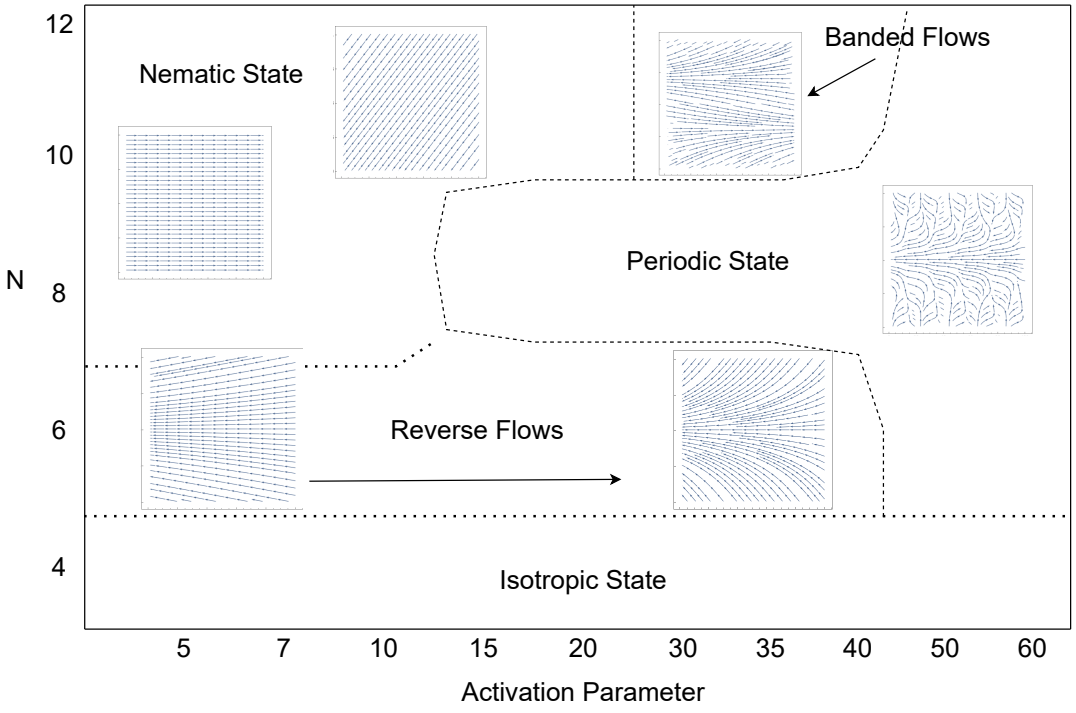

Figure 42: Phase Diagram for Neumann Boundary Conditions II.

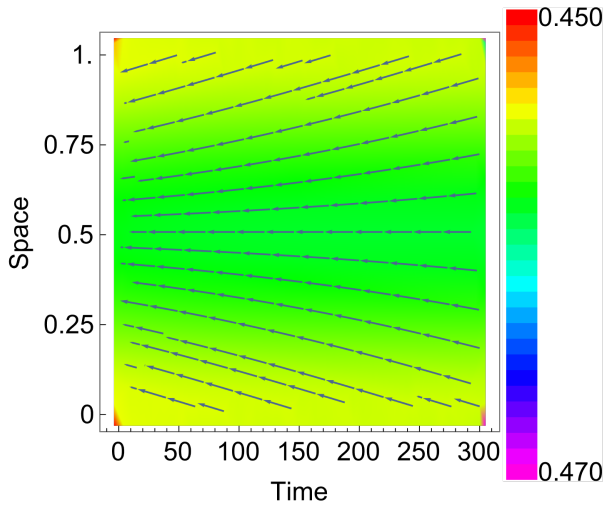

(a) $\zeta_a = 5$.

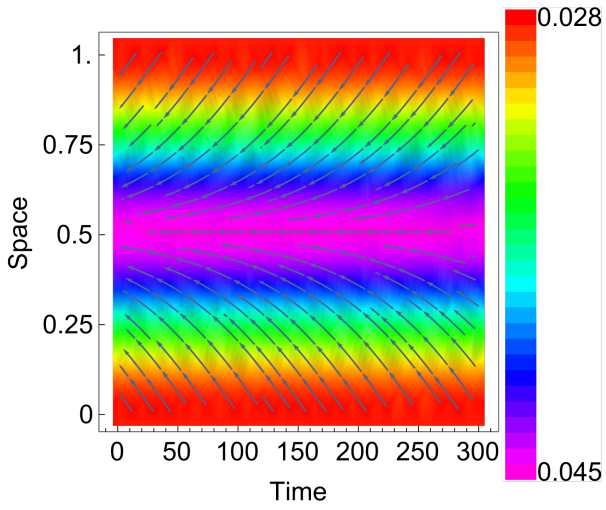

(b) $\zeta_a = 25$.

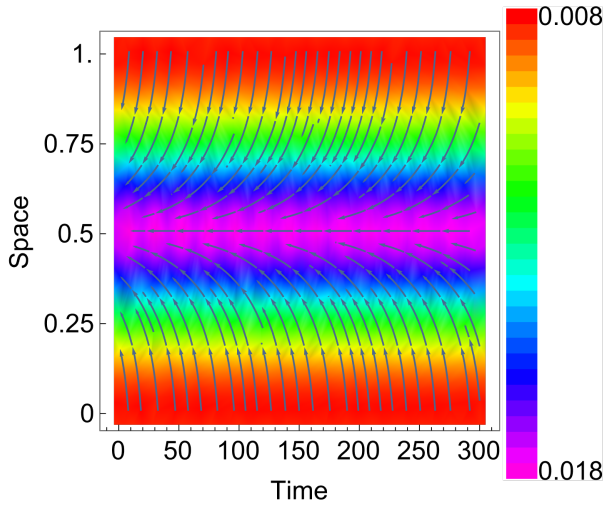

(c) $\zeta_a = 40$.

Figure 43: Reverse Flows: Polarity Vector Progression Plots for $N = 4$ and $\zeta_a = 5, 25, 40$.

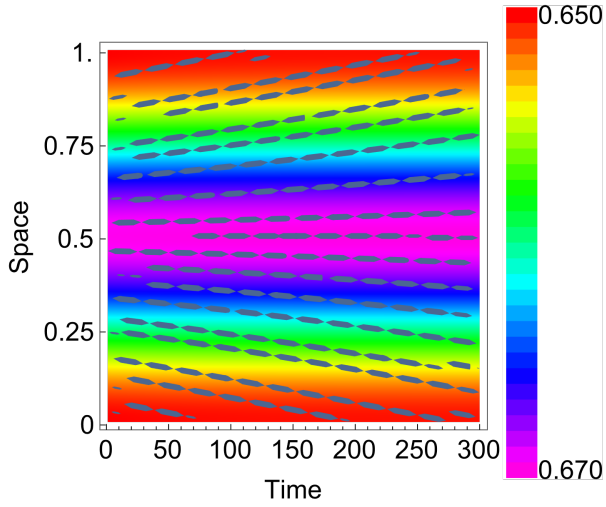

(a) $\zeta_a = 5$.

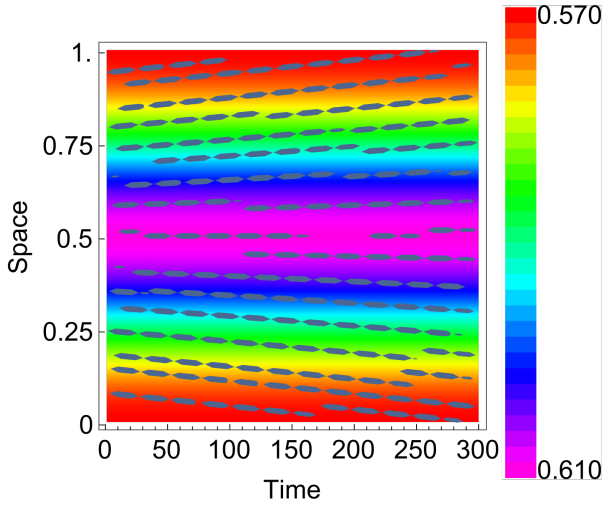

(b) $\zeta_a = 25$.

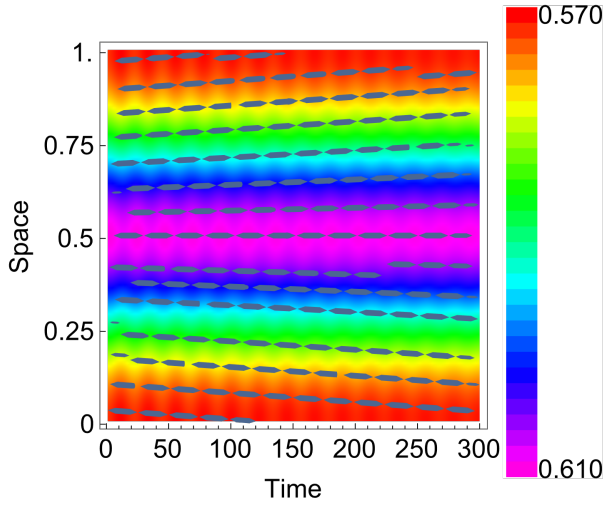

(c) $\zeta_a = 40$.

Figure 44: Reverse Flows: Nematic Director Progression Plots for $N = 4$ and $\zeta_a = 5, 25, 40$.

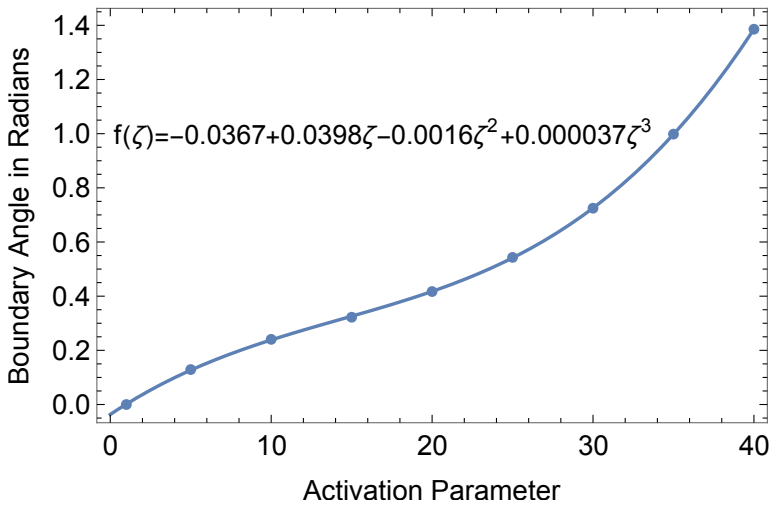

Figure 45: Reverse Flows ($\zeta_a > 0$): Boundary Angle vs. Negative Activation Parameter.

the nematic directors is lessened with an increased activation parameter. An effect that is reversed from the polarity diagrams, but also observed in Neumann boundary condition simulations containing negative activation parameters.

Steady state rheological data for $\zeta_a = 5, 25, 40$ is found in Figure 46. The range of polarity angles over space is broadened with an increased activation parameter, as seen in Figure 46a. Order parameter in Figure 46(b) sees little change (± 0.1) with varying values of ζ_a. Fluid velocity in Figure 46(c) peaks along the center line of the channel, resulting in a parabolic shape. The magnitudes of apparent stress in Figure 46(d), first normal stress in Figure 46(e), and second normal stress in Figure 46(f) all see increases in magnitudes and range with a stronger activation parameter. Any further increases in activation parameter create periodic solutions.

4.2.2 PERIODIC STATE

Neumann boundary conditions with puller-like behavior produce a large area of periodic solutions, as observed in the phase diagram in Figure 42. In this section, we study the simulation with parameters $N = 8$ and $\zeta_a = 20$. We observe a polarity diagram of mostly reverse-oriented polarity vectors, but with a periodic pulse which affects both polymer orien-

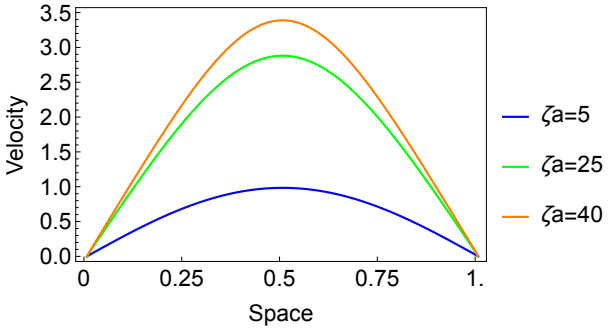

(a) Polarity angle over space.

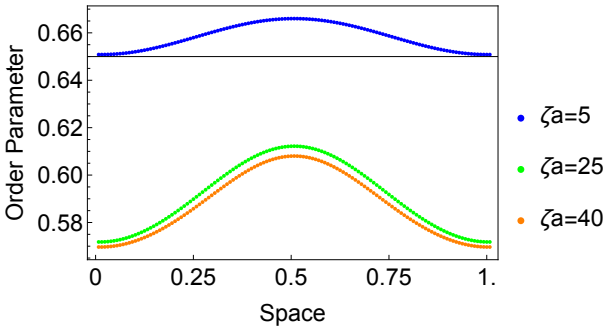

(b) Order parameter over space.

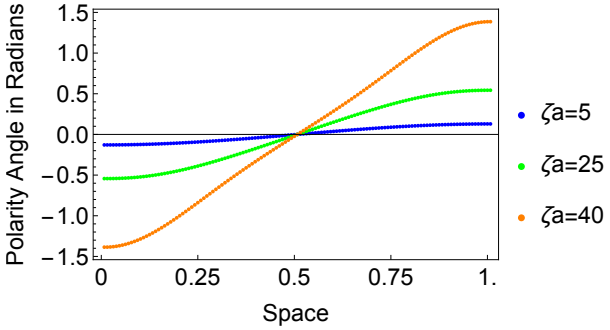

(c) Fluid velocity over space.

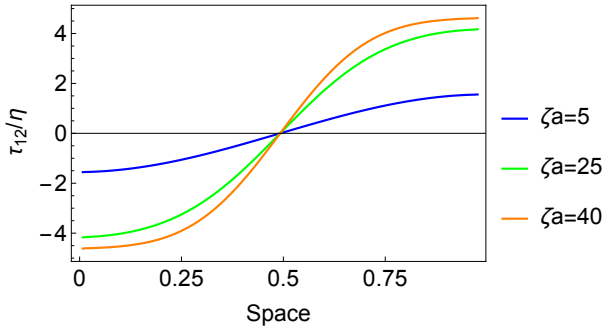

(d) Apparent stress over space.

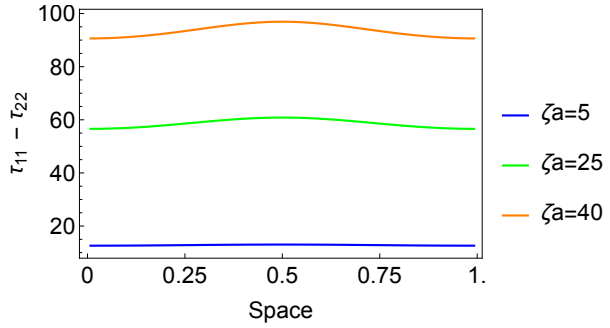

(e) First normal stress over space.

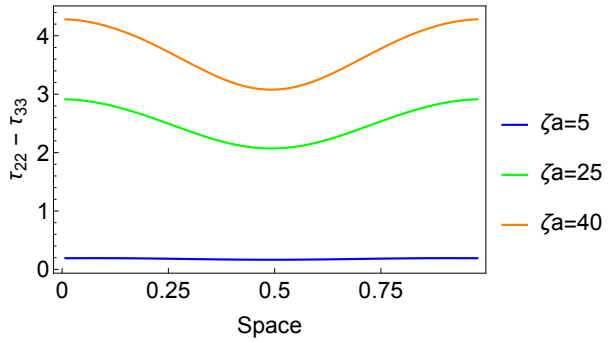

(f) Second normal stress over space.

Figure 46: Reverse Flows: Rheological Properties for $N = 4$ and $\zeta_a = 5, 25, 40$.

tation and magnitude in Figure 47(a). The nematic director in Figure 47(b) shows pulsating values for order parameter, while the nematic director orientation closely relates to that of reverse flows from Figure 44. We measure a short wave period of approximately 20 time units, as compared periodic state solutions with Dirichlet boundary conditions: Periodic State Type I and II show wave period lengths of 160 and 30, respectively.

In Figure 48, we see that all measured quantities fluctuate over the course of one period. The polarity angle in Figure 48(a) effectively retains reverse flow geometry, and we see the angle's magnitude fluctuate. Order parameter in Figure 48(b) maintains a parabolic shape over the course of one cycle, with the point of highest order measuring in the center of the channel. Values are measured roughly between 0.5 and 0.75 over the course of one cycle. We see velocity in Figure 48(c) double in magnitude over the course of one cycle while maintaining parabolic shape. Apparent stress in Figure 48(d) plots are skew-symmetric with respect to the center of the channel. First normal stress in Figure 48(e) mimics the graph of order parameter, displaying parabolic shapes with positive values. Second normal stress in Figure 48(f) measure negative, with a parabolic down shape with much lower measured magnitudes of stress than observed in the first normal graph.

4.2.3 STEADY STATE BANDED FLOW

Banded flow simulations occur when a high value of nematic strength is coupled with an intermediate activation parameter. We see three distinct banded regions in the polarity vector diagram which correspond to three matching regions in the nematic director diagram of Figure 49. Both show two weak defects surrounding the center band, characterized by horizontal vectors. In the polarity angle diagram over space in Figure 50(a), we see the center band characterized by a negative polarity angle. Order parameter in Figure 50(b) presents as a wave-like shape, showing the highest states of order correlating to the highest magnitudes of velocity. Fluid velocity data in Figure 50(c) is skew-symmetric over the channel, with the leftward-pointing upper channel in Figure 49(a) having negative velocity and the rightward-pointing lower channel having positive velocity, both of similar magnitudes. Apparent stress in Figure 50(d) presents itself as a downward parabola, with the center of the channel having the minimum value of stress. First and second normal stress graphs in Figure 50(e) and (f)

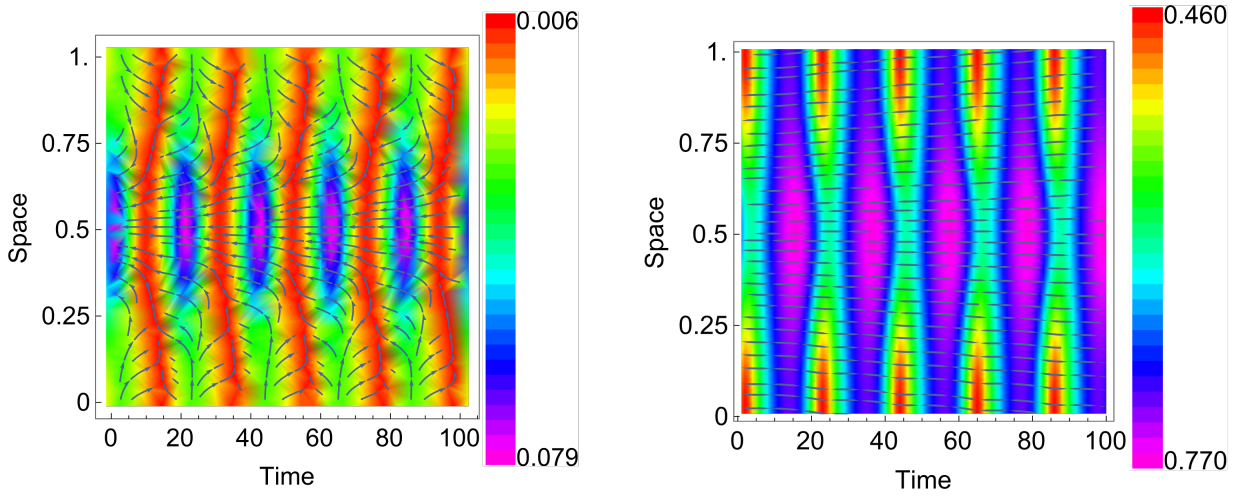

(a) Polarity vector at steady state.

(b) Nematic director at steady state.

Figure 47: Periodic State: Polarity and Nematic Plots for $N = 8$ and $\zeta_a = 20$.

both show two wave-like shapes across the channel, with the two defects showing the highest points of first normal stress corresponding to the two minimums of second normal stress diagram.

4.2.4 SUMMARY

Simulations with Neumann boundary conditions coupled with a positive activation parameter produce spontaneous flows when $N > 5$, in contrast to the previous section (simulations with a negative activation parameter), where above the threshold of $N = 5$ produce purely nematic states. Both steady state and periodic states are observed. In further contrast to the previous section, rightward-facing polarity vectors indicate a negative velocity, while leftward-facing polarity vectors indicate a positive fluid velocity.

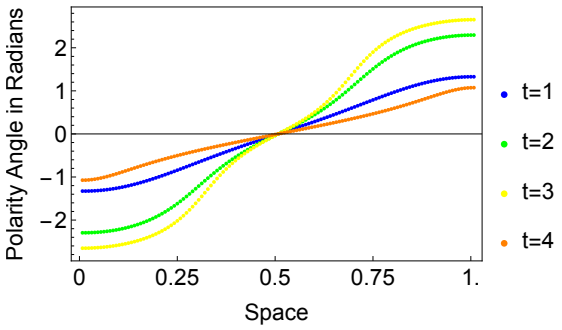

(a) Polarity angle over space.

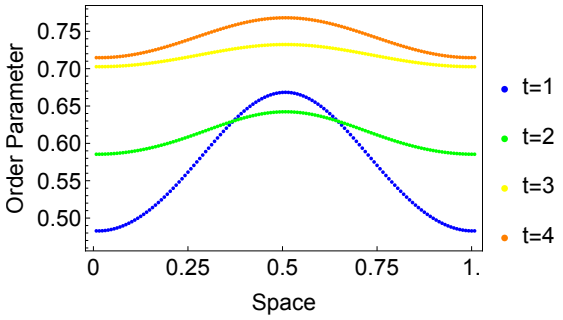

(b) Order parameter over space.

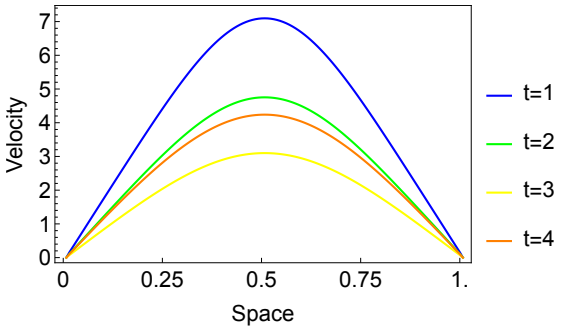

(c) Fluid velocity over space.

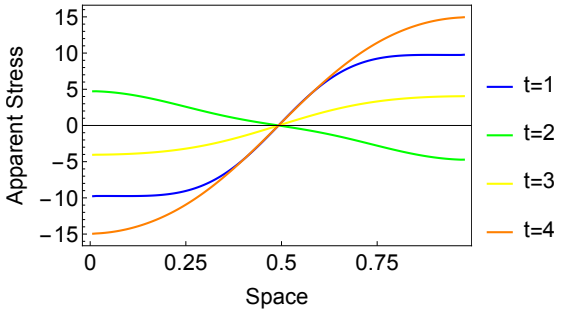

(d) Apparent stress over space.

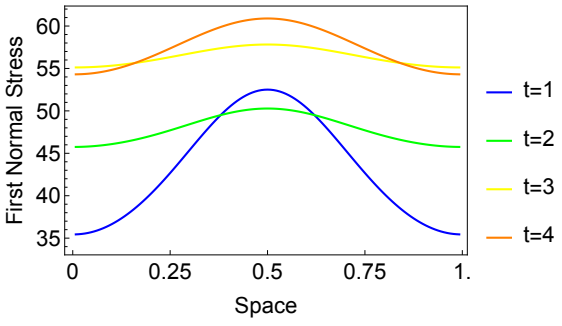

(e) First normal stress over space.

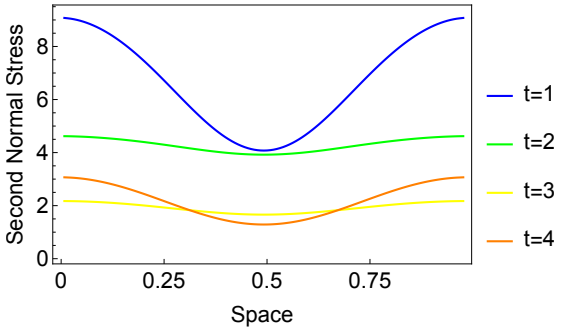

(f) Second normal stress over space.

Figure 48: Periodic State: Rheological Properties for $N = 8$ and $\zeta_a = 20$.

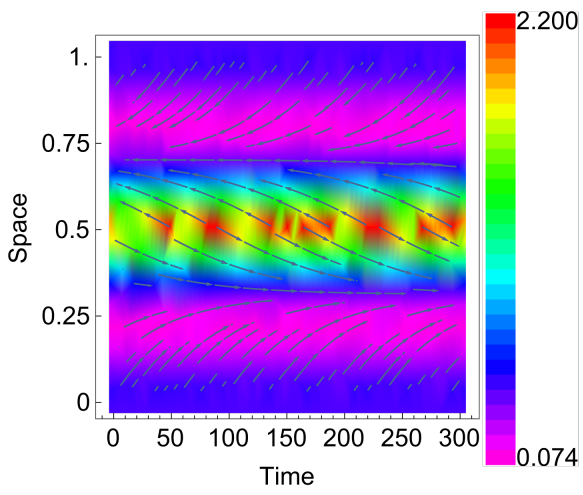

(a) Polarity vector at steady state.

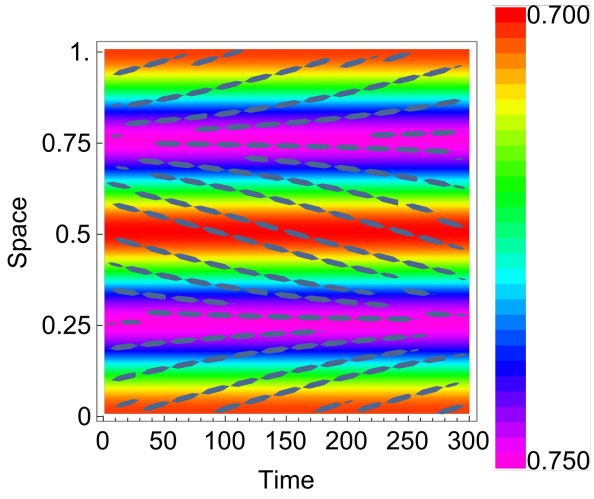

(b) Nematic director at steady state.

Figure 49: Banded Flow: Polarity and Nematic Plots for $N = 12$ and $\zeta_a = 30$.

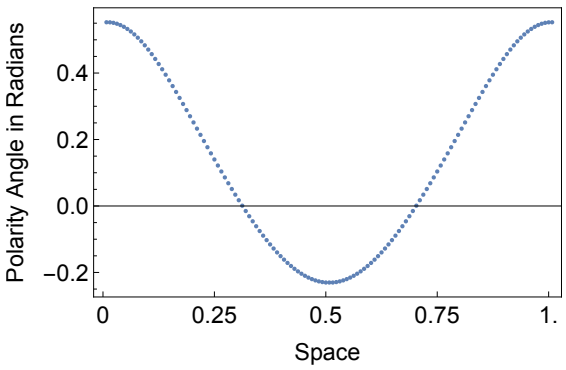

(a) Polarity angle over space.

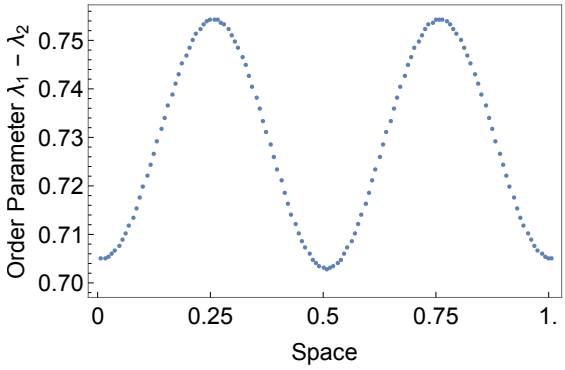

(b) Order parameter over space.

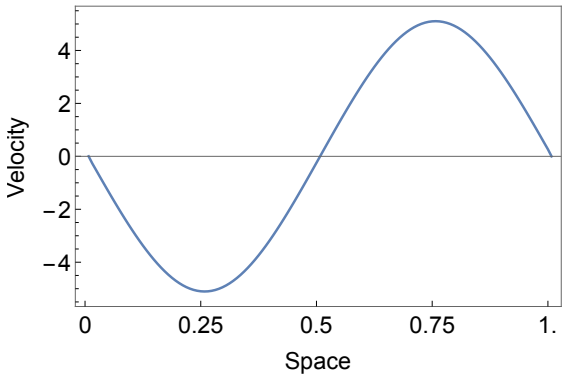

(c) Fluid velocity over space.

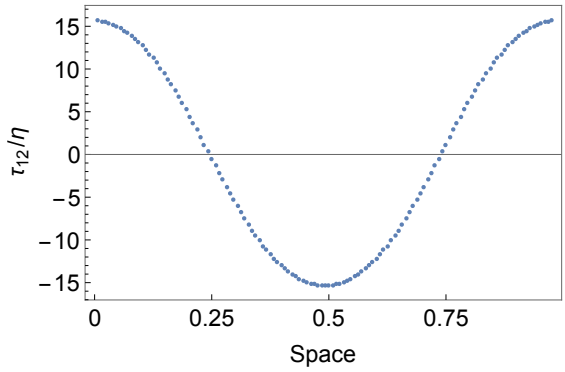

(d) Apparent stress over space.

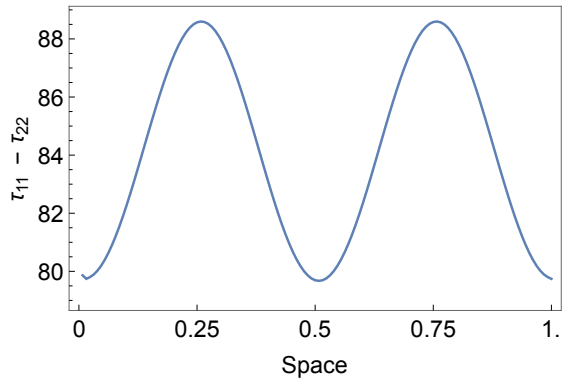

(e) First normal stress over space.

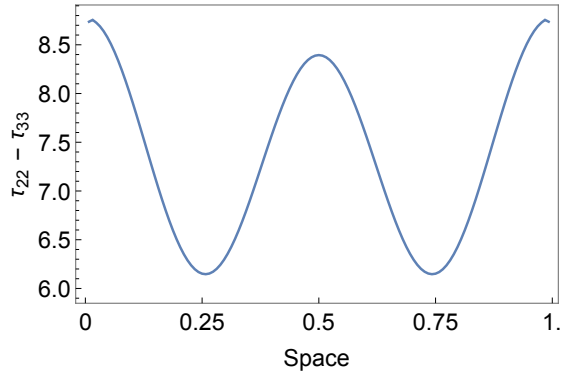

(f) Second normal stress over space.

Figure 50: Banded Flow: Rheological Properties for $N = 12$ and $\zeta_a = 30$.

CHAPTER 5

POISEUILLE FLOW SIMULATIONS

In Chapter 1, we reduce the equations of the Kinetic Model to one dimension. The pressure gradient term is a component of the Navier-Stokes velocity equation (19), and the expansion of the pressure gradient occurs in (22). We require only the first components of the spatial terms, thus $\frac{\partial p}{\partial x} = 0$ in the reduced model. In this chapter we assume $\frac{\partial p}{\partial x} \neq 0$, and with this term, we induce a pressure gradient along the length of the channel. We refer to this term as p_x. A horizontal pressure gradient applied to an incompressible fluid along a one-dimensional channel is known as Poiseuille flow [11], shown in Figure 51. The addition of a pressure gradient can cause a flow reversal to the direction of applied pressure, known as "backflow" [4].

For most simulations, pressure gradients are applied in both positive and negative directions. We define these directions with respect to the direction of the anchored polarity vector. In simulations of Dirichlet boundary conditions with parallel anchoring, the polarity vector is anchored to the channel walls with the vector head pointing to the right. Neumann boundary condition simulations begin with the polarity vector oriented rightward. We define a positive pressure gradient as a rightward-directional force in the channel. In contrast, a negative pressure gradient imposes a leftward force in the channel. Within normal anchoring simulations, where the polarity vector is anchored vertically, only one direction of pressure is applied.

On each defined region in Chapters 2 and 3, we perform Poiseuille flow simulations with pressure gradients of ± 1, ± 5, and ± 10. These values of pressure gradients were chosen to match the Poiseuille flow simulations performed in reference [39]. In specific simulations where there is an interesting event happening at a different value of p_x, we show the data presented there. All simulation results are compared with non-Poiseuille flow, or $p_x = 0$. Simulations are affected differently by the addition of a pressure gradient, therefore, some sections will show the data represented in differently than others.

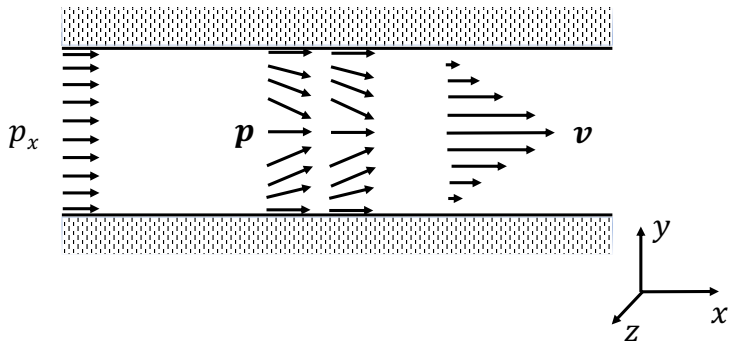

Figure 51: Axisymmetric Poiseuille flow generated by a horizontal pressure gradient, p_x.

5.1 DIRICHLET BOUNDARY CONDITIONS WITH PARALLEL ANCHORING AND PUSHER-LIKE BEHAVIOR

In Chapter 2, we saw the effects of perturbations with different wave numbers applied to otherwise identical channel flow simulations. They were separated into four regions and by perturbation type. Strong geometric similarities are seen between regions where the nematic strength and the activation parameter are the same, but the initial perturbation applied is different. In contrast to the organization in Chapter 2, the following section will present Region 1.a and Region 1.b together, as the application of positive and negative pressure gradients are similar in effect to changing the wave number of the perturbation.

5.1.1 REGION 1: FORWARD AND REVERSE CHANNEL FLOWS

Region 1.a: Forward Channel

With the addition of a positive pressure gradient, the steady state geometry of Forward Channel flow, as viewed in Figure 5, remains generally unchanged, as seen in the polarity angle over space plot of Figure 52(a). As the gradients of the angles become slightly sharper, the overall shape remains the same, displaying skew-symmetry about the center of the channel. In Figure 52(b), the velocity profile remains the same shape, while the overall velocity magnitude is doubled.

When any amount of negative pressure is applied, we see an immediate change of flow

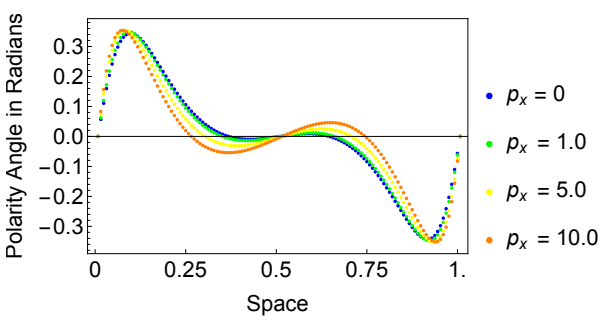

(a) Polarity angles over space.

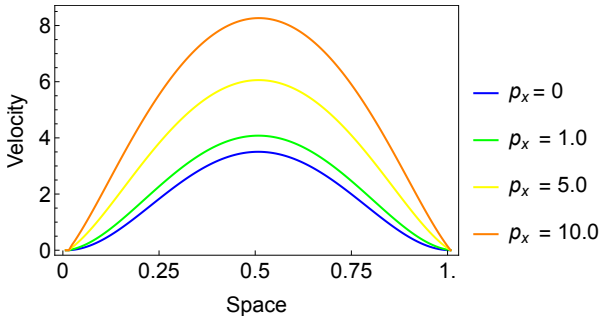

(b) Fluid velocities over space.

Figure 52: Region 1.a: Positive Pressure Gradient.

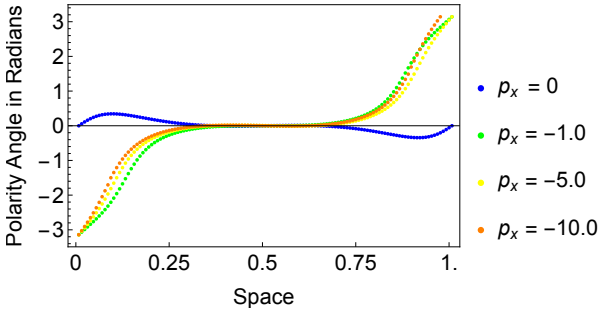

(a) Polarity angles over space.

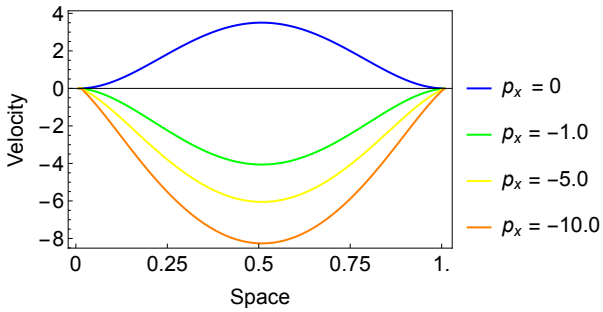

(b) Fluid velocities over space.

Figure 53: Region 1.a: Negative Pressure Gradient.

direction and velocity direction, as viewed in Figure 53. Remarkably, the angle of the polarity vector in the negative direction mirrors that of the simulation when positive flow is viewed. When the pressure gradient is increased in magnitude, the steady state geometry maintains its shape, while velocity is increased in magnitude. When applying the pressure gradient values of $p_x = 10$ and $p_x = -10$, the maximum velocity magnitudes measured for each are nearly equivalent as seen in Figures 52(b) and 53(b).

Region 1.b: Reverse Channel

Region 1.b's Reverse Channel flow contains the same parameters as the simulation as above, but with a $\sin 2\pi$ initial perturbation that orients the polarity vector in the opposite

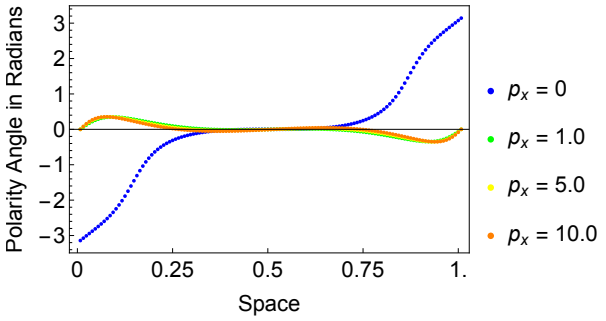

(a) Polarity angles over space.

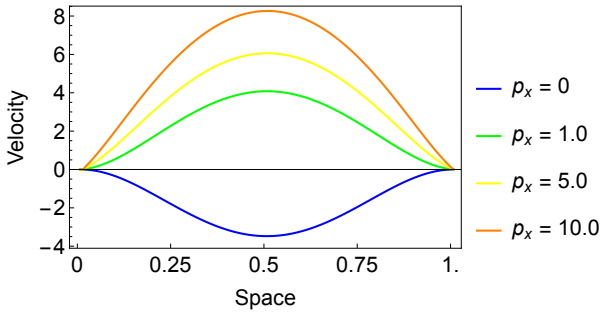

(b) Fluid velocities over space.

Figure 54: Region 1.b: Positive Pressure Gradient.

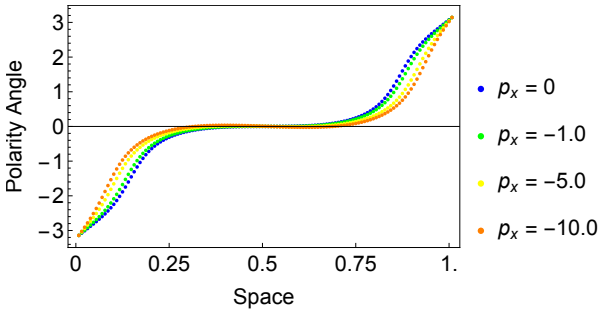

(a) Polarity angles over space.

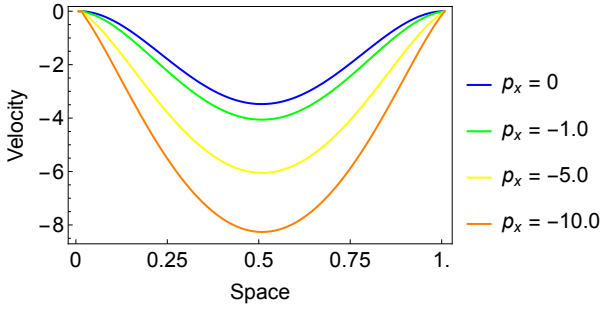

(b) Fluid velocities over space.

Figure 55: Region 1.b: Negative Pressure Gradient.

direction (recall Figure 14). We apply a positive pressure gradient and observe an immediate reversal of flow, both in polarity vector orientation and velocity direction, as seen in Figure 54. The induced-flow geometry now mimics Region 1.a.'s Forward Channel flow in Figure 5. The effect of a negative pressure gradient on leftward-oriented polarity vectors preserve the geometric shape while increasing velocity by nearly three-fold.

5.1.2 REGION 2: DOUBLE CHANNEL FLOWS

Region 2.a: Forward Double Channel

When a positive pressure gradient is applied to a rightward-facing polarity diagram, referencing Figure 7, the steady state structure is unchanged, as seen in Figure 56. The

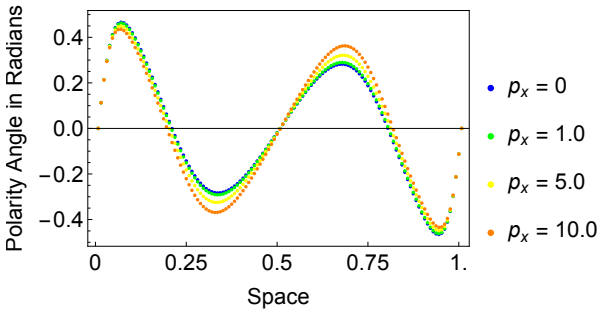

(a) Polarity angles over space.

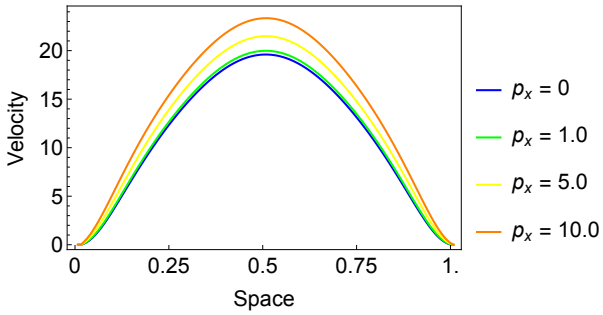

(b) Fluid velocities over space.

Figure 56: Region 2.a: Positive Pressure Gradient.

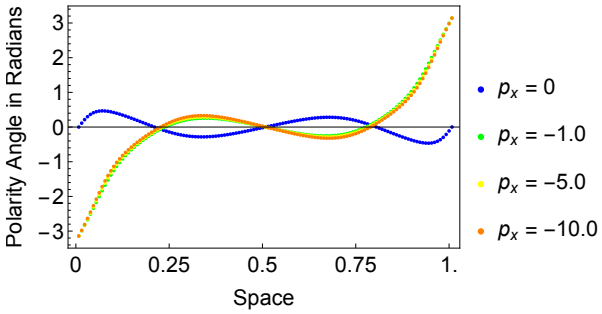

(a) Polarity angles over space.

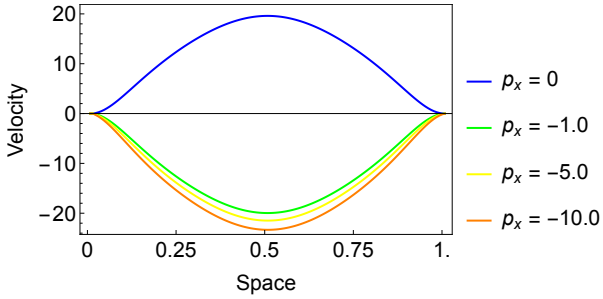

(b) Fluid velocities over space.

Figure 57: Region 2.a: Negative Pressure Gradient.

Forward Double Channel geometry remains in tact. Given the high velocity observed with a pressure gradient, as seen in Figure 8, applying higher magnitudes of pressure does not significantly raise the velocity.

When a negative pressure gradient is applied, shown in Figure 57, the original rightward-pointing polarity vectors see an immediate shift to the leftward direction, displaying a remarkable similarity to Region 2.b's Reverse Double Channel geometry when perturbed by $\sin 2\pi$, as seen in Figure 16.

Region 2.b: Reverse Double Channel

The same effect seen in the previous section (Region 1.b) of applying a positive pressure gradient to a leftward-pointing polarity vector diagram occurs again as a flow reversal

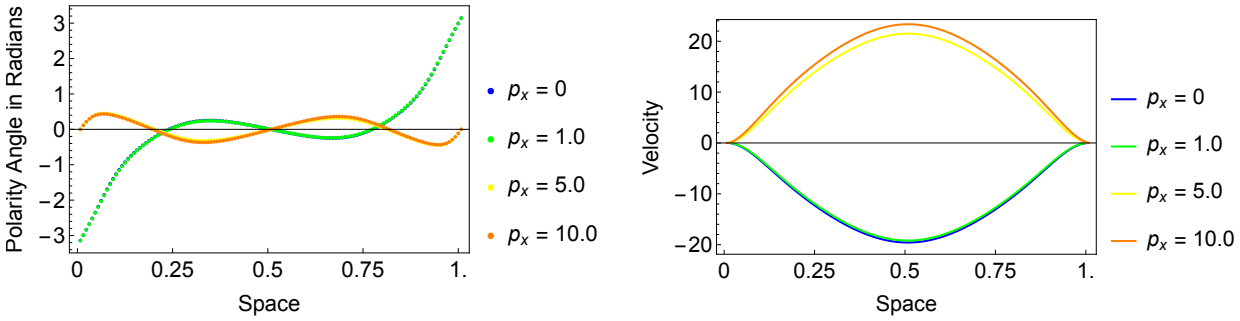

(a) Polarity angles over space.

(b) Fluid velocities over space.

Figure 58: Region 2.b: Positive Pressure Gradient.

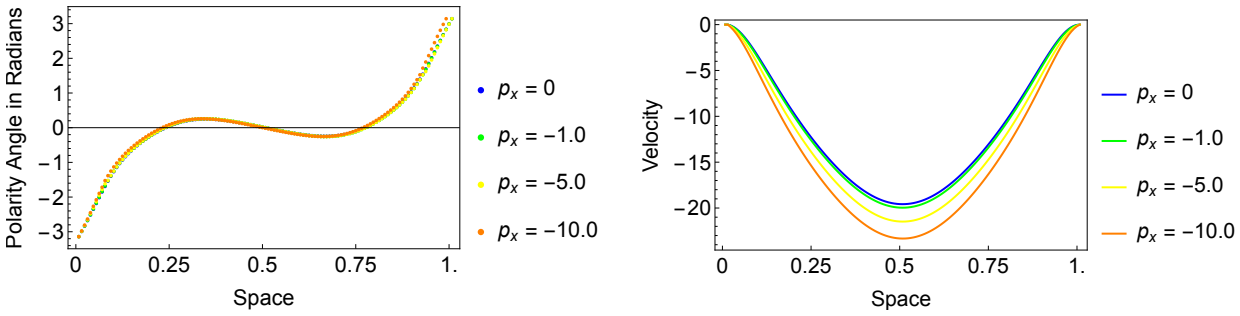

(a) Polarity angles over space.

(b) Fluid velocities over space.

Figure 59: Region 2.b: Negative Pressure Gradient.

is induced. However, the flow reversal to the rightward direction does not happen immediately, but at a critical point between $2.8 < p_{x_c} < 2.9$. When the flow is reversed, near perfect symmetry is seen in the polarity angle diagram in Figure 58 with regards to channel boundaries, width, and shape. A negative pressure gradient applied to the Reverse Double Channel simulation preserves channel geometry while slightly increasing velocity, as seen in Figure 59.

5.1.3 REGION 3: SIMPLE FORWARD AND REVERSE FLOWS

Simple Forward and Simple Reverse flows with pressure gradients follow the same general rules of Region 1 and Region 2: forward flows with positive pressure gradients remain

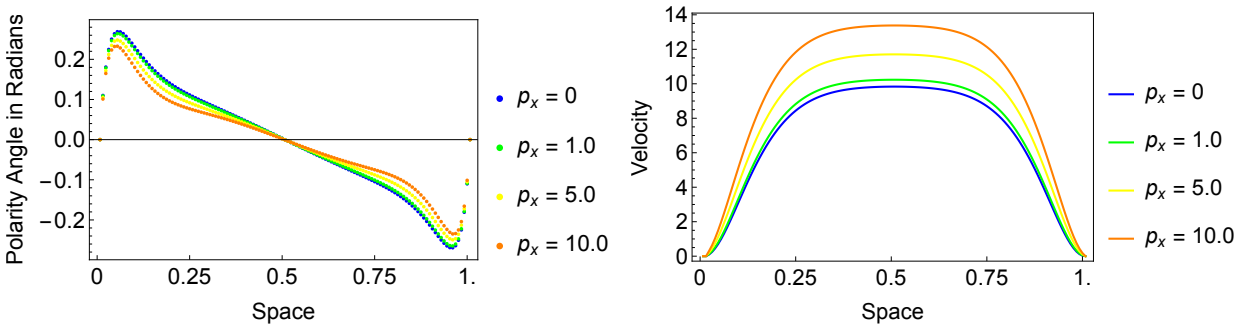

(a) Polarity angles over space. (b) Fluid velocities over space.

Figure 60: Region 3.a: Positive Pressure Gradient.

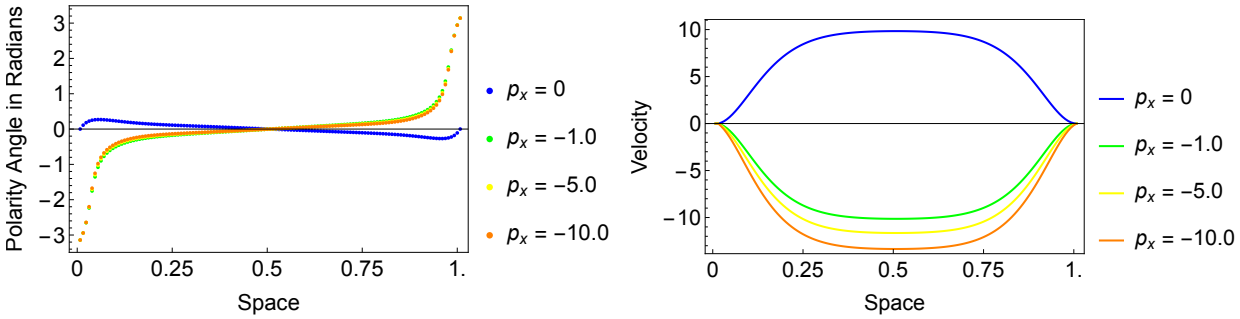

(a) Polarity angles over space. (b) Fluid velocities over space.

Figure 61: Region 3.a: Negative Pressure Gradient.

rightward-oriented with positive velocities that increase steadily as pressure increases, shown in Figure 60. Reverse flows with negative pressure gradients remain leftward-oriented with negative velocities that increase steadily in magnitude as pressure increases, as seen in Figure 63. When the opposite pressure is applied, both flows see their orientation immediately shift to the opposite direction with geometry preserved, as well as an increased velocity profiles with increased pressure, shown in Figures 61 and 62.

5.1.4 REGION 4: FORWARD CENTERLINE FLOW

As observed in Chapter 2, Region 4.a and Region 4.b produce nearly identical simulation results with different initial perturbations. The addition of pressure gradients also yield

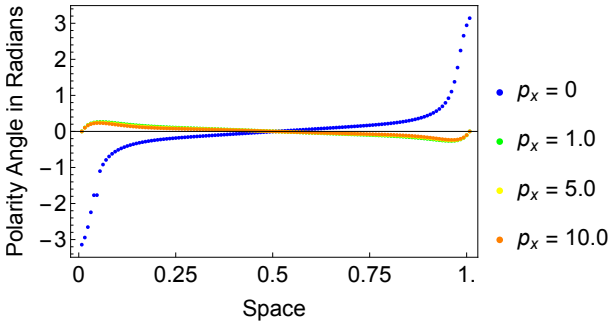

(a) Polarity angles over space.

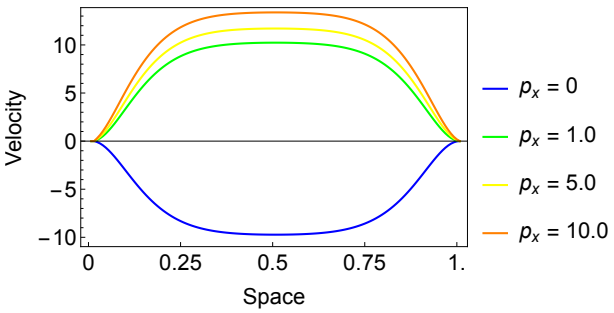

(b) Fluid velocities over space.

Figure 62: Region 3.b: Positive Pressure Gradient.

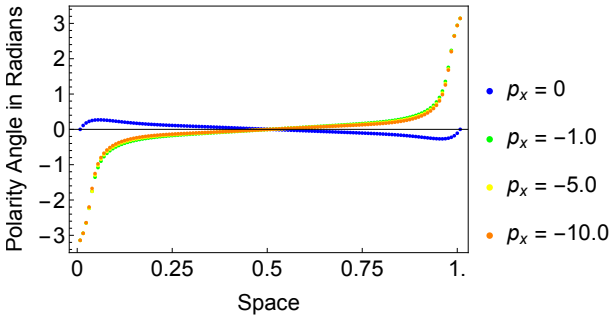

(a) Polarity angles over space.

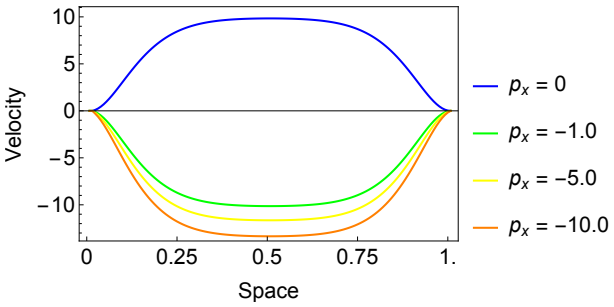

(b) Fluid velocities over space.

Figure 63: Region 3.b: Negative Pressure Gradient.

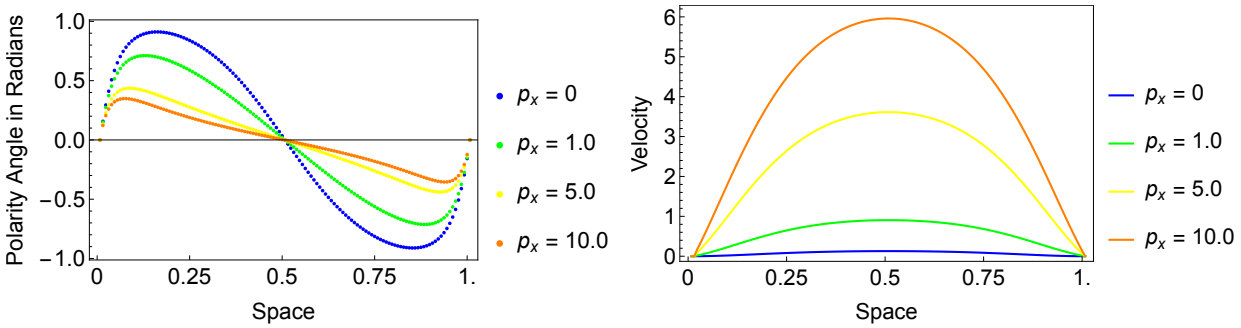

(a) Polarity angles over space.

(b) Fluid velocities over space.

Figure 64: Region 4: Positive Pressure Gradient.

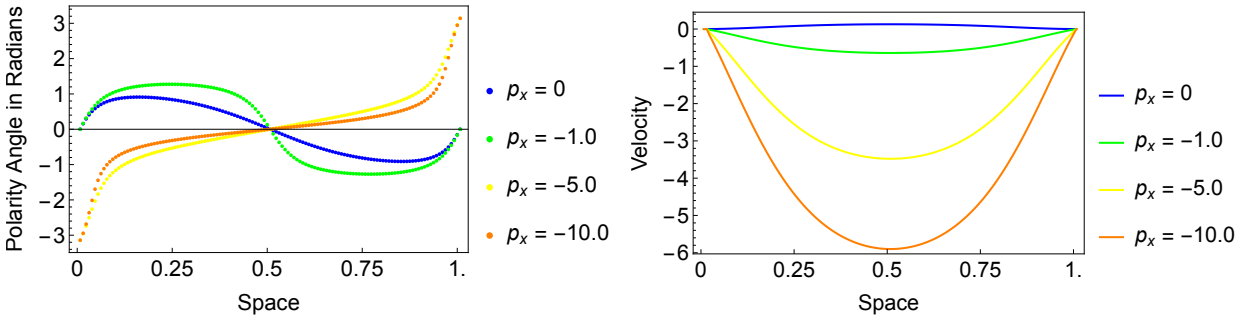

(a) Polarity angles over space.

(b) Fluid velocities over space.

Figure 65: Region 4: Negative Pressure Gradient.

identical results. Only the results from the $\sin \pi$ perturbation are presented here. Recall the simulation observed without pressure in Figure 12(c) displays a very small velocity. A positive pressure gradient significantly increases fluid velocity while descreasing the range of polarity angles at steady state. This dominating effect essentially "flattens" the observed curves of Figure 11. Applying a pressure gradient now aligns fluid velocity direction with polarity direction. The effects of negative pressure gradients are shown in Figure 65. We see a flow reversal with leftward-facing polarity vectors and negative velocity values.

Geometry	**Perturbation**	$p_x > 0$	$p_x < 0$
Forward Flows	$\sin \pi$	Geometry Preserved	Geometry Reversed
Reverse Flows	$\sin 2\pi$	Geometry Reversed	Geometry Preserved

Table 10: Geometric Effects of Pressure-Induced Simulations.

5.1.5 SUMMARY

Applying the array of different pressure gradients to these simulations produce only steady state solutions. Within Regions 1-3, the overall geometry is dictated by the specific coupling of nematic strength and activation parameter. As with different initial perturbations, the geometric structure is preserved with the application of pressure. When the pressure direction is in the initial flow direction, the direction and geometry is unchanged with respect to flow direction. If the pressure direction is opposite the flow direction, a near exact geometry in the opposite direction is observed. The flow reversal to the direction of the imposed pressure gradient is also seen in the microfluidic studies of reference [39]. Further, we see polarity vector orientation correlate to the sign of velocity and an increase in velocity magnitude with increasing values of p_x. We generalized these results in Table 10.

5.2 DIRICHLET BOUNDARY CONDITIONS WITH PARALLEL ANCHORING SIMULATIONS WITH PULLER-LIKE BEHAVIOR

5.2.1 STEADY STATE OUTWARD FLOW

The steady state geometry resembling an outward-oriented flow is seen in Figure 22. The structure has a rightward-pointing polarity vector in the center, separating two forward-angled regions. Thus, we classify this simulation as a forward flow. When a positive pressure gradient is applied to the simulation, we see the simulation geometry change very little, as shown in Figure 66.

We observe a steady state velocity of zero in the original simulation. The application of a positive pressure gradient produces a different velocity profile: from the channel boundaries,

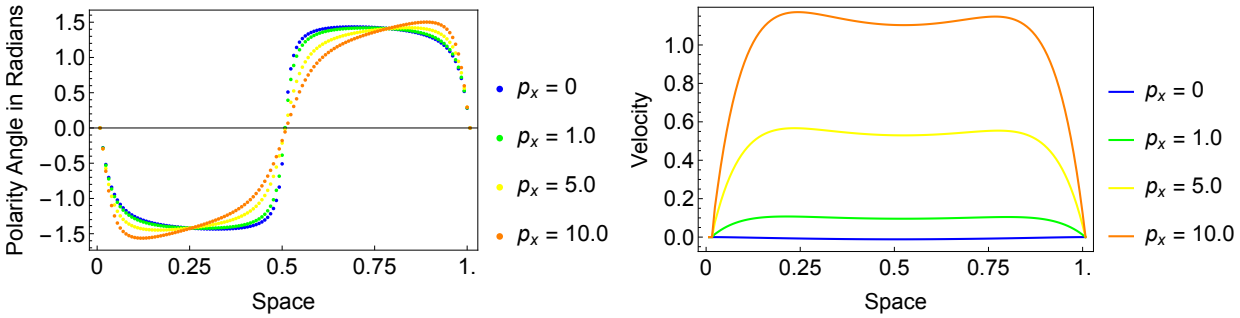

(a) Polarity angles over space. (b) Fluid velocities over space.

Figure 66: Outward Flow: Positive Pressure Gradient.

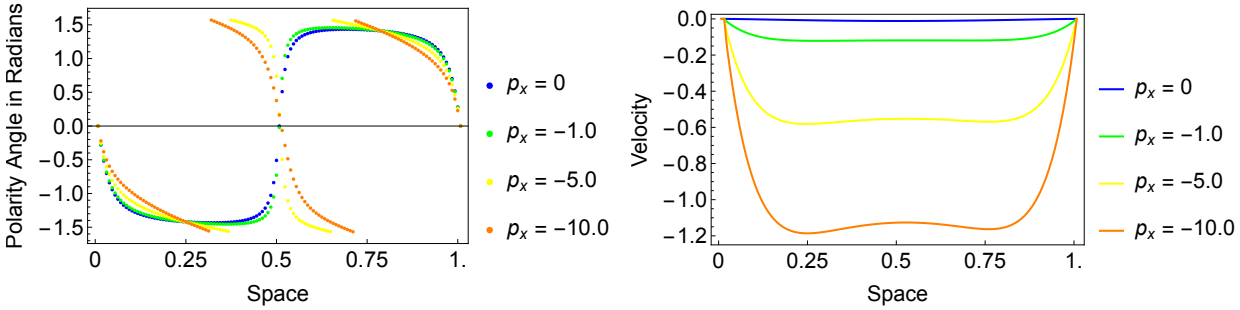

(a) Polarity angles over space. (b) Fluid velocities over space.

Figure 67: Outward Flow: Negative Pressure Gradient.

the velocity rises sharply and peaks on either side of the channel centerline. This contrasts to previous velocity profiles with peaks at the vertex. A negative pressure gradient produces an identical velocity profile in the negative direction. While velocity does increase from zero (observed when $p_x = 0$) it remains at a relatively low magnitude of approximately ± 0.8 for positive and negative pressure gradients.

A negative pressure gradient produces a flow reversal of the polarity vector and the sign of velocity, as seen in Figure 67. The outward orientation towards the channel boundaries is preserved, and as in the previous section, we see the overall geometric structure preserved but with a reversal of flow. The critical value of the negative pressure gradient that causes the inversion is between $-3.0 < p_{x_c} < -2.5$. As the simulation nears the centerline defect, we see a skew-symmetry "flip" of the two graphs as seen in Figure 67(a). We see velocities

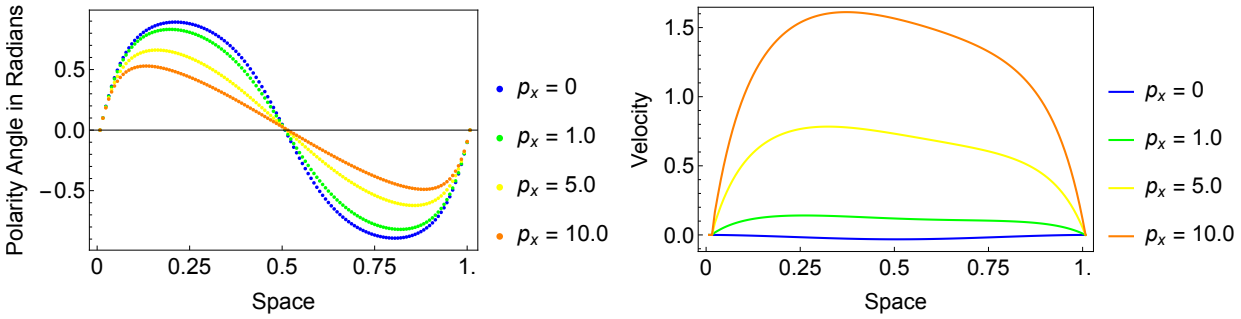

(a) Polarity angles over space.

(b) Fluid velocities over space.

Figure 68: Inward Flow: Positive Pressure Gradient.

values remain negative and increase in magnitude proportionally to the pressure gradient in Figure 67(b).

5.2.2 STEADY STATE INWARD FLOW

Inward flow's steady state geometry of the polarity vector is seen in Figure 24. Without an induced pressure gradient, the steady state velocity is recorded at zero. Inward flow has a rightward-pointing polarity vector plot, and the addition of a positive pressure gradient predictably raises velocity from zero. The polarity plot sees decreased curvature, as an increasing positive pressure gradient dominates the original steady state geometry, as shown in Figure 68.

The application of a negative pressure gradient follows a similar pattern as observed in the previous section of Outward flow, as a critical value of the pressure gradient inverts the center region of the polarity plot while the outer regions maintain orientation. The polarity angle diagram in Figure 69(a) shows the differences in the geometries of the channel center. The angle data in Figure 69(b) from $p_x = -4$ and $p_x = -5$ shows a sharp angle descent and near mirror image similarities along the center region. Increasing the negative pressure gradient to $p_x = 10$ produces a near reflective steady state geometry. Note that both top and bottom channel boundaries in both graphs maintain a rightward orientation, while the centerline flow exhibits a directional change.

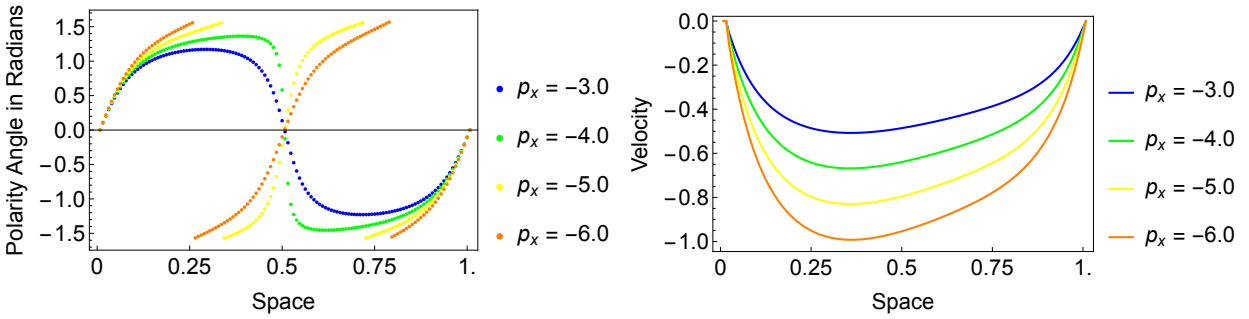

(a) Polarity angles over space.

(b) Fluid velocities over space.

Figure 69: Inward Flow: Negative Pressure Gradient.

5.2.3 PERIODIC STATE, TYPE I

The first of two periodic states observed within Dirichlet boundary conditions, Type I presents a longer wave period in measured time units as compared Type II. Refer to Figures 26 and 28 for Type I and Type II's polarity vector plots. The addition of a pressure gradients also produce very different results within each simulation; for Type I, periodic state is lost after pressure reaches a certain magnitude. Figures 70 and 71 display fluid velocity in the channel taken at a single point in space over time.

The addition of pressure gradients within the range of $0 < p_x \leq 4$ maintain a periodic state. Increasing magnitudes of p_x have a dampening effect on the wave height. At a critical value between $4 < p_{x_c} \leq 5$, periodic state is lost. Similarly, periodic state is preserved when a negative pressure gradient is applied until a critical value in the range of $-5 \leq p_{x_c} < -4$, where simulations transition to steady state. The steady state simulations of $p_x = \pm 10$ show the steady state polarity vector over time in Figure 72. A familiar geometry is observed, driven solely by the pressure gradient dominating other parameters.

5.2.4 PERIODIC STATE, TYPE II

The application of a pressure gradient to Type II periodic state preserves the periodic solution, as verified in Figures 73 and 74. Referencing the original simulation data for Type II periodic state in Figures 28 and 29(a), we see that through one cycle of data, a reverse

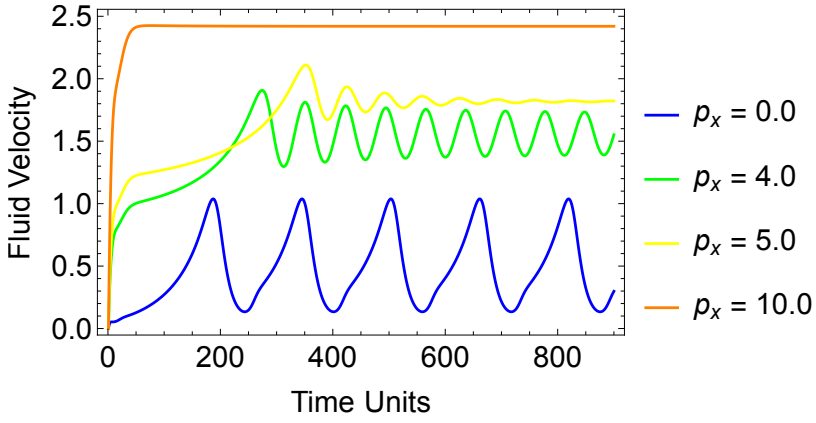

Figure 70: Periodic State, Type I: Dissipation of periodic state with applied positive pressure gradient.

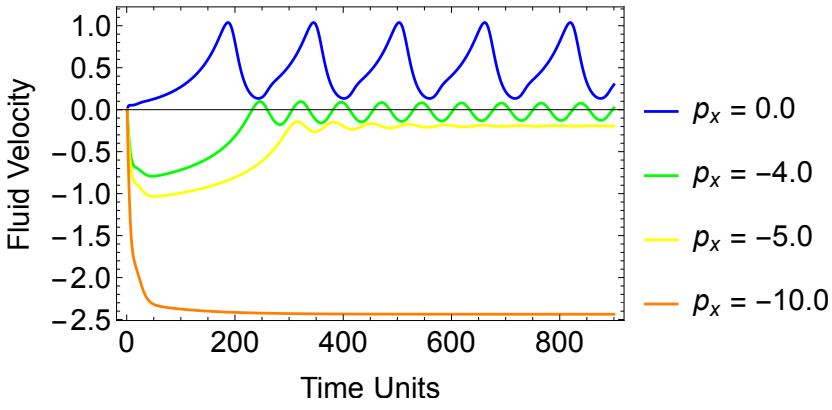

Figure 71: Periodic State, Type I: Dissipation of periodic state with applied negative pressure gradient.

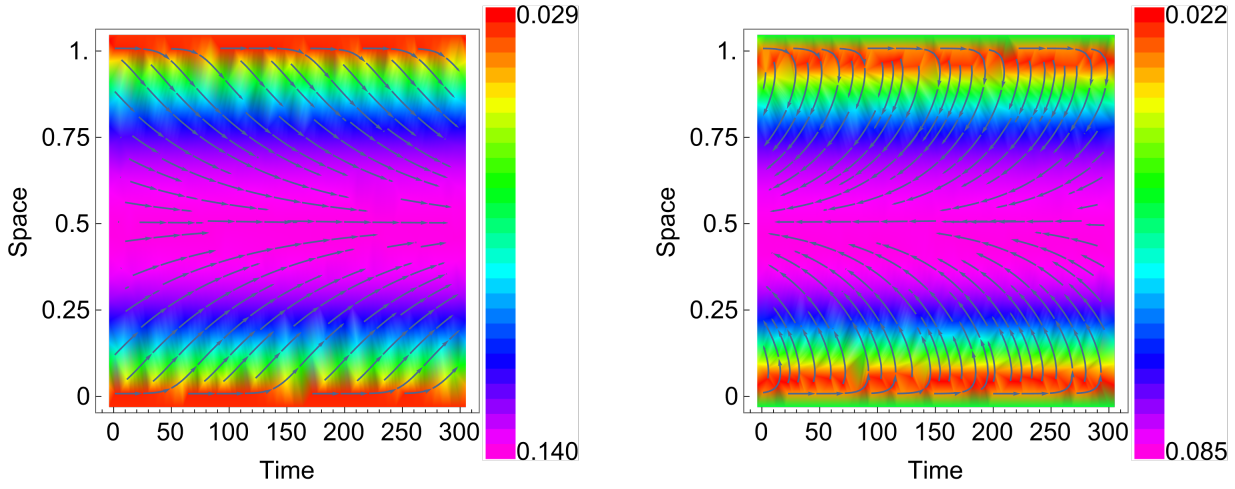

(a) $p_x = 10.0$ (b) $p_x = -10.0$

Figure 72: Periodic State I: Converged Solutions of $p_x = \pm 10.0$.

in both polarity vector orientation and fluid velocity occur simultaneously in different parts of the channel. With that knowledge, when viewing Figures 73 and 74, the sign of velocity indicates only what is happening at that grid point (this set of data is taken near the upper boundary). What can be inferred is that the application of pressure, both positive and negative, decreases the range of velocity fluctuations. A detailed look at the effects of the pressure gradient on wave period length can be seen in Figures 75 and 76. We see that the effect of both pressure gradients linearly decrease the wavelengths (measured in dimensionless time units). Wavelength is at maximum of 29 time units when $p_x = 0$ and linearly decreases to 25 time units when $p_x = \pm 10$.

5.2.5 SUMMARY

Poiseuille simulations on the steady state regions respond similarly to the steady state simulations with negative activation parameter: both forward flows of Outflow and Inflow keep similar geometries with a positive pressure gradient, and both simulations see an increase in fluid velocities. Negative pressure gradients, upon reaching a certain magnitude,

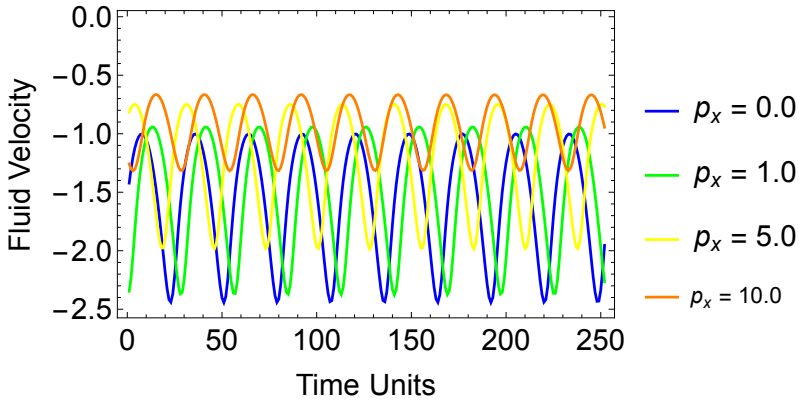

Figure 73: Periodic State II: Preservation of periodic state with applied positive pressure gradient.

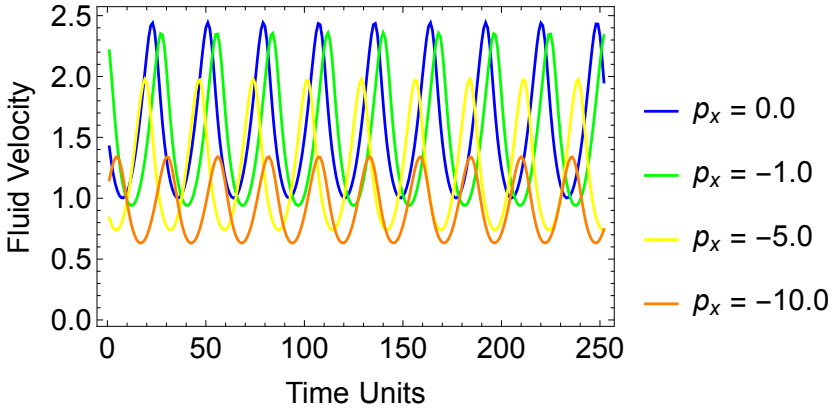

Figure 74: Periodic State II: Preservation of periodic state with applied positive pressure gradient.

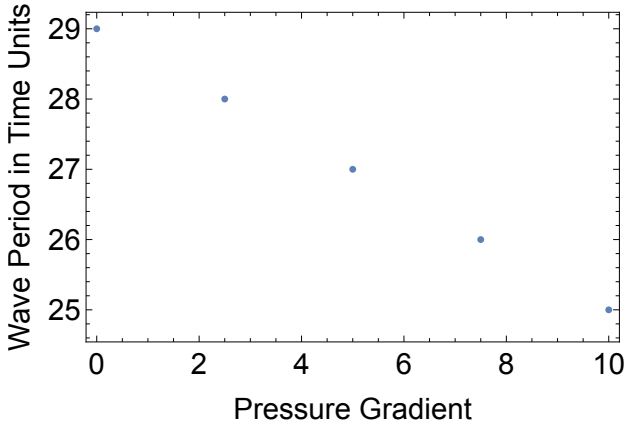

Figure 75: Periodic State II: Effects of positive pressure gradient on wave period length.

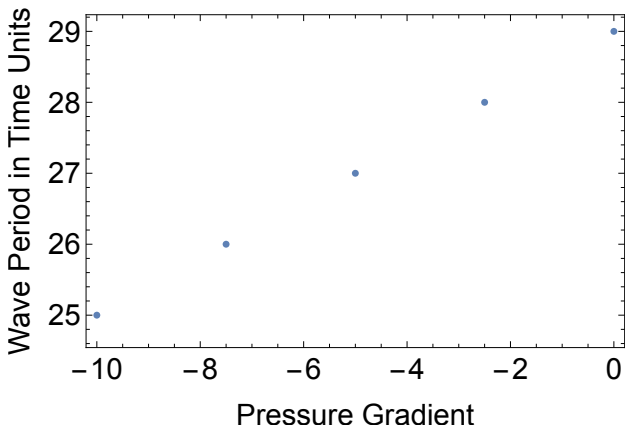

Figure 76: Periodic State II: Effects of negative pressure gradient on wave period length.

produce an inversion of polarity vector geometry in the center of the channel. Periodic State I and II respond in different ways to the application of a pressure gradient. Within Periodic State I, the addition of a pressure gradient, both positive and negative, causes a loss of periodic solution and the simulation becomes steady state. For Periodic State II, the addition of a pressure gradient preserves periodicity while affecting the periodic frequency. As in non-Poiseuille simulations, we see that polarity vector orientation does not correlate to the sign of velocity.

5.3 DIRICHLET BOUNDARY CONDITIONS WITH NORMAL ANCHORING AND PUSHER-LIKE BEHAVIOR

5.3.1 STEADY STATE BENDED FLOW

Bended flow without a pressure gradient is shown in Figure 31. The polarity diagram shows polarity vectors perpendicular to channel walls while oriented leftward in the channel. With the addition of a positive pressure gradient (Figure 77), the polarity vector orientation is reversed while fluid velocity remains positive. With increasing pressure magnitudes, asymmetries are seen in the polarity angles of Figure 77.

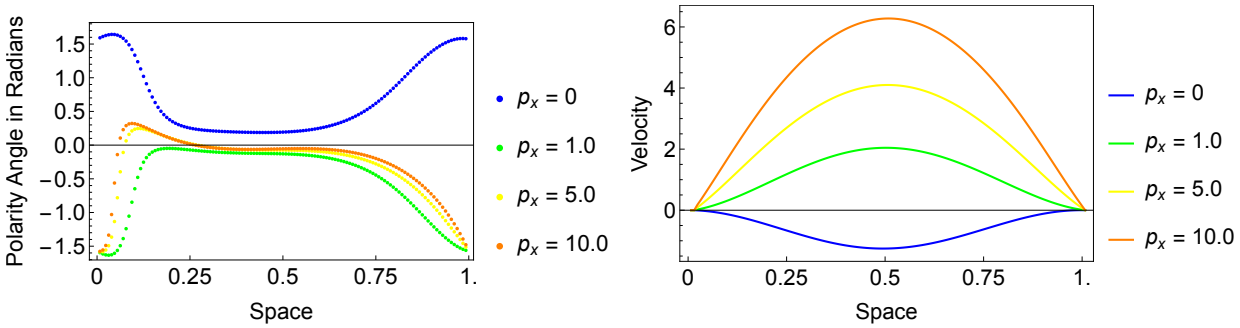

(a) Polarity angles over space.

(b) Fluid velocities over space.

Figure 77: Bended Flow: Positive Pressure Gradient.

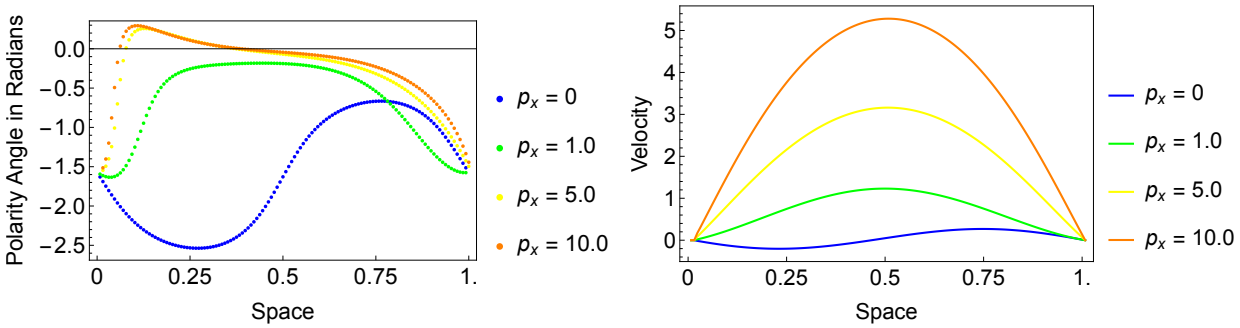

(a) Polarity angles over space.

(b) Fluid velocities over space.

Figure 78: Wiggle Flow: Positive Pressure Gradient.

5.3.2 STEADY STATE WIGGLE FLOW

The interesting geometry observed in this simulation, referred to as Wiggle flow, shows perpendicularly-anchored polarity vectors oriented downward undergo a slight shift rightward, then leftward, as they approach the bottom of the channel, as seen in Figure 33. This effect is destroyed by any addition of a pressure gradient. The effects of pressure on Wiggle flow seen in Figure 78(a) mimic that of the previous simulation with normal anchoring, Bended flow. A positive pressure gradient produces an antisymmetric effect near the lower boundary. The velocity profile in Figure 78(b) shows a parabolic shape with an increasing pressure gradient that increases velocity magnitude. Maximum velocities, reached in the center of the channel, are of similar magnitude to those observed in Bended flow.

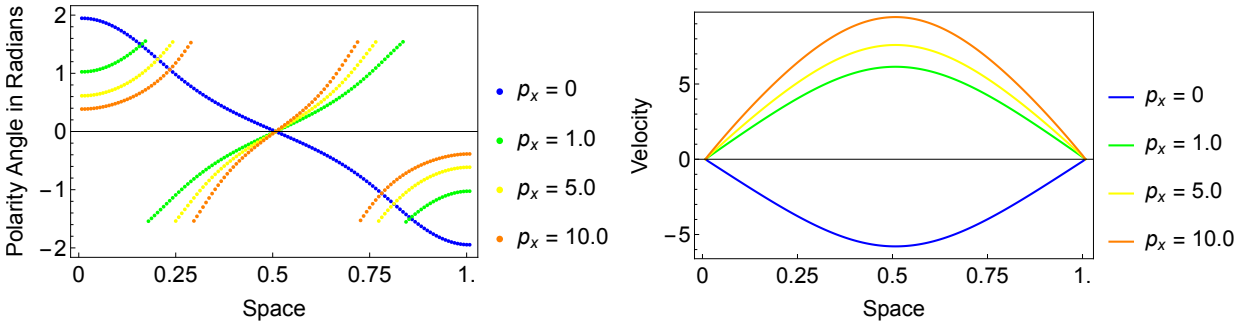

(a) Polarity angles over space.

(b) Fluid velocities over space.

Figure 79: Reverse Flows ($\zeta_a < 0$): Positive Pressure Gradient.

5.4 NEUMANN BOUNDARY CONDITIONS WITH PUSHER-LIKE BEHAVIOR

5.4.1 STEADY STATE REVERSE FLOWS

In Chapter 3, steady state reverse flows with Neumann boundary conditions are viewed as a collection of simulations with varying activation parameters ($-30 \leq \zeta_a \leq -5$). With the addition of pressure, we represent this section as one simulation. The nematic strength of this simulation is $N = 4$, and we use an intermediate activation parameter of $\zeta_a = -15$. We represent this as one simulation as similar effects are seen with the addition of pressure.

Any amount of positive pressure applied to the simulation causes an immediate reversal of fluid flow and polarity vector orientation. As seen in Figure 79, the polarity angles of $p_x = 0$ and $p_x = 1$ are nearly identical reflections. As seen previous simulations, the addition of a negative pressure gradient to a reverse flow increases the velocity of the fluid in the reverse direction, as well as increasing the angle of polarity vector, referencing Figure 80.

5.4.2 SUMMARY

The steady state reverse flow produced by Neumann boundary conditions with a positive activation parameter respond in a predictable way to a pressure gradient. With a positive pressure gradient, the leftward-pointing polarity vector with negative velocity immediately

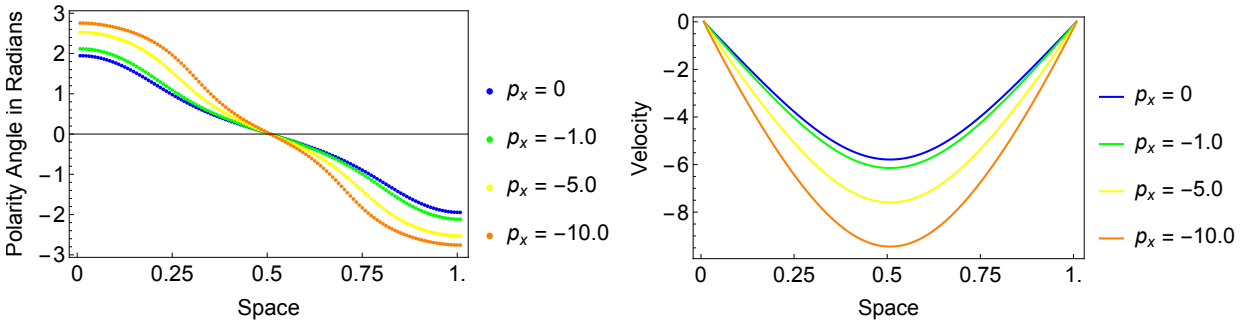

(a) Polarity angles over space.

(b) Fluid velocities over space.

Figure 80: Reverse Flows ($\zeta_a < 0$): Negative Pressure Gradient.

sees a change in orientation to the right, or the direction of the applied pressure. With the addition of a negative pressure gradient, geometry is preserved and velocity magnitude increases.

5.5 NEUMANN BOUNDARY CONDITIONS WITH PULLER-LIKE BEHAVIOR

5.5.1 STEADY STATE REVERSE FLOWS

In Chapter 3, steady state reverse flows with Neumann boundary conditions are viewed as a collection of simulations with varying activation parameters. We represent this section with two simulations, as different phenomena occur when pressure is applied. The first simulation we entitle Reverse Flow I, with parameters of $N = 6$ and $\zeta_a = 10$. The second is Reverse Flow II, with parameters of $N = 7$ and $\zeta_a = 35$.

Reverse Flow I

The addition of a positive pressure gradient to the Reverse Flow I simulation acts as a driving force to the center of the simulation: as the magnitude of pressure is increased, we observe the boundary angles increase until the channel flow is oriented rightward. Figure 81 is a collection of polarity vector diagrams for $p_x = 5$, $p_x = 7$, and $p_x = 10$, respectively. Using

these plots, we can see the progression of geometric changes that the traditional polarity diagrams over space lack. Figure 82 shows the progression of increasing boundary angles as the magnitude of pressure gradient is increased. The boundary angles are measured from the top of the channel ($y = 1.0$). Figure 81(a) shows reverse flow maintained at $p_x = 5$, until the positive pressure gradient acts as a driving force along the centerline of the channel that "bends" the boundary angles forward, until the threshold of $p_x = 7$ (Figure 81(b)). We see the shift to forward flow in Figure 81(c). For completeness, the polarity over space diagram is included in Figure 83(a). We see the transition at $p_x = 7$ from reverse flow to forward flow. Despite the changes in flow orientation and geometry, fluid velocity remains positive and increases as the pressure increases. We see the velocity profile again take a parabolic form, reaching its maximum in the center of the channel.

Negative pressure gradients produce similar geometries of the polarity vector, albeit reversed, as did positive gradients. With the application of any amount of negative pressure gradient, we see the polarity vector geometry immediately switch to a forward orientation, something not witnessed before. Even very small pressure gradients of $p_x = -0.01$ cause a flow reversal of both polarity vector orientation as well as fluid velocity direction. The induced forward flow geometry is maintained while the pressure gradient is within the bounds of $-7 < p_x < -0.01$, as seen in Figure 84(a). At the magnitude of $p_x = -7.0$ we see the polarity vectors along the centerline of the channel in the vertical position in Figure 84(b). With a further increase of pressure, we see the centerline vector now orient left, while the vectors nearer the channel boundaries maintaining their leftward orientation in Figure 84(c). Figure 85 shows the changes of the boundary angles. We notice a discontinuity in the graph between the boundary angle measured when $p_x = 0$ and $p_x = -0.5$. This is due to the immediate flow reversal observed when any amount of negative pressure gradient is applied to the simulation. This immediate flow reversal also causes the fluid velocity to shift from positive (observed at $p_x = 0$) to negative values, and increase in magnitude as pressure is increased, as show in Figure 86(b).

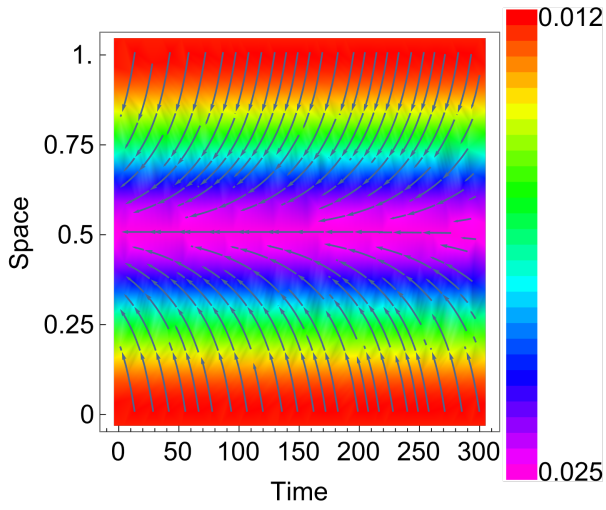

(a) $p_x = 5$.

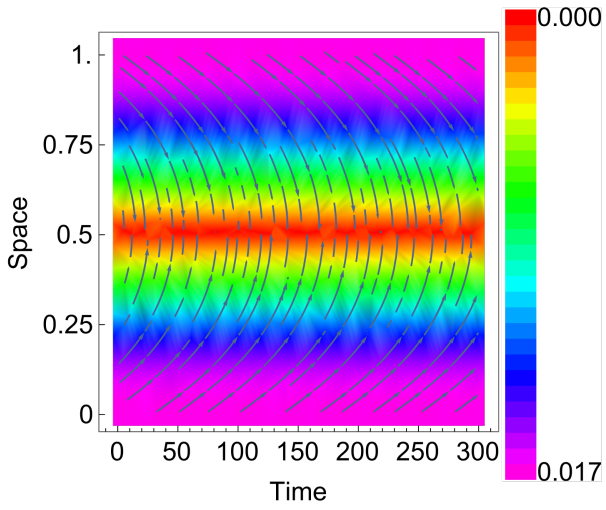

(b) $p_x = 7$.

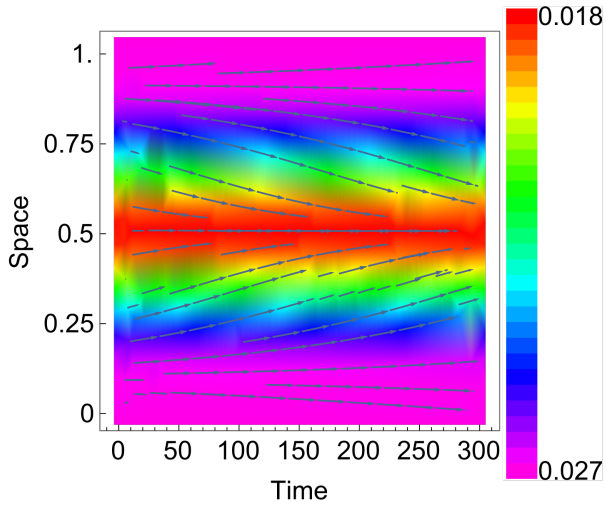

(c) $p_x = 10$.

Figure 81: Reverse Flow I ($\zeta_a > 0$): Positive Pressure Gradient Polarity Vector Diagrams.

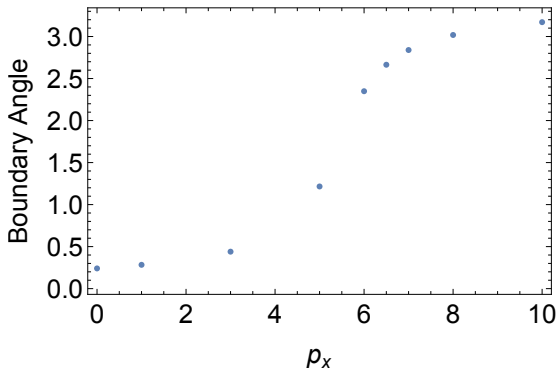

Figure 82: Reverse Flow I ($\zeta_a > 0$): Boundary Angels vs. Positive Pressure Gradient.

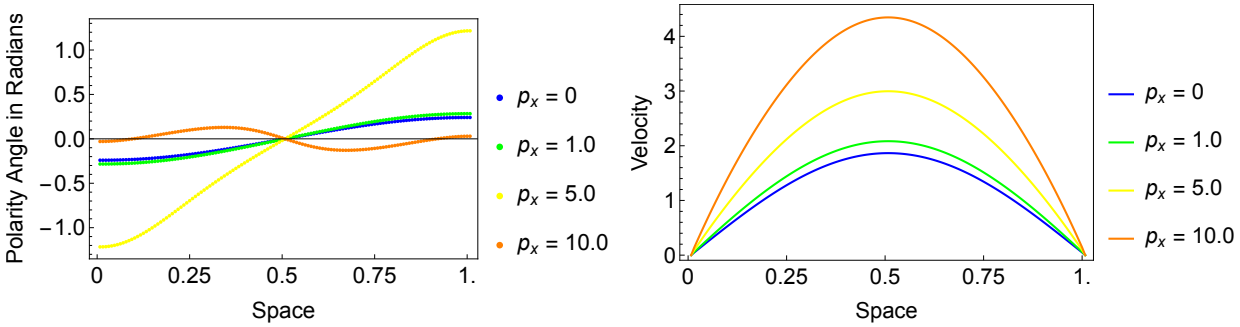

(a) Polarity angles over space.

(b) Fluid velocities over space.

Figure 83: Reverse Flow I ($\zeta_a > 0$): Positive Pressure Gradient.

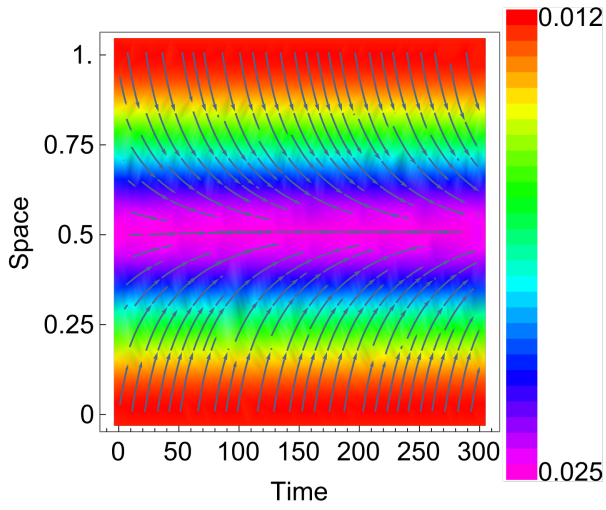

(a) $p_x = -5$.

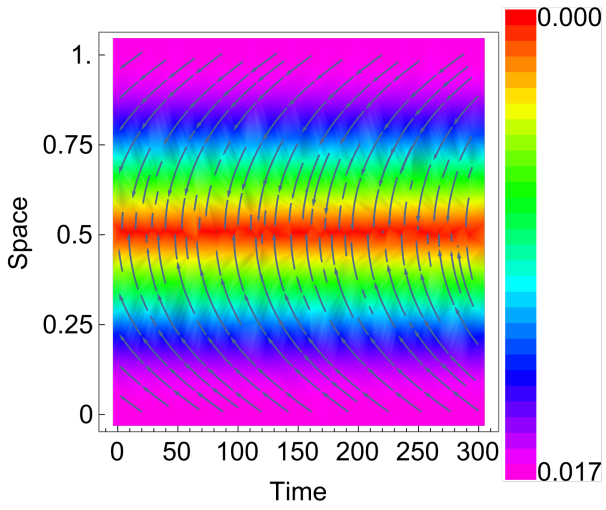

(b) $p_x = -7$.

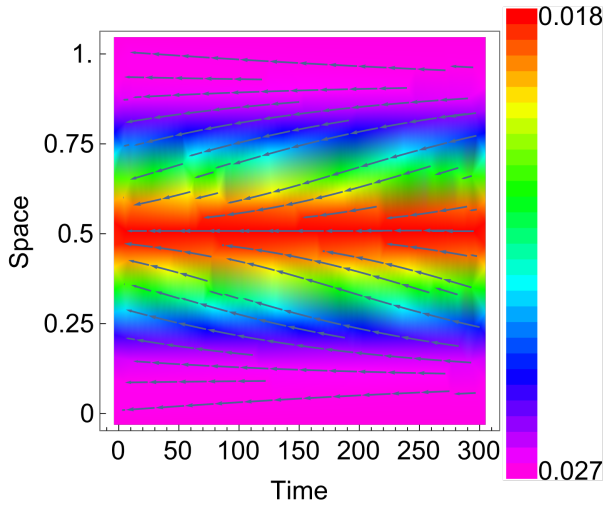

(c) $p_x = -10$.

Figure 84: Reverse Flow I ($\zeta_a > 0$): Negative Pressure Gradient Polarity Vector Diagrams.

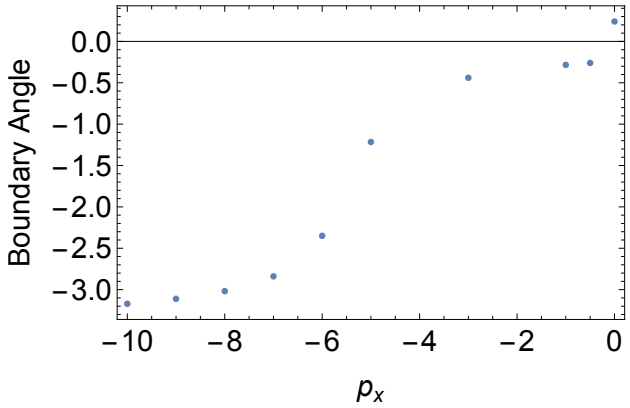

Figure 85: Reverse Flow I ($\zeta_a > 0$): Boundary Angels vs. Negative Pressure Gradient.

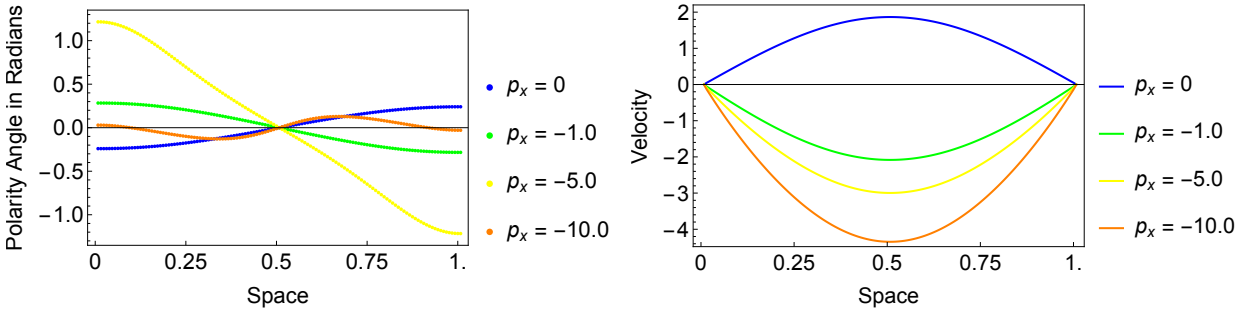

(a) Polarity angles over space.

(b) Fluid velocities over space.

Figure 86: Reverse Flow I ($\zeta_a > 0$): Negative Pressure Gradient.

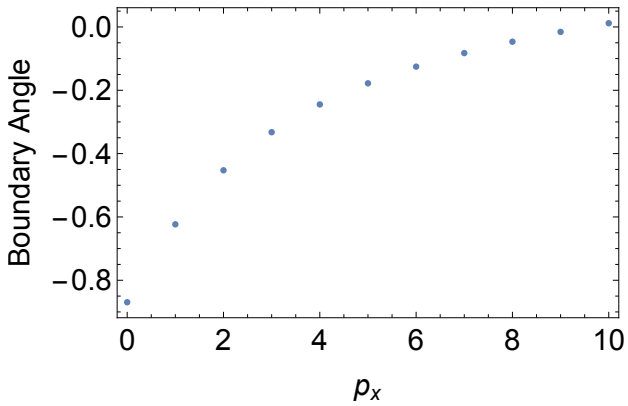

Figure 87: Reverse Flow II ($\zeta_a > 0$): Boundary Angels vs. Positive Pressure Gradient.

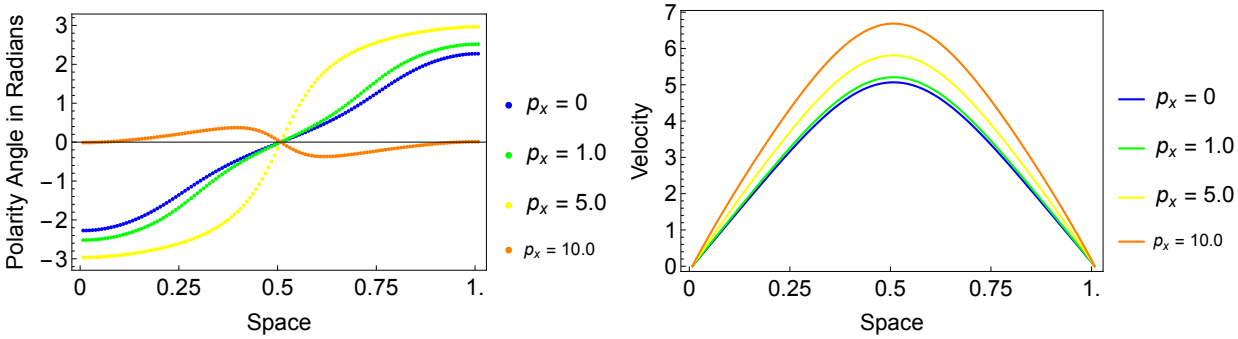

(a) Polarity angles over space.

(b) Fluid velocities over space.

Figure 88: Reverse Flow II ($\zeta_a > 0$): Positive Pressure Gradient.

Reverse Flow II

Reverse Flow II is the second of two reverse flows observed when $N = 6$; however, this simulation includes a much higher activation parameter of $\zeta_a = 35$. When a positive pressure gradient is applied, we see very similar effects as Reverse Flow I: reverse flow is maintained until a critical value of p_x, at which point we then observe the geometry change to forward flow. For Reverse Flow II, this happens around $p_x = 6$. The boundary angle versus p_x are seen in Figure 87. Fluid velocity profile also remains positive and increases in magnitude as positive pressure is increased, as seen in Figure 88.

Applying a negative pressure gradient to Reverse Flow II produces a periodic state

solution when $-1.0 \leq p_x < -0.5$, as seen in Figure 89(a). When $p_x < -1.0$, we see a transition back to steady state, and the polarity angle geometry in Figure 89(b)-(d) and Figure 90 begin to mimic what was seen in Reverse Flow I's negative p_x simulations.

5.5.2 PERIODIC STATE

Periodic state solutions occur in a large number of simulations for Neumann boundary conditions, and when the activation parameter becomes large enough, all couplings with $N > 5$ result in periodic state. When $p_x = 0$, we observe the periodic state of $N = 8$ and $\zeta_a = 20$ in Figure 47. With the addition of a pressure gradient within the bounds of $-1.0 \leq p_x \leq 1.5$, we see a periodic solution. Figure 94 shows how the time units of one wave period are affected by low values of p_x. We see a linear increase in wave period length when negative pressure gradient is applied, from 21 time units when $p_x = 0$ to 26 time units when $p_x = 1.25$. Pressure gradients larger than 1.25 produce steady state solutions. When a positive pressure gradient is added to the simulation, we see a slight decrease in wave period length, with the smallest period observed of 19 time units when $p_x = 1.0$ and 1.5.

Periodic state is lost when $p_x > 1.5$. At $p_x = 0$, we see a reverse flow geometry despite intermittent "pulses" of periodic state fluctuations in Figure 47(a). For p_x values above 1.5, we maintain the reverse flow geometry. We see an increase in the angular change of the polarity angle in the positive/rightward direction in the center of the channel driven by the pressure gradient. This effect can be seen in the polarity vector diagrams found in Figure 92. Reverse flow is preserved with a positive gradient, an effect of Poiseuille flow not seen before. Velocity measures positive when $p_x = 0$ and increases as the gradient is increased.

The addition of a negative pressure gradient similarly produces a centerline-driving effect that changes the flow from reverse to forward between $-2.25 < p_{xc} < -2.0$. At this critical value, we also see a shift in velocity flow direction from forward to negative, as seen in Figure 93. Comparing the polarity angle over space graphs for $p_x = \pm 5$ and $p_x = \pm 10$, the geometries of the pressure gradients of equal magnitudes are mirror images of the other.

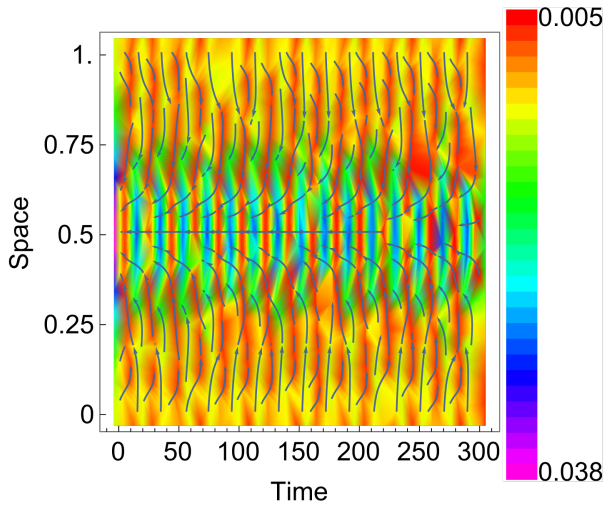

(a) $p_x = -1.0$.

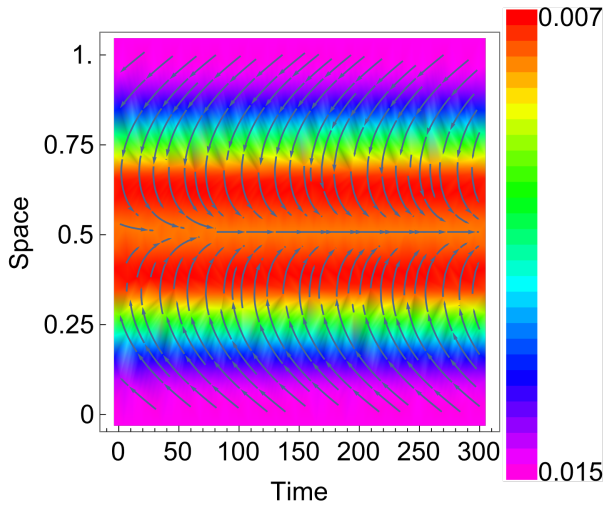

(b) $p_x = -3.0$.

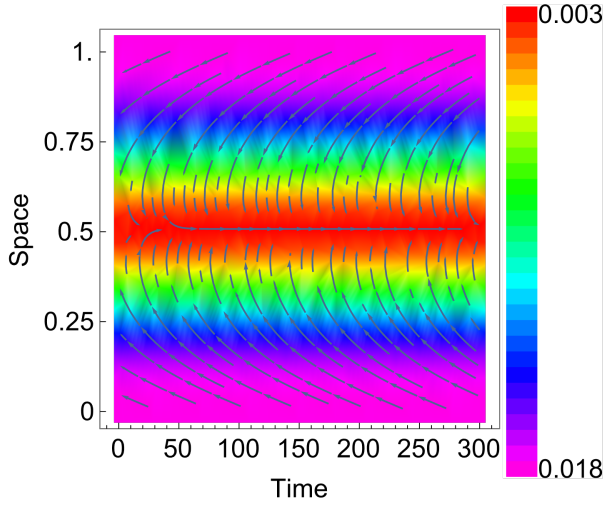

(c) $p_x = -5.0$.

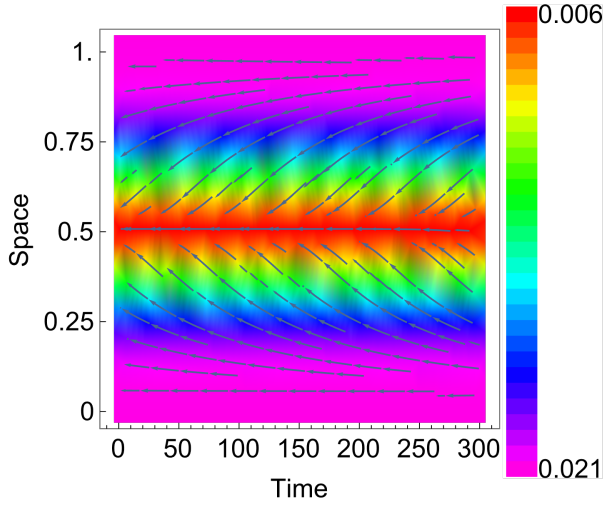

(d) $p_x = -10.0$.

Figure 89: Reverse Flow II ($\zeta_a > 0$): Negative Pressure Gradient Polarity Vector Diagrams.

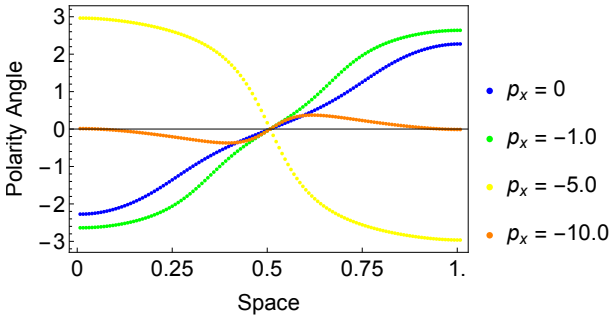

(a) Polarity angles over space.

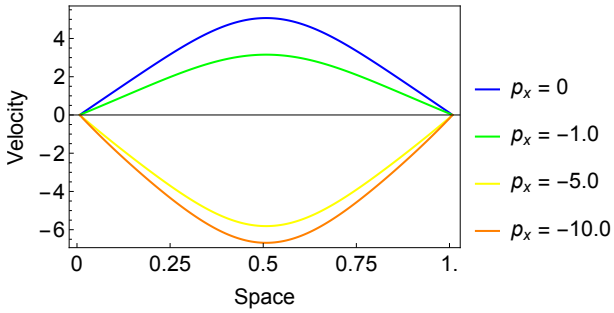

(b) Fluid velocities over space.

Figure 90: Reverse Flow II ($\zeta_a > 0$): Negative Pressure Gradient.

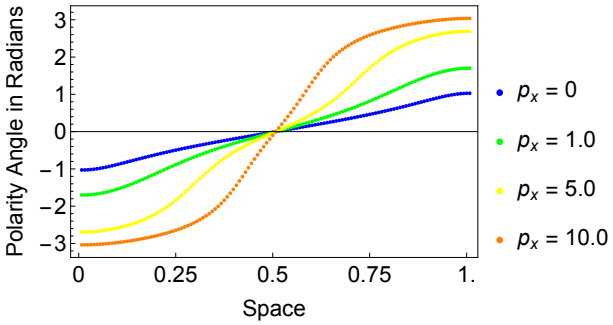

(a) Polarity angles over space.

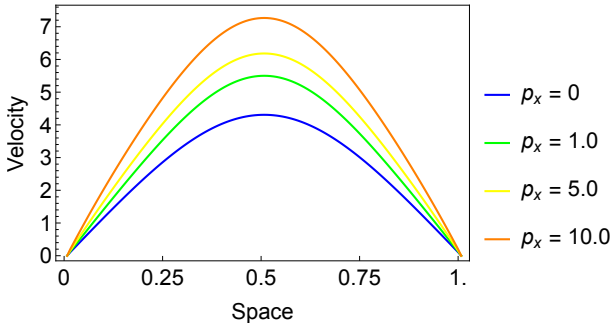

(b) Fluid velocities over space.

Figure 91: Periodic State: Positive Pressure Gradient.

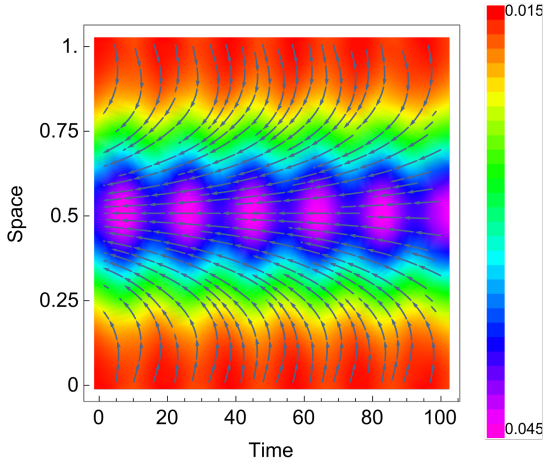

(a) Polarity diagram for $p_x = 1.0$.

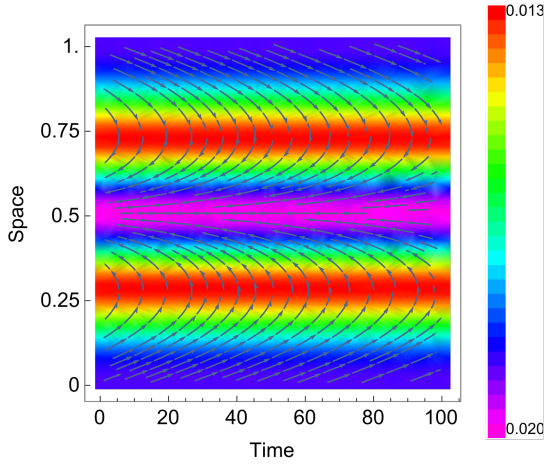

(b) Polarity diagram for $p_x = 5.0$.

Figure 92: Periodic State: Positive Pressure Gradient Effects on Channel Center.

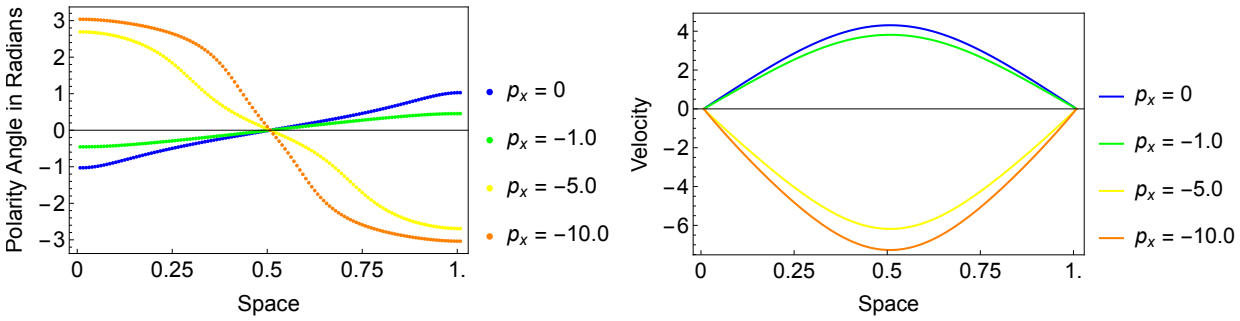

(a) Polarity diagram for $p_x = 1.0$.

(b) Polarity diagram for $_x = 5.0$.

Figure 93: Periodic State: Negative Pressure Gradient.

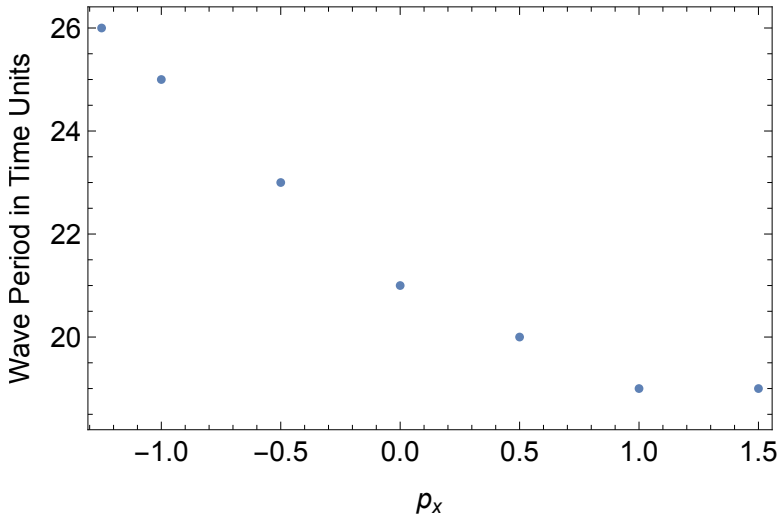

Figure 94: Periodic State: Effects of Pressure Gradient.

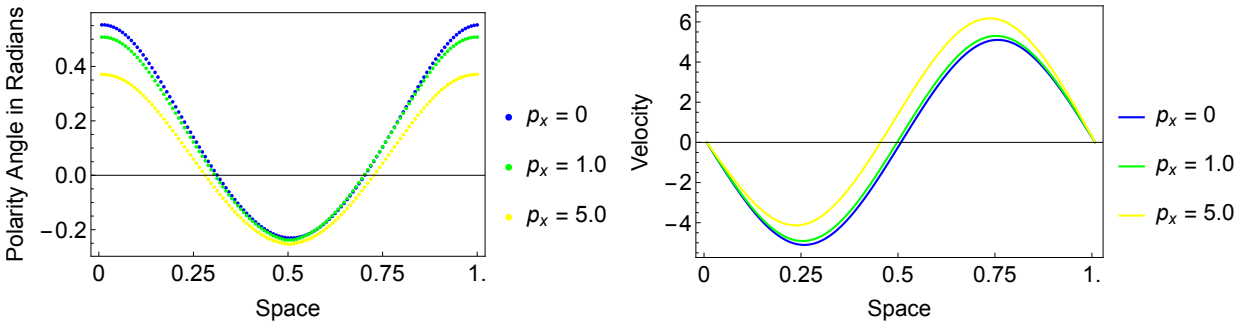

(a) Polarity angles over space.

(b) Fluid velocities over space.

Figure 95: Banded Flow: Positive Pressure Gradient.

5.5.3 STEADY STATE BANDED FLOW

The steady state Banded flow geometry without the addition of a pressure gradient is shown in Figure 49. This simulation couples a high nematic strength with an intermediate activation parameter. In the phase diagram in Figure 42, holding $N = 12$ and increasing the activation parameter causes a periodic state solution. The addition of a pressure gradient to Banded flow produces a similar effect: at some critical value of p_x, steady state becomes periodic state. This happens for both positive and negative values of p_x when $5 < |p_{x_c}| \leq 6$.

For values of $p_x \leq 5$, we see the Poiseuille flow simulations maintain steady state. We view their polarity angles and velocities over space in Figure 95. Velocity maintains its skew-symmetric shape, while increasing the pressure value to $p_x = 5$ produces a slight increase in fluid velocity. When p_x reaches a critical value in between $-5 < p_{x_c} < -4$, we see a flow reversal to a similar Banded flow geometry.

When $5 < |p_x|$, all simulations have periodic solutions. This pressure-induced periodic state is shown in Figure 97. A flow reversal is observed when a positive pressure gradient is applied, as seen in Figure 97(a). Similar geometries exist between both graphs, as well as a similar shape to non-Poiseuille Neumann boundary condition periodic state shown in Figure 47. As pressure is increased for periodic state-inducing values of $|p_x|$, we see a decrease in the size of the wave period, as shown in Figure 98. Increasing the magnitude of pressure gradient, regardless of sign, increases the frequency of the periodic state.

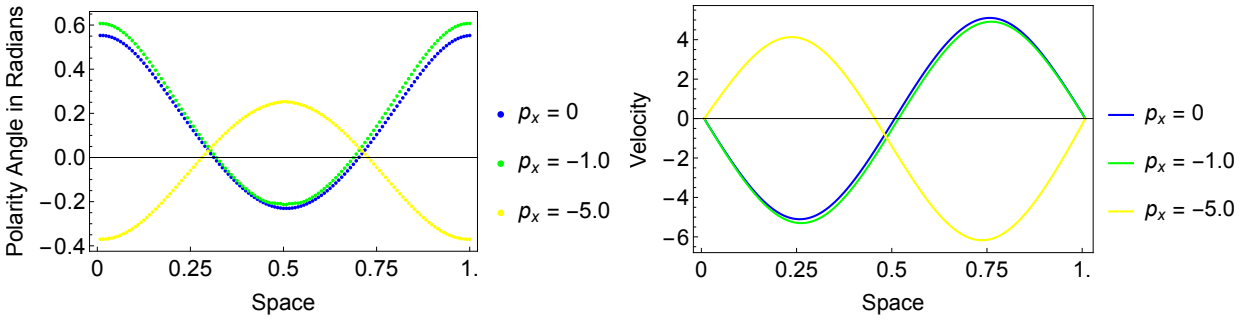

(a) Polarity angles over space.

(b) Fluid velocities over space.

Figure 96: Banded Flow: Negative Pressure Gradient.

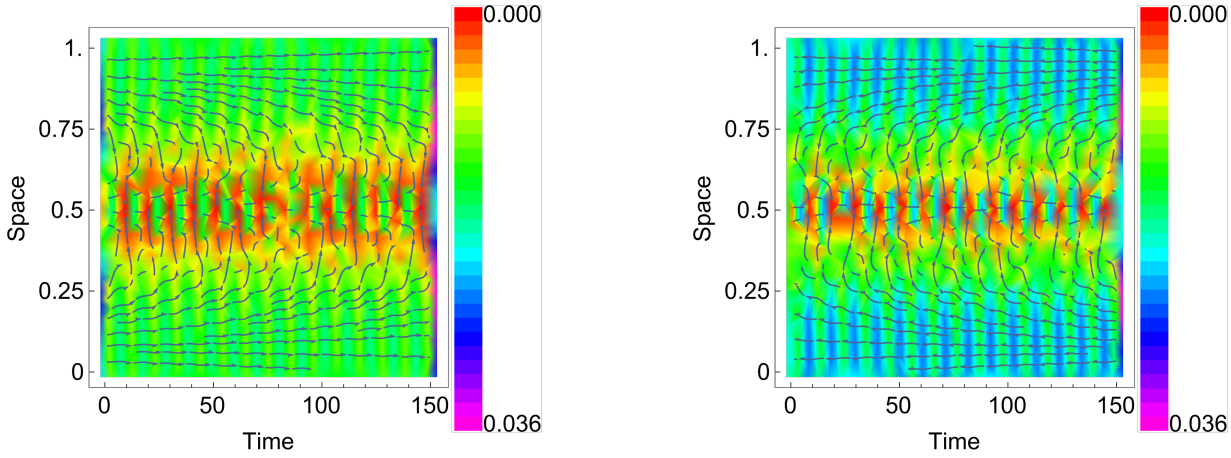

(a) Polarity diagram for $p_x = 10$.

(b) Polarity diagram for $p_x = -10$.

Figure 97: Banded Flow: Pressure-Induced Periodic State Polarity Diagrams.

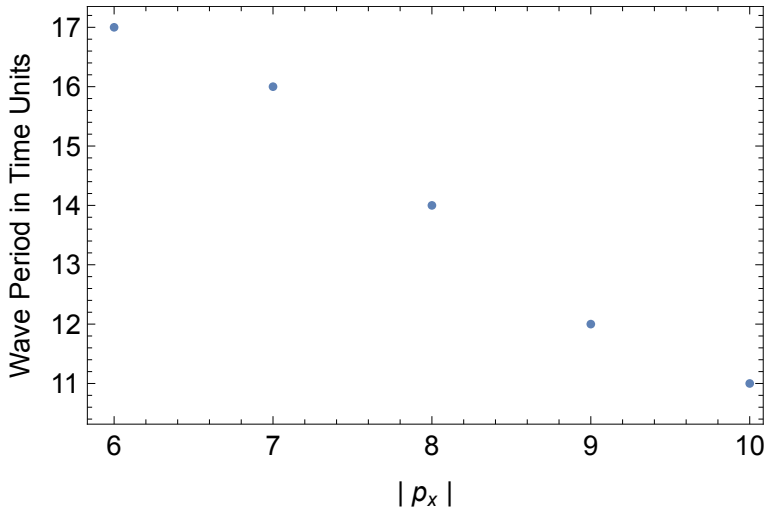

Figure 98: Banded Flow: Pressure-Induced Periodic State Wave Period Comparisons.

5.5.4 SUMMARY

Positive pressure gradients on Reverse Flow I and Reverse Flow II both transition to forward flow after a critical value of p_x is reached. Negative pressure gradients on Reverse Flow I initially transition to a forward flow orientation, then a center-driving effect reorients the geometry back to reverse flow. A small negative pressure gradient on Reverse Flow II causes a periodic state ($-1.0 \leq p_x < -0.5$), then the geometry shifts to a forward flow. Steady state Reverse Flow I transitions to forward flow around a critical value of p_x, while Reverse Flow II sees a pressure-induced periodic state when a small amount of negative pressure gradient is applied. Higher values of p_x transition the simulation back to steady state.

In the Poiseuille simulations for periodic state, we see the periodic state solution preserved for pressure gradient values of $-1.25 \leq p_x \leq 1.5$. Within this range, we see the wave frequency increase with increasing values of p_x. Higher pressure gradient values ($1.5 < p_x$) produce steady state forward flow. Negative values of $p_x < -1.25$ produce steady state reverse flow. Pressure-induced polarity vector orientation correlates to the sign of velocity.

For Poiseuille simulations on Banded flow, when the pressure gradient is above the threshold of $5 < |p_x|$, we see a pressure-induced periodic state. Within this induced periodic state, we observe an increase in frequency with increasing values of $|p_x|$. General flow orientation follows pressure-induced direction, and velocity magnitude increases with increasing magnitude of p_x.

CHAPTER 6

CONCLUSIONS

We explore the Kinetic Model for active nematic liquid crystal polymers within the channel flow simulation space. Of the numerous parameters used in the model, we select nematic concentration and activation parameter and investigate the competing strengths between the two. By varying the values of these parameters, we observe spontaneous flows that result in steady state and periodic state solutions. We conduct numerous simulations and create multiple phase diagrams for different boundary conditions employed on the model.

Within simulations of parallel anchoring coupled with a negative activation parameter, all non-isotropic simulations produce spontaneous flows. We see correlations between polarity vector orientation and the sign of velocity. Within different regions, we see different wave numbers produce polarity vector geometries that are near perfect reflections of the other. Parallel anchoring simulations with positive activation parameters produce spontaneous flows of both steady state and periodic state. Two periodic states are observed, with numerous differences between them to include polarity vector geometry and period of wave length. In contrast to previous simulations, polarity vector orientation does not correlate to the sign of velocity.

Normal anchoring simulations produce spontaneous flows only for pusher-like behavior of the polymers. For the observed steady states, both values of nematic strength and activation parameter are low in magnitude. Larger parameter values produce asymmetric results.

When homogenous Neumann boundary conditions are employed on the Kinetic Model, we see spontaneous flows for both positive and negative activation parameters. Steady states with high order parameters exist as nematic states. Both positive and negative activation parameters produce a large array of reverse flow simulations. We observe the effects on the rheological properties produced by increasing the activation parameter. When the activation parameter is negative, we observe rightward-facing polarity vectors indicate positive velocities and leftward-facing polarity vectors indicate negative fluid velocities. Simulations with

positive activation parameters produce both steady state and periodic states. Rightward-facing polarity vectors indicate a negative velocity, while leftward-facing polarity vectors indicate a positive fluid velocity.

Within the Poiseuille flow simulations, we see mainly four types of responses to an applied pressure gradient: 1) steady state simulations maintain steady state, 2) steady state simulations become periodic, 3) periodic simulations maintain a periodic solution, and 4) periodic simulations transition to steady state. We observe predictable increases in velocity magnitude when the pressure gradient is increased. In steady state solutions, we see similar geometric patterns in the effects of a positive pressure gradient and a negative pressure gradient, where the geometric patterns are reflections of each other within the same pressure gradient magnitude.

For both parallel anchoring and normal anchoring simulations, if the pressure direction is in the initial flow direction, the direction and geometry is unchanged with respect to regions and flow orientation. If the pressure direction is opposite to the flow direction, a near exact geometry in the opposite direction is observed. We see polarity vector orientation correlate to the sign of velocity and observe an increase in velocity magnitude with increasing magnitudes of pressure gradients. We see the two observed periodic states respond in different ways: one loses its periodic solution, while the periodic state with the higher values of nematic strength and activation parameter maintain its periodic solution.

Within the Poiseuille simulations for periodic state, we see the periodic state solutions preserved for pressure gradient values within a small range of pressure gradients. Where periodic state is observed, frequency increases with increasing values of pressure gradients. For large pressure gradients, when applied to steady states solutions with large activation parameters, we see a pressure-induced periodic state. Within this induced periodic state, we observe an increase in frequency with increasing magnitudes of pressure gradients. General flow orientation follows the pressure-induced direction, and velocity magnitude increases with increasing magnitude of pressure gradients.

BIBLIOGRAPHY

[1] Alonso-Matilla, R., Ezhilan, B., and Saintillan, D. Microfluidic rheology of active particle suspensions: Kinetic theory. *Biomicrofluidics 10* (2016).

[2] Baskaran, A., and Marchetti, M. C. Enhanced diffusion and ordering of self-propelled rods. *Physical Review Letters 101* (2008).

[3] Baskaran, A., and Marchetti, M. C. Hydrodynamics of self-propelled hard rods hydrodynamics of self-propelled hard rods. *Physical Review E 77* (2008).

[4] Batista, V. M. O., Blowab, M. L., and da Gamaab, M. M. T. The effect of anchoring on the nematic flow in channels. *Soft Matter*, 11 (2015).

[5] Bird, R. B., Armstrong, R. C., and Hassager, O. *Dynamics of Polymeric Liquids*, 2 ed., vol. 1. John Wiley and Sons, Inc., 1987.

[6] Bird, R. B., Curtiss, C. F., Armstrong, R. C., and Hassager, O. *Dynamics of Polymeric Liquids*, 2 ed., vol. 2. John Wiley and Sons, Inc., 1987.

[7] Budrene, E. O., and Berg, H. C. Complex patterns formed by motile cells of escherichia coli. *Nature 349* (1991).

[8] Charras, G. Biological matters arising. *Nature 544* (April 2017).

[9] Cheong, A., Rey, A. D., and Mather, P. T. Capillary instabilities in thin nematic liquid crystalline fibers. *Physical Review. E, Statistical Physics, Plasmas, Fluids, and Related Interdisciplinary Topics 64* (2001).

[10] Cui, Z., Su, J., and Zeng, X. Apparent viscosity of active nematics in poiseuille flow. *Journal of Physics. Conference Series 640* (2015).

[11] de Gennes, P., and Prost, J. *The Physics of Liquid Crystals*. Oxford University Press, Oxford, 1993.

[12] Doi, M., and Edwards, S. F. *The Theory of Polymer Dynmaics*. Oxford Science Publications, 1988.

[13] Edwards, S. A., and Yeomans, J. M. Spontaneous flow states in active nematics: A unified picture. *Europhysics Letters* (January 2009).

[14] Evans, A. A., Ishikawa, T., Yamaguchi, T., and et al. Orientational order in concentrated suspensions of spherical microswimmers. *Physics of Fluids 23* (2011).

[15] Evans, L. C. *Partial Differential Equations*, 2nd ed. American Mathematical Society, 2010.

[16] Forest, M. G., Wang, Q., and Zhou, R. Scaling behavior of kinetic orientational distributions for dilute nematic polymers in weak shear. *Journal of Non-Newtonian Fluid Mechanics 116* (2003).

[17] Forest, M. G., Wang, Q., and Zhou, R. The weak shear kinetic phase diagram for nematic polymers. *Rheologica acta 43* (2003).

[18] Forest, M. G., Wang, Q., and Zhou, R. Kinetic theory and simluations of active polar liquid crystalline polymers. *Soft Matter 9* (2013), 5207–5222.

[19] Forest, M. G., Wang, Q., and Zhou, R. Kinetic attractor phase diagrams of active nematic suspensions: the dilute regimes. *Soft Matter 11* (2015).

[20] Frank, F. C. I. liquid crystals. on the theory of liquid crystals. *Discussions of the Faraday Society* (1958).

[21] Geng, Y., Kizhakidathazhath, R., and Lagerwall, J. P. F. Robust cholesteric liquid crystal elastomer fibres for mechanochromic textiles. *Nature Materials* (2022).

[22] Ginelli, F., Peruani, F., Bar, M., and Chate, H. Large-scale collective properties of self-propelled rods. *Physical Review Letters 104* (2010).

[23] Giomi, L. Geometry and topology of turbulence in active nematics. *Physical Review X 5* (2015).

[24] Giomi, L., Liverpool, T. B., and Marchetti, M. C. Sheared active fluids: Thickening, thinning, and vanishing viscosity. *Physical Review E 81* (2010).

[25] Giomi, L., Mahadevan, L., Chakraborty, B., and Hagan, M. F. Banding, excitability and chaos in active nematic suspensions. *Nonlinearity* (July 2012).

[26] Giomi, L., Marchetti, M. C., and Liverpool, T. B. Complex spontaneous flows and concentration banding in active polar films. *Physical Review Letters 101* (November 2008).

[27] Giomi, L., Toner, J., and Sarkar, N. Hydrodynamic theory of p-atic liquid crystals. *Physical Review E 106* (2022).

[28] Gupta, S. Application of liquid crystals in space activities. *Frontiers of Polymer Research* (1991).

[29] Iserles, A. *A first course in numerical analysis of differential equations*. Cambridge University Press, 2009.

[30] Koide, N. *The Liquid Crystal Display Story: 50 Years of Liquid Crystal Research and Development That Lead the Way to the Future*. Springer Japan, 2014.

[31] Kudrolli, A., Lumay, G., Volfson, D., and Tsimring, L. S. Swarming and swirling in self-propelled polar granular rods. *Physical Review Letters 100* (2008).

[32] Larson, R. G. *The Stucture and Rheology of Complex Fluids*. Oxford University Press, 1999.

[33] Lauga, E. Propulsion in a viscoelastic fluid. *Physics of Fluids 19* (2007).

[34] Leslie, F. M. Some constitutive equations for liquid crystals. *Archive for Rational Mechanics and Analysis 28* (1968).

[35] Leslie, F. M., Demus, D., Goodby, J., Gray, G. W., Spiess, H.-W., and Vill, V. *Physical Properties of Liquid Crystals*. Wiley-VCH, 1999.

[36] Lin, F., and Chun, L. Static and dynamic theories of liquid crystals. *Journal of Partial Differential Equations 14* (2001).

[37] Liverpool, T. B., and Marchetti, M. C. Hydrodynamics and rheology of active polar filaments. *Physical Review Letters 97* (2006).

[38] Marchetti, M. C., Joanny, J. F., Ramaswamy, S., Liverpool, T. B., Prost, J., Rao, M., and Simha, R. A. Hydrodynamics of soft active matter. *Reviews of Modern Physics 85* (2013).

[39] Mondal, S., Griffiths, I. M., Charlet, F., and Majumdar, A. Flow and nematic director profiles in a microfluidic channel: the interplay of nematic material constants and backflow. *Fluids 3*, 39 (2018).

[40] Mushenheim, P. C., Trivedi, R. R., Weibel, D. B., , and Abbott, N. L. Using liquid crystals to reveal how mechanical anisotropy changes interfacial behaviors of motile bacteria. *Biophysical Journal 107* (2014).

[41] Nedelec, F. J., Surrey, T., Maggs, A. C., and Leibler, S. Self-organization of microtubules and motors. *Nature 389* (1997).

[42] Oseen, C. W. The theory of liquid crystals. *Transactions of the Faraday Society 29* (November 1933).

[43] Pearce, D. J. G., Nambisan, J., Ellis, P. W., Fernandez-Nieves, A., and Giomi, L. Orientational correlations in active and passive nematic defects. *Physical Review Letters 127* (2021).

[44] Phan-Thien, N. *Understanding Viscoelasticity.* Springer, 2002.

[45] Ramaswamy, S. The mechanics and statistics of active matter. *Annual Review of Condensed Matter Physics 1* (2010).

[46] Rey, A. D. Liquid crystal models of biological materials and processes. *Soft Matter 6* (2010).

[47] Rey, A. D., and Denn, M. M. Dynamical phenomena in liquid-crystalline materials. *Annual Review of Fluid Mechanics 34* (2002).

[48] Saintillan, D. Rheology of active fluids. *Annual Review of Fluid Mechanics 50* (2018).

[49] Saintillan, D., and Shelley, M. J. Orientational order and instabilities in suspensions of self-locomoting rods. *Physical Review Letters 99* (2007).

[50] Saintillan, D., and Shelley, M. J. Instabilities, pattern formation, and mixing in active suspensions. *Physics of Fluids 20* (2008).

[51] Saintillan, D., and Shelley, M. J. Active suspensions and their nonlinear models. *Comptes Rendus Physique 14* (2013).

[52] Scharf, T. *Polarized Light in Liquid Crystals and Polymers*. John Wiley and Sons, Inc., 2006.

[53] Simha, R. A., and Ramaswamy, S. Hydrodynamic fluctuations and instabilities in ordered suspensions of self-propelled particles. *Physical Review Letters 89* (2002), 058101.

[54] Sokolov, A., Aranson, I. S., Kessler, J. O., and Goldstein, R. E. Concentration dependence of the collective dynamics of swimming bacteria. *Physical Review Letters 98* (2007).

[55] Sonnet, A., Maffettone, P., and Virga, E. Continuum theory for nematic liquid crystals with tensorial order. *Journal of Non-Newtonian Fluid Mechanics 119* (2004).

[56] Virga, E. G. *Variational Theories for Liquid Crystals*. Champan and Hall, 1994.

[57] Yang, X., and Wang, Q. Role of the active viscosity and self-propelling speed in channel flows of active polar liquid crystals. *Soft Matter 12* (2016).

[58] Zhou, R. Phase transitions and spiral defects of active liquid crystal polymers from a closure model. *Radiation Effects and Defects in Solids 175*, 11-12 (2020).

[59] Zhou, R. Shear stress response of active liquid crystal suspensions. *Radiation Effects and Defects in Solids 175*, 1-2 (2020).

[60] Zhou, R., Forest, M. G., and Wang, Q. Kinetic structure simluations of nematic polymers in plane couette cells. i: The algorithm and benchmarks. *Society for Industrial and Applied Mathematicians 3*, 4 (2005), 853–870.

[61] Zhu, L., Lauga, E., and Brandt, L. Self-propulsion in viscoelastic fluids: Pushers vs. pullers. *Physics of Fluids 24* (2011).

VITA

Lacey Savoie Schenk
Department of Mathematics & Statistics
Old Dominion University

December 2022
lsche007@odu.edu
Norfolk, VA 23529

Education

- Ph.D. in Computational and Applied Mathematics, Old Dominion University, Norfolk, VA. Dissertation: *Channel Flow Simulations of Active Liquid Crystal Polymers*. December 2022 [Anticipated].
- M.S. in Computational and Applied Mathematics, Old Dominion University, Norfolk, VA. May 2019.
- M.S. in Secondary Education for Mathematics, Old Dominion University, Norfolk, VA. May 2017.
- B.S. in Systems Engineering with Merit, United States Naval Academy, Annapolis, MD. May 2008.

Publications

- Schenk, L., and Zhou, R., "*Active Polar Liquid Crystal Channel Flows: Analyzing the Roles of Nematic Strength and Activation Parameter*," College of Sciences Posters. (2022)

Presentations

- Schenk, L. "*Active Polar Liquid Crystal Channel Flows: Analyzing the Roles of Nematic Strength and Activation Parameter*," Society of Industrial and Applied Mathematicians Annual Meeting, Pittsburgh, Pennsylvania. (July 14, 2022)

Awards

- Marsh Award for Best Capstone Robotic Design Project. May 2008.
- Outstanding Military Career Transition Program Student Award. May 2017.
- Student Travel Award from Society of Industrial and Applied Mathematicians Annual Conference. July 2022.
- Old Dominion University Graduate Student Research Travel Award. July 2022.

Typeset using LaTeX.